Eur. Phys. J. C (2025) 85:72
https://doi.org/10.1140/epjc/s10052-024-13606-8

THE EUROPEAN PHYSICAL JOURNAL C

Regular Article - Experimental Physics

Measurement of multidifferential cross sections for dijet production in proton–proton collisions at $\sqrt{s} = 13$ TeV

CMS Collaboration*

CERN, 1211 Geneva 23, Switzerland

Received: 27 December 2023 / Accepted: 12 November 2024
© CERN for the benefit of The CMS Collaboration 2025

Abstract A measurement of the dijet production cross section is reported based on proton–proton collision data collected in 2016 at $\sqrt{s} = 13$ TeV by the CMS experiment at the CERN LHC, corresponding to an integrated luminosity of up to 36.3 fb^{-1}. Jets are reconstructed with the anti-k_{T} algorithm for distance parameters of $R = 0.4$ and 0.8. Cross sections are measured double-differentially (2D) as a function of the largest absolute rapidity $|y|_{\text{max}}$ of the two jets with the highest transverse momenta p_{T} and their invariant mass $m_{1,2}$, and triple-differentially (3D) as a function of the rapidity separation y^*, the total boost y_{b}, and either $m_{1,2}$ or the average p_{T} of the two jets. The cross sections are unfolded to correct for detector effects and are compared with fixed-order calculations derived at next-to-next-to-leading order in perturbative quantum chromodynamics. The impact of the measurements on the parton distribution functions and the strong coupling constant at the mass of the Z boson is investigated, yielding a value of $\alpha_{\text{S}}(m_{\text{Z}}) = 0.1179 \pm 0.0019$.

1 Introduction

The production of jets in high-energy proton–proton (pp) collisions provides an important experimental input for the determination of the proton structure in terms of parton distribution functions (PDFs), and for the study of the strong force described by quantum chromodynamics (QCD). In conjunction with deep-inelastic $\text{e}^{\pm}\text{p}$ scattering (DIS) measurements [1,2], which strongly constrain the quark PDFs, jet data from pp collisions at the LHC provide sensitivity to the gluon content and allow the running of the strong coupling constant α_{S} to be probed over a wide range of momentum scales. Recent progress made in calculating predictions for these processes at next-to-next-to-leading order (NNLO) accuracy [3,4] in perturbative QCD (pQCD) underscores the need for precise experimental data up to the highest accessible energies.

Dijet observables are particularly well-suited for this purpose owing to the abundant production of jets in hadron-induced processes across a large phase space, which makes it possible to perform high-precision multi-differential measurements. Such measurements performed at the LHC include a triple-differential (3D) dijet measurement at a center-of-mass energy $\sqrt{s} = 8$ TeV [5] using jets reconstructed with the anti-k_{T} clustering algorithm [6,7] with a distance parameter $R = 0.7$, and several double-differential (2D) measurements at 7 and 13 TeV [8–12] for anti-k_{T} jets with $R = 0.4$, 0.6, or 0.7.

In this article, measurements of the dijet production cross section in pp collisions at $\sqrt{s} = 13$ TeV from the CMS Collaboration are presented, using anti-k_{T} jets for two values of the distance parameter, $R = 0.4$ and 0.8. Both 2D and 3D measurements are performed as a function of the kinematic properties of the two jets with the highest transverse momenta (p_{T}) in the event.

In the 2D case, the cross section is measured as a function of the largest absolute rapidity $|y|_{\text{max}}$ of the two jets and the invariant mass $m_{1,2}$ of the dijet system, as done for the CMS measurements at $\sqrt{s} = 7$ TeV [9,10]. For the 3D measurements, the same two angular observables are considered as for the previous CMS measurement at $\sqrt{s} = 8$ TeV [5]: the dijet rapidity separation $y^* = |y_1 - y_2|/2$ and the total boost of the dijet system $y_{\text{b}} = |y_1 + y_2|/2$, where y_1 and y_2 indicate the rapidities of the jets. The measurements are performed as a function of y^*, y_{b}, and $m_{1,2}$, and alternatively as a function of y^*, y_{b}, and the average p_{T} of the two jets, $\langle p_{\text{T}} \rangle_{1,2}$.

The 2D and 3D measurements cover a largely overlapping phase space. However, each of the two presents different experimental advantages stemming from the difference in the information content of the respective observables. The 2D measurement features a more inclusive rapidity binning, leading to an increased statistical precision and a larger accessible range in $m_{1,2}$. The use of two angular observables for the 3D measurement provides additional information on the dijet topology, at the expense of a reduced reach in $m_{1,2}$. Moreover, the variables y^* and y_{b} encode the dependence on

* e-mail: cms-publication-committee-chair@cern.ch (corresponding author)

Published online: 24 January 2025

the partonic scattering angle in the laboratory frame and the imbalance in the initial-state parton momenta, respectively. This is advantageous for comparisons to fixed-order pQCD predictions, which are obtained by convolving the partonic scattering cross sections and the PDFs. Specifically, the relation between the dijet invariant mass and the proton momentum fractions $x_\pm$ carried by the incoming partons is given at leading order (LO) by $x_\pm = m_{1,2}\ \exp(\pm y_\mathrm{b})/\sqrt{s}$. Using the average dijet p_T instead renders the y^* dependence explicit and gives $x_\pm = 2\langle p_\mathrm{T}\rangle_{1,2}\cosh(y^*)\exp(\pm y_\mathrm{b})/\sqrt{s}$.

This article is organized as follows. A brief description of the CMS detector is given in Sect. 2. Section 3 presents the samples of recorded and simulated events used for the measurement. In Sect. 4, the reconstruction of the event content is described, and the selection criteria applied to events entering this analysis are given. Sections 5 and 6 detail the measurement of the 2D and 3D dijet cross sections using the reconstructed jets, and the unfolding of the resulting spectra to correct for detector effects, respectively. The different sources of experimental uncertainty in the measurement are outlined in Sect. 7. The measurements are compared to fixed-order predictions obtained at NNLO accuracy in pQCD, which are discussed in Sect. 8. A comparison of the measurements to the predictions obtained for several global PDF sets is presented in Sect. 9. In Sect. 10, the impact of including the present measurements in determinations of PDFs and the strong coupling constant at the scale of the Z boson mass, $\alpha_\mathrm{S}(m_\mathrm{Z})$, is investigated. Finally, a summary of the main findings is given in Sect. 11.

Tabulated results are provided in the HEPData record for this analysis [13].

2 The CMS detector

The central feature of the CMS apparatus is a superconducting solenoid of 6 m internal diameter, providing a magnetic field of 3.8 T. Within the solenoid volume are a silicon pixel and strip tracker, a lead tungstate crystal electromagnetic calorimeter (ECAL), and a brass and scintillator hadron calorimeter (HCAL), each composed of a barrel and two endcap sections. Forward calorimeters extend the pseudorapidity (η) coverage provided by the barrel and endcap detectors. Muons are detected in gas-ionization chambers embedded in the steel flux-return yoke outside the solenoid.

Events of interest are selected using a two-tiered trigger system [14]. The first level, composed of custom hardware processors, uses information from the calorimeters and muon detectors to select events at a rate of around 100 kHz within a fixed latency of about 4μs [15]. The second level, known as the high-level trigger (HLT), consists of a processor farm running a compact version of the full event reconstruction software, optimized for fast processing, and reduces the event rate to around 1 kHz before data storage.

A more detailed description of the CMS detector, together with a definition of the coordinate system used and the relevant kinematic variables, can be found in Ref. [16].

Table 1 Overview of the single-jet (dijet) triggers deployed for the different p_T ($\langle p_\mathrm{T}\rangle$) thresholds at the HLT, and the corresponding integrated luminosities

	Trigger threshold (GeV)				
	40	60	80	140	200
Trigger set	Int. luminosity (pb^{-1})				
Single-jet $R = 0.4$	0.3	0.7	2.8	24.2	103.6
Single-jet $R = 0.8$	0.05	0.3	1.0	10.1	85.8
Dijet $R = 0.4$	0.1	1.7	4.2	27.9	140.2
	Trigger threshold (GeV)				
	260	320	400	450	500
Trigger set	Int. luminosity (fb^{-1})				
Single-jet $R = 0.4$	0.6	1.8	5.2	36.3	36.3
Single-jet $R = 0.8$	0.5	1.5	4.6	33.5	33.5
Dijet $R = 0.4$	0.5	3.0	9.1	–	29.6

3 Data and simulated samples

The measurements presented in this article are based on pp collision data recorded by the CMS detector in 2016 at $\sqrt{s} = 13$ TeV, corresponding to an integrated luminosity of up to 36.3 fb^{-1}. Collision events containing jets are identified during data taking by dedicated trigger algorithms. Owing to the stringent timing constraints, jets at the HLT are clustered from particle candidates reconstructed using a simplified procedure, as compared to the full offline reconstruction.

The integrated luminosity recorded by the available jet-related triggers is given in Table 1. Several sets of triggers are deployed, which require the presence of at least one jet (two jets) with a p_T (average p_T) above certain predefined thresholds. While distinct sets of single-jet triggers are deployed for anti-k_T jets with distance parameters of $R = 0.4$ and 0.8, only the former are used for the dijet triggers. The integrated luminosity delivered by each of these triggers depends on the total time period during which it was deployed. In addition, low-threshold triggers are prescaled by a factor that is continually adjusted during data taking to optimize the data acquisition rate, resulting in lower effective integrated luminosities.

To study the impact of the detector response on the measurement, samples of simulated events produced using Monte Carlo (MC) event generators are used. Events are generated

at LO in pQCD using PYTHIA 8 [17] (version 8.212) with the CUETP8M1 tune [18]. The matrix element calculation is matched to the parton shower and takes multi-parton interactions and hadronization effects into account. An alternative LO sample, generated using the MADGRAPH5_aMC@NLO program [19] (version 2.2.2) and interfaced with PYTHIA for the simulation of parton showering and hadronization, is used to estimate the dependence of results on the simulation model.

To simulate contributions from additional pp collisions (pileup), the particles emerging from the high-energy scattering are overlaid with simulated minimum-bias events and propagated through a full simulation of the CMS detector modeled using the GEANT4 package [20]. The resulting signals are then processed using the same reconstruction techniques used for collision data. Differences between the simulated and measured pileup activity are accounted for using a global reweighting of simulated events based on the mean number of pileup interactions determined in data based on an estimated inelastic pp collision cross section of 69.2 mb. This number is obtained using the pileup counting method described in the inelastic cross section measurement [21]. About 23 pileup interactions occurred for each proton bunch collision during the 2016 data taking [22].

4 Event reconstruction and selection

A global description of collision events is achieved following the particle-flow approach [23], which aims to identify and measure the kinematic properties of each individual particle emerging from the collision using an optimized combination of information from the various elements of the CMS detector.

The trajectories of charged particles, as well as their originating pp interaction vertices are reconstructed from hits in the inner tracking detectors. The primary vertex is taken to be the vertex corresponding to the hardest scattering in the event, evaluated using tracking information alone, as described in Section 9.4.1 of Ref. [24].

Muons are identified as particle tracks in the inner detector layers that are compatible with either a track or several hits in the muon system, and are associated with calorimeter deposits consistent with the muon hypothesis. The muon four-momentum is determined by fitting the muon trajectory using information from both the inner tracker and the muon system.

Photons are identified as ECAL energy clusters not linked to the extrapolation of any charged-particle track to the ECAL. Electrons are identified by linking a primary charged-particle track to potential energy deposits in the ECAL. The resulting energy clusters are required to be spatially compatible with the extrapolated track to the ECAL, or consistent with bremsstrahlung photons emitted in the tracker material. While for photons the energy is obtained directly from the ECAL measurement, the electron energy is determined from a combination of the track momentum at the primary interaction vertex and the associated ECAL clusters.

Charged hadrons are identified as particle tracks not identified as electrons or muons, and neutral hadrons are identified as HCAL energy clusters not linked to any charged-hadron trajectory, or as a combined ECAL and HCAL energy excess with respect to the expected charged hadron energy deposit. The energy of charged hadrons is determined by combining the track momentum and the corresponding ECAL and HCAL energies, corrected for the response function of the calorimeters to hadronic showers. The energy of neutral hadrons is obtained from the corresponding corrected ECAL and HCAL energies.

For each event, jets are clustered from the reconstructed particle candidates using the infrared- and collinear-safe anti-k_T algorithm [6,7] with distance parameters of $R = 0.4$ and 0.8. The jet momentum is determined as the vector sum of all particle momenta in the jet, and is found from simulation to be, on average, within 5–10% of the true momentum over the entire p_T range and detector acceptance used in the analysis. To mitigate the effect of pileup, which can contribute additional tracks and calorimetric energy depositions to the jet momentum, charged particles identified as originating from pileup vertices are discarded and an offset correction [25] is applied to account for the remaining contributions.

Jet energy corrections [26] are derived from simulation studies so that the average energy of reconstructed jets becomes identical to that of particle-level jets. The latter are defined as jets clustered from all stable particles produced in the collision, excluding neutrinos. In situ measurements of the momentum balance in dijet, photon+jet, Z+jet, and multijet events are used to account for any residual differences in the jet energy scale (JES) between data and simulation. The jet energy resolution (JER) typically amounts to 15–20% at 30 GeV, 10% at 100 GeV, and 5% at 1 TeV [26]. It is measured in data using similar jet balancing approaches as for the JES, and residual differences between data and simulation are corrected by smearing the p_T of simulated jets accordingly. Additional selection criteria [27] are applied to each jet to remove jets potentially dominated by spurious contributions from various subdetector components or reconstruction failures. Similarly, anomalous events caused by reconstruction failures, detector malfunctions, or noncollision backgrounds are identified and rejected by dedicated event filters. These are designed to identify more than 85–90% of anomalous events with a misidentification rate of less than 0.1%. Further details can be found in Ref. [28].

Events entering the 2D cross section measurements for both $R = 0.4$ and 0.8 are required to have been accepted by at least one single-jet trigger path operating on jets with the

same distance parameter. For the 3D measurements, the dijet triggers are used on account of their lower overall prescale values.

To guarantee a high reconstruction efficiency at the trigger level, trigger paths with different thresholds are assigned to mutually exclusive phase space regions. These are determined for single-jet (dijet) triggers based on measurements of the trigger efficiency as a function of the leading jet p_T (average p_T of the two leading jets), requiring the trigger efficiency to remain above 99.5% in each region.

During the 2016 data taking, a gradual shift in the timing of the inputs of the ECAL first-level trigger in the region defined by $|\eta| > 2.0$ caused the trigger signal to be incorrectly associated to the previous bunch crossing ("prefiring"), leading to a specific trigger inefficiency. For events containing a jet with a p_T larger than $\approx$100 GeV, the efficiency loss in the region $2.5 < |\eta| < 3.0$ is $\approx$10–20%, depending on p_T, η, and time. Correction factors were computed from data and applied to the acceptance evaluated from simulation.

Further selection criteria are applied to events passing the trigger selection, based on the kinematic properties of two jets with the highest p_T, denoted in the following by the subscripts 1 and 2 for the p_T-leading and p_T-subleading jets, respectively. For the former, a requirement of $p_{T,1} > 100$ GeV and $|y_1| < 3$ is imposed, while the latter is required to satisfy $p_{T,2} > 50$ GeV and $|y_2| < 3$.

5 Cross section measurement

The dijet production cross section is measured both double- and triple-differentially for anti-k_T jets with distance parameters of $R = 0.4$ and 0.8 in terms of the properties of the system formed by the two p_T-leading jets. The 2D spectra are reconstructed as a function of $m_{1,2}$ in five rapidity regions defined in terms of the variable $|y|_{max} = |y_{max}|$, where y_{max} corresponds to the rapidity of the jet closer to the beam line (outermost jet), and is given by

$$y_{max} = \text{sign}(|\max(y_1, y_2)| - |\min(y_1, y_2)|) \times \max(|y_1|, |y_2|). \quad (1)$$

In the 3D case, the cross section is measured as a function of $m_{1,2}$ and $\langle p_T \rangle_{1,2}$ in 15 rapidity regions, defined in terms of the dijet rapidity separation y^* and the total boost y_b of the dijet system, as given by

$$y^* = \frac{1}{2}|y_1 - y_2|, \quad y_b = \frac{1}{2}|y_1 + y_2|. \quad (2)$$

The variables $m_{1,2}$ and $\langle p_T \rangle_{1,2}$ are obtained as

$$m_{1,2} = \sqrt{(E_1 + E_2)^2 - (\vec{p}_1 + \vec{p}_2)^2}, \quad \langle p_T \rangle_{1,2} = \frac{1}{2}\left(p_{T,1} + p_{T,2}\right), \quad (3)$$

where the subscripts 1 and 2 refer to the p_T-leading and p_T-subleading jets, respectively.

The differential dijet spectra are reconstructed from the effective event yield N_{eff} in bins of the chosen observables, normalized to the integrated luminosity $\mathcal{L}_{int}$. The effective event yield is calculated from the raw event yield, taking into account the selection efficiency and subtracting background contributions. In addition, events that enter the measurement are weighted according to the prescale factor of the trigger path assigned to the corresponding phase space region.

The 2D cross section is obtained as a function of y_{max} and $m_{1,2}$ as

$$\frac{d^2\sigma}{dy_{max}dm_{1,2}} = \frac{1}{\mathcal{L}_{int}} \frac{N_{eff}}{(2\,\Delta|y|_{max})\Delta m_{1,2}}. \quad (4)$$

Here, $\Delta|y|_{max}$ and $\Delta m_{1,2}$ denote the width of the bins in the respective quantities. The measurement is performed in five rapidity bins of equal size within $0 < |y|_{max} < 2.5$ and covers an invariant mass range of $249 < m_{1,2} < 10{,}050$ GeV. The measurement boundaries are chosen starting from a preliminary binning determined using simulated samples based on the expected experimental resolution in $m_{1,2}$, and discarding bins at low $m_{1,2}$ that do not meet the minimal trigger efficiency requirement of 99.5%, and bins at high $m_{1,2}$ for which the statistical uncertainty exceeds 50%.

For the 3D measurement, the cross section is obtained as

$$\frac{d^3\sigma}{dy^*dy_b dx} = \frac{1}{\mathcal{L}_{int}} \frac{N_{eff}}{\Delta y^* \Delta y_b \Delta x}. \quad (5)$$

As in Eq. (4), the event yield is normalized to the observable bin widths Δy^*, Δy_b and Δx, where x stands for either $m_{1,2}$ or $\langle p_T \rangle_{1,2}$. Fifteen rapidity regions are investigated, covering the range from 0 to 2.5 in each observable, as illustrated in Fig. 1. Different invariant mass and average transverse momentum regions are measured depending on the rapidity region, covering a range of $306 < m_{1,2} < 6094$ GeV and $147 < \langle p_T \rangle_{1,2} < 2702$ GeV, respectively. These ranges are obtained using an analogous procedure as for the 2D measurements.

6 Unfolding

Because of the finite detector resolution and other experimental effects, such as the reconstruction efficiency, the proper-

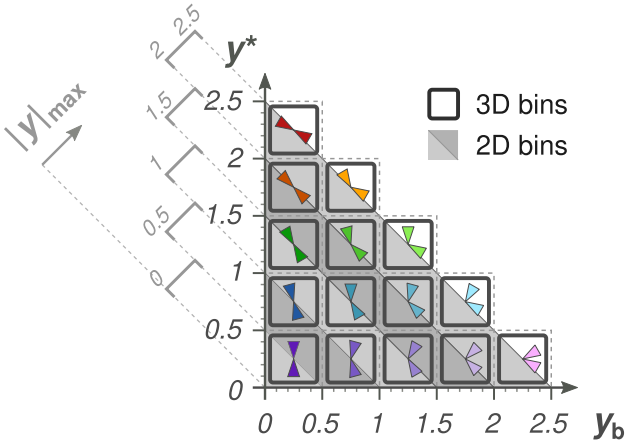

Fig. 1 Illustration of the dijet rapidity phase space, highlighting the relationship between the variables used for the 2D and 3D measurements. The colored triangles are suggestive of the orientation of the two jets in the different phase space regions in the laboratory frame, assuming that the beam line runs horizontally

ties of reconstructed jets differ from those of jets defined at the particle level. This leads to a migration of dijet events within the phase space spanned by the observables used for the cross section measurement. To enable a direct comparison of the measured cross sections to theoretical particle-level calculations or to other measurements, the effect of these migrations is accounted for as part of a multi-dimensional unfolding procedure.

Using simulated event samples, the dijet observables of interest are computed event by event based on both the two p_{T}-leading reconstructed jets and the jets clustered directly from generated particles. Response matrices are constructed to reflect the probability of bin-to-bin event migrations between the particle and reconstruction levels, taking all the observables used for a measurement into account simultaneously.

The measured event distributions are unfolded using the TUNFOLD package [29], based on the simulation-derived response matrices. While no explicit regularization of the unfolded distributions is performed, large fluctuations between neighboring bins stemming from an ill-conditioned response matrix are avoided through an appropriate choice of bins. These are chosen in such a way as to ensure that the bin sizes remain at least twice as large as the resolution in these variables, and that the purity is at the level of 50% or above. The latter is defined as the fraction of reconstructed events in each bin that originate from genuine dijet events in the same bin at the particle level.

To ensure that the unfolding problem is well-posed, a larger number of bins is chosen for the reconstructed distributions than for the particle-level distributions. Moreover, because of the larger resolution and the decrease in purity at outer rapidities, a coarser particle-level binning is chosen for the two outermost $|y|_{\mathrm{max}}$ regions for the 2D measurements, and the corresponding nine outermost (y^*, y_{b}) regions for the 3D measurements. All response matrices obtained in this way exhibit condition numbers of $\approx$3 and are thus suitable for unfolding without regularization. The condition number is defined as the absolute value of the ratio between the largest and smallest matrix eigenvalue. Figure 2 shows the responses obtained for a representative choice of jet distance parameters and dijet observables.

Aside from event migrations within the measurement phase space, contributions to each bin from spurious jet reconstructions, pileup, changes in the p_{T} ordering of jets, or migrations into the phase space, are evaluated in the simulation and proportionally subtracted from the measured distributions prior to unfolding. Similarly, to correct for event losses due to the finite reconstruction efficiency, changes in the p_{T} ordering of jets, or migrations outside the phase space, bin-by-bin correction factors are derived from simulation and applied to the unfolded distributions.

7 Experimental uncertainties

Statistical fluctuations in the observed event counts and various systematic effects give rise to experimental uncertainties in the measured cross sections. The statistical uncertainties are calculated from the event counts in each bin assuming a Poisson distribution and the corresponding covariance matrix is propagated through the unfolding procedure to yield a full set of statistical uncertainties and correlations for the unfolded cross sections. For both the 2D and 3D measurements, the statistical uncertainties remain below 2% in most phase space regions, generally increasing to 2–5% at outer rapidities and reaching values of 20–40% at large $m_{1,2}$ or $\langle p_{\mathrm{T}} \rangle_{1,2}$.

The impact of systematic effects on the cross section is generally estimated by varying experimental parameters within a ± 1 standard deviation interval around the nominal value. The relative differences to the nominal result are used to construct an asymmetric confidence interval for the unfolded cross sections in each observable bin.

Figures 3 and 4 show an overview of the main contributions to the experimental uncertainty in the dijet cross section for the 2D measurement for both values of R, and the 3D measurement as a function of $\langle p_{\mathrm{T}} \rangle_{1,2}$ for $R = 0.4$, respectively. The main contributions to the systematic uncertainty are due to the determination of the JES and JER, and the luminosity. A further uncertainty results from the correction of the trigger prefiring inefficiency, and is only significant in the outer rapidity regions with contributions from jets with $|y| > 2$. Other contributions, which have an overall smaller impact on the cross section, arise as a consequence of experimental

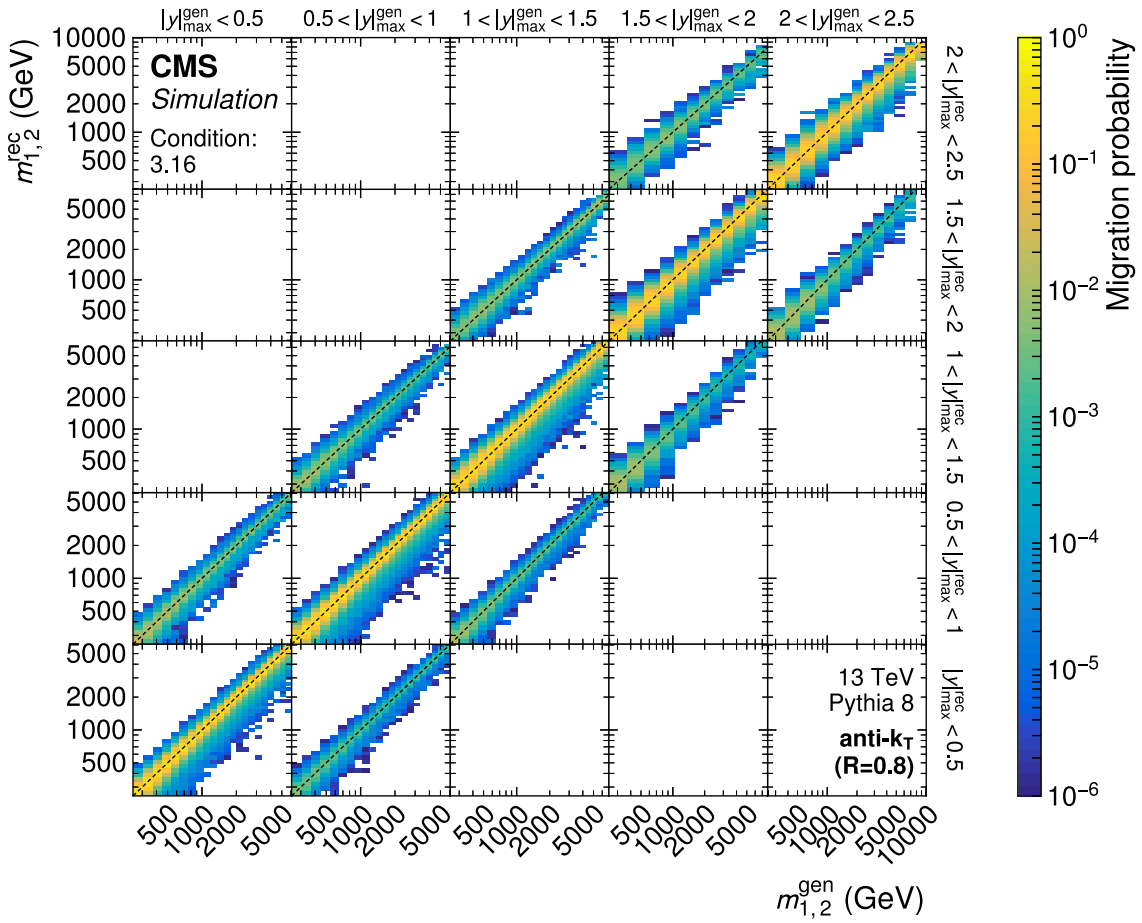

Fig. 2 Response matrix for the 2D measurement as a function of $m_{1,2}$ using jets with $R = 0.8$. The entries represent the probability for a dijet event generated in the phase space region $(m^{gen}_{1,2}, |y|^{gen}_{max})$ indicated on the x axis to be reconstructed in the phase space region $(m^{rec}_{1,2}, |y|^{rec}_{max})$ indicated on the y axis. Response matrices for all other jet sizes and observables can be found in Appendix A

methods such as unfolding. The following sections describe the individual uncertainty contributions in more detail.

7.1 Jet energy scale uncertainty

The dominant contribution to the systematic uncertainty arises from the determination of the JES. Jets are calibrated in a multi-stage procedure to correct for experimental effects, such as contributions from pileup collisions or shifts in the jet energy due to detector or reconstruction effects. The corrections depend on the p_T and η of the jet, and lead to a total uncertainty in the energy scale of individual jets of 1–2% in the phase space considered here [30]. Since the dijet spectrum decreases exponentially as a function of $m_{1,2}$ and $\langle p_T \rangle_{1,2}$, the resulting uncertainty in the measured differential dijet cross section is amplified by this exponent. For the 2D cross sections, the JES uncertainty starts at 2–5%, reaching 30% at higher values of $m_{1,2}$. For the 3D cross section the total JES uncertainty increases with $m_{1,2}$ ($\langle p_T \rangle_{1,2}$) from about 3% up to values between 8 and 60% (40%), depending on the rapidity region.

The total JES uncertainty is composed of 22 individual contributions describing different systematic effects. These include, in roughly descending order of their impact on the cross section: the change in experimental conditions over time, the calibration of the relative and absolute JES as a function of η and p_T, the change in response for jets initiated by gluons and different quark flavors, and pileup collisions. Each contribution represents a fully correlated uncertainty across all data points and is considered to be independent of the other contributions.

7.2 Luminosity uncertainty

The uncertainty due to the integrated luminosity measurement is evaluated to be 1.2% [31] in all phase space regions and is considered to be fully correlated across all bins.

7.3 Jet energy resolution uncertainty

The effect of the finite JER on the cross section is modeled using response matrices obtained from the simulation, where the effective JER is increased by factors derived from control samples in data to account for residual differences between the detector simulation and the actual data-taking conditions. The correction of the JER is applied as part of the unfolding procedure. The JER uncertainty in the cross section is estimated by performing the unfolding with response matrices derived from alternative samples, where the jet energy was smeared by factors representing a ± 1 standard deviation shift in the JER compared to the nominal value. The resulting uncertainty values range from below 1% at central rapidities to at most 10% in the outer rapidity regions, and are considered to be correlated across all data points.

7.4 Unfolding uncertainties

A further uncertainty arises as a consequence of the limited size of the simulated samples used for deriving the response matrices as part of the unfolding procedure. These are thus subject to an intrinsic statistical uncertainty, which is propagated analytically to the unfolded cross sections. In most phase space regions, this uncertainty remains below 0.5%, reaching values of 5–10% only in a small number of bins at the highest $m_{1,2}$ or $\langle p_\mathrm{T} \rangle_{1,2}$. As an estimate of the model dependence introduced by unfolding, the difference in the cross sections unfolded with response matrices obtained from PYTHIA 8 and MADGRAPH5_aMC@NLO is taken as an additional uncertainty, which is considered to be correlated across all data points. This uncertainty is typically at the level of 1%, rising up to at most 10% at outer rapidities and high $m_{1,2}$.

7.5 Other uncertainties

The correction applied to compensate for the trigger inefficiency due to prefiring gives rise to an additional correlated uncertainty in the cross section. In general, this uncertainty is at the level of 1% or below, except in the outermost $|y|_\mathrm{max}$ region and the five outermost (y^*, y_b) regions, where it rises to about 10% (20%) at the upper end of the $m_{1,2}$ ($\langle p_\mathrm{T} \rangle_{1,2}$) spectrum.

The uncertainty contribution from pileup interactions is determined by varying the total inelastic pp cross section used for reweighting the simulated samples within its associated uncertainty of 4.6%, as obtained using the pileup counting method described in Ref. [21]. The unfolding is then performed with the resulting response matrices, taking the differences between the variations and the nominal value as a fully correlated uncertainty in the unfolded cross section, which is below 1% in all phase space regions.

The normalization uncertainty in the background contribution from spurious jet reconstructions or event migrations at the phase space boundaries is estimated to be 5% and propagated through the unfolding procedure. A further contribution to the uncertainty in the unfolded cross section is due to the correction of reconstruction inefficiencies and migrations outside the measurement phase space and is estimated to be 5% of the corresponding correction factors. Each of the above contributions is considered to be fully correlated across all data points.

8 Theoretical predictions

Fixed-order theoretical predictions for the 2D and 3D dijet cross sections are obtained up to NNLO accuracy in pQCD with the NNLOJET program (revision 5918) [32]. The NNLOJET program is interfaced to FASTNLO (version 2.3) [33,34] via the APPLFAST interface (version 0.0.46) [35,36] to provide interpolation grids that allow theoretical predictions to be obtained for arbitrary PDFs and for different values of the renormalization scale μ_R, the factorization scale μ_F, and the strong coupling constant $\alpha_\mathrm{S}(m_\mathrm{Z})$, without the need to repeat the full calculation.

Following recommendations outlined in Ref. [3], $m_{1,2}$ is chosen as the central reference value for both μ_R and μ_F. To estimate the theoretical uncertainty due to missing higher-order terms in perturbation theory, the conventional recipe [37–39] of varying the μ_R and μ_F scales is applied. More precisely, the so-called scale uncertainty is derived from the envelope of the theoretical predictions obtained for the six scale variations corresponding to $(\mu_\mathrm{R}/m_{1,2}, \mu_\mathrm{F}/m_{1,2})$ = (1/2, 1/2), (1/2, 1), (1, 1/2), (2, 1), (1, 2), and (2, 2). As an example, Fig. 5 shows the resulting uncertainty for theoretical predictions of the 2D and 3D dijet cross sections obtained at LO, next-to-leading order (NLO), and NNLO. In most phase space regions, the NLO and NNLO scale uncertainty bands overlap, indicating good perturbative convergence. However, towards small values of $m_{1,2}$ and large rapidity separations y^*, a steep rise in the ratio of the higher-order predictions with respect to LO, referred to here as the K factors, is observed, leading to a reduced overlap and an increased scale uncertainty. For an ideal dijet event with two jets of equal p_T produced in a back-to-back configuration, the dijet invariant mass is given by $m_{1,2} = 2p_\mathrm{T}\cosh(y^*)$. The rise in the K factors then is understood to be caused by the minimum p_T requirements imposed on the two leading jets, which at small dijet mass restrict the phase space accessible to LO processes in favor of higher-order contributions.

The NNLO contribution is based on the leading-color and leading-flavor-number approximation [3,4]. Subleading-color contributions have been shown to be at the percent level at NLO and are expected to be even smaller in comparison

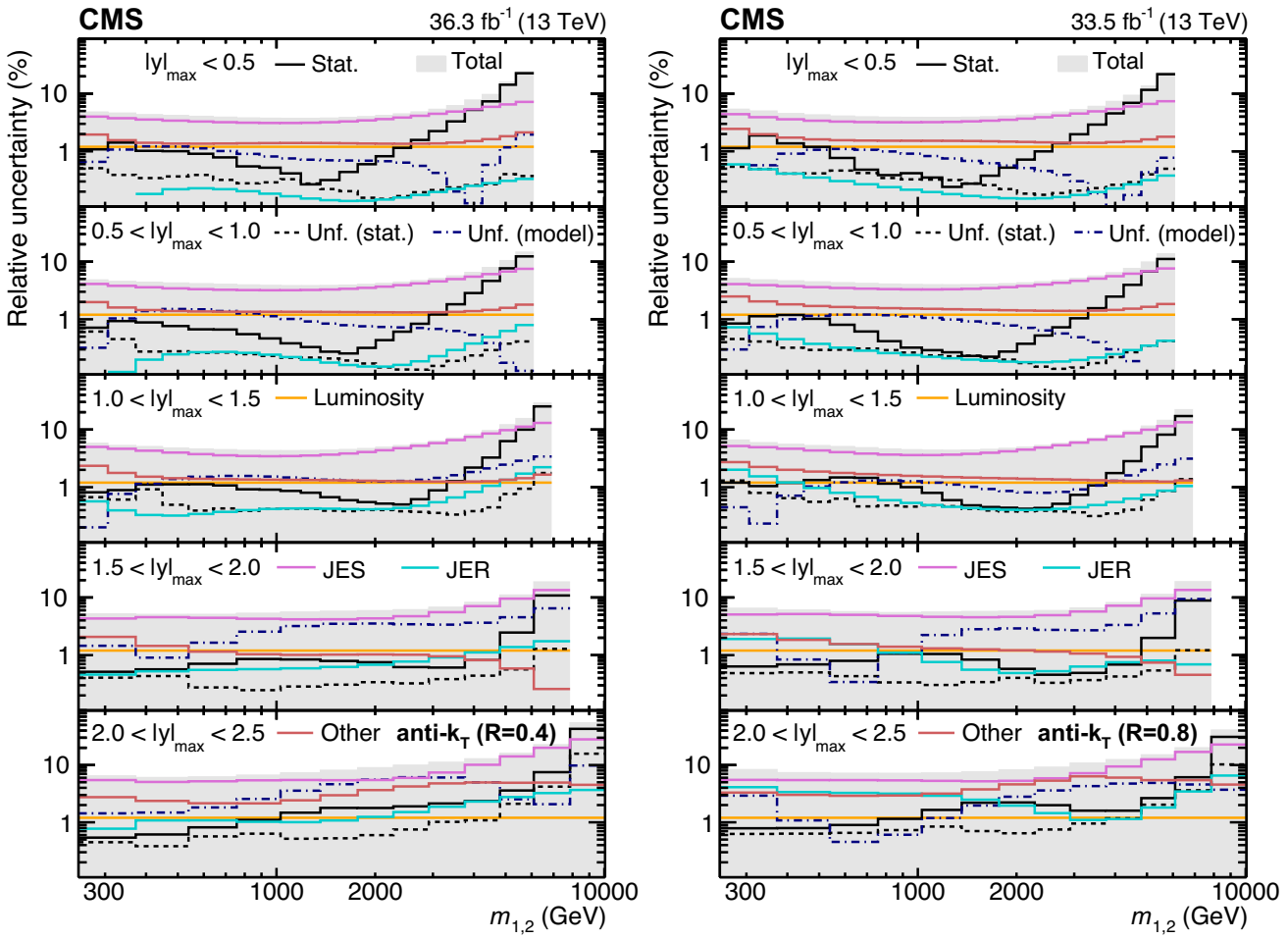

Fig. 3 Breakdown of the experimental uncertainty for the 2D measurements as a function of $m_{1,2}$ using jets with $R = 0.4$ (left) and 0.8 (right). The individual components and abbreviations are explained in Sect. 7. The abbreviation "Unf." refers to the unfolding uncertainties. The shaded area represents the sum in quadrature of all statistical and systematic uncertainty components

to the leading-color result at NNLO [40]. It is worth noting, however, that in a recent investigation [41] a significant impact of subleading-color contributions was found for the NNLO prediction of the $\langle p_T \rangle_{1,2}$-dependent 3D CMS dijet measurement at $\sqrt{s} = 8$ TeV with a jet distance parameter $R = 0.7$ [5]. The reported effect can lead to a decrease in the cross section of up to 5% for small $\langle p_T \rangle_{1,2}$ and an increase of up to 3% for large $\langle p_T \rangle_{1,2}$, which is beyond the size of the scale uncertainty at NNLO. For the CMS inclusive jet measurement at $\sqrt{s} = 13$ TeV [42] with jet distance parameters of $R = 0.4$ and 0.7, the effect was determined to be much smaller and to be covered by scale uncertainty estimates, except towards small jet p_T for the smaller jet size. Predictions for the 2D dijet measurement performed as a function of $m_{1,2}$ and y^* at $\sqrt{s} = 7$ TeV by the ATLAS Collaboration [11] were also less affected even with $R = 0.4$. The effect on the dijet observables under examination here is not yet known. The 2D and 3D measurements presented here for two jet distance parameters, $R = 0.4$ and 0.8, and for the two dijet observables $m_{1,2}$ and $\langle p_T \rangle_{1,2}$, provide an ideal set of measurements to further study the impact of subleading-color corrections in comparison to data.

To compare with CMS data unfolded to the particle level, the fixed-order predictions are complemented by nonperturbative (NP) correction factors c_{NP}, which are defined as the ratio between the nominal cross sections with and without multiple parton interactions (MPI) and hadronization (HAD) effects, as given by a chosen MC event generator,

$$c_{NP} = \frac{\sigma^{PS+MPI+HAD}}{\sigma^{PS}}, \tag{6}$$

where the parton shower (PS) is considered to be a perturbative component.

The model dependence of the NP corrections is evaluated by comparing results from several MC event generators.

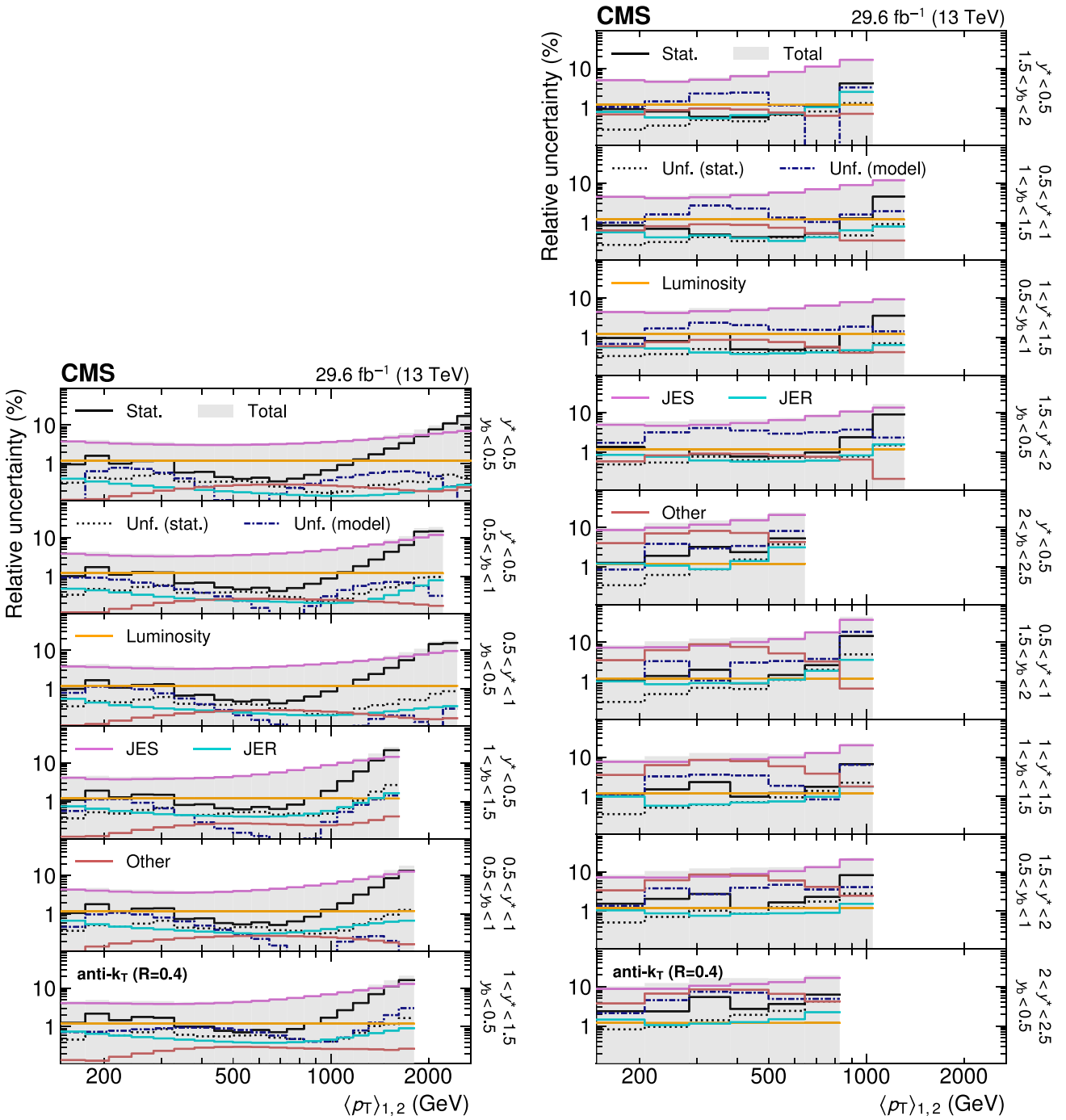

Fig. 4 Breakdown of the experimental uncertainty for the 3D measurement as a function of $\langle p_T \rangle_{1,2}$ using jets with $R = 0.4$. The individual components and abbreviations are explained in Sect. 7. The shaded area represents the sum in quadrature of all statistical and systematic uncertainty components. Similar plots for all other jet sizes and observables can be found in Appendix B

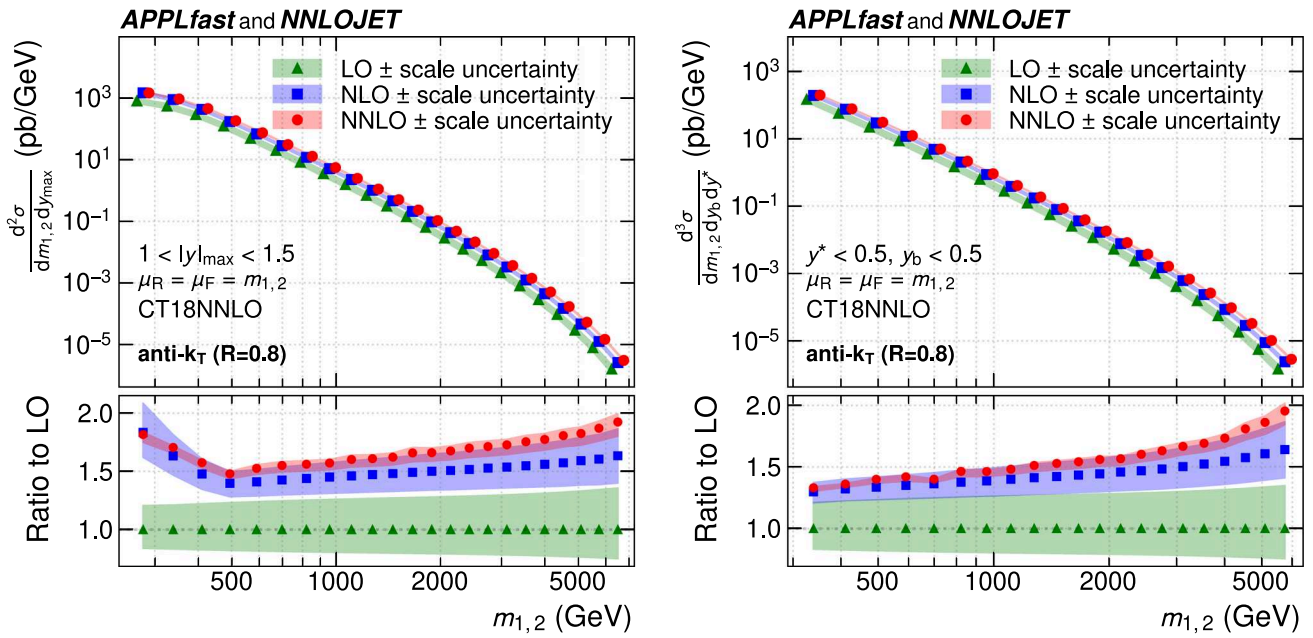

Fig. 5 Theoretical predictions for the 2D (left) and 3D (right) cross sections, as a function of $m_{1,2}$, illustrated here in the rapidity regions $1.0 < |y|_{\max} < 1.5$ and $y_b < 0.5$, $y^* < 0.5$, together with the corresponding six-point scale uncertainty for $\mu_R = \mu_F = m_{1,2}$ using the CT18 NNLO PDF set. In the left panels, the curves and symbols are slightly shifted for better visibility. The right panels show the ratio to the respective prediction at LO. The fluctuations in the NNLO predictions are due to the limited statistical precision of the calculation

Leading-order particle-level predictions are obtained from PYTHIA (version 8.240), using the tunes CUETP8M1 [18] and CUETP8M2T4 [43], and HERWIG++ [44] (version 2.7.1) using the EE5C tune [45]. These generators are interfaced to POWHEG [46–49] (version 2J V2_Mar2016) to provide NLO predictions. An additional set of predictions is obtained from HERWIG 7 [50] (version 7.2.2) with the CH3 tune [51] at both LO and NLO.

To mitigate statistical fluctuations, the corrections are parametrized by a smooth function $f(x) = a/x^b + c$, where x is either $m_{1,2}$ or $\langle p_T \rangle_{1,2}$. The parameters a, b, and c are obtained in a least-squares fit to the binwise correction factors c_{NP} obtained from Eq. (6) in each rapidity region. The fits provide a good description of the correction factors in most phase space regions. For a number of low-$m_{1,2}$ bins, where the phase space is constrained by the minimum p_T requirements on the two leading jets, the value of c_{NP} is taken directly as the correction factor. The final correction factor in each bin is obtained as the midpoint between the largest and smallest value of c_{NP} obtained across all MC configurations, and half the difference between the largest and smallest value is assigned as an uncertainty.

The resulting NP corrections are illustrated in Fig. 6. For jets with $R = 0.4$, the contributions from hadronization and MPI largely cancel, leading to NP corrections compatible with unity within their uncertainty. In contrast, the MPI contribution dominates for jets with $R = 0.8$, resulting in significantly larger NP corrections of ≈20% at low values of $m_{1,2}$. The size of the uncertainty is similar for both jet sizes.

It is also observed that the NP corrections obtained with PYTHIA 8 are in general larger than those from HERWIG++ or HERWIG 7, such that this difference is the dominant contribution to the NP correction uncertainty. While some dependence on the tune is observed when comparing the predictions from CUETP8M1 and CUETP8M2T4, the impact is typically small. In most cases, the values obtained at NLO are seen to be comparable to those obtained at LO from the same generator, with the notable exception of HERWIG++, where the NLO result obtained using POWHEG is consistently higher than the LO result.

For jet transverse momenta in the TeV range, electroweak contributions to the differential dijet cross section become important and must be considered in addition to the NNLO pQCD calculation [52]. These effects, which arise from the virtual exchange of soft or collinear W or Z bosons, are accounted for by applying a multiplicative correction factor to the pQCD prediction. As shown in Fig. 7, these factors exhibit a strong dependence on the rapidity and p_T of the jets. Particularly at small $|y|_{\max}$ or y^*, the electroweak correction reaches 10–20% for dijet masses beyond 5 TeV, where experimental uncertainties become large as well. The uncertainty on this correction is therefore considered to be negligible with respect to other large uncertainties.

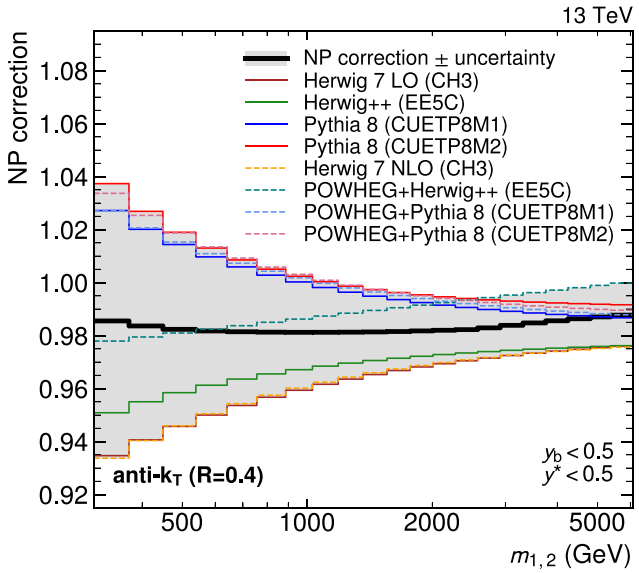

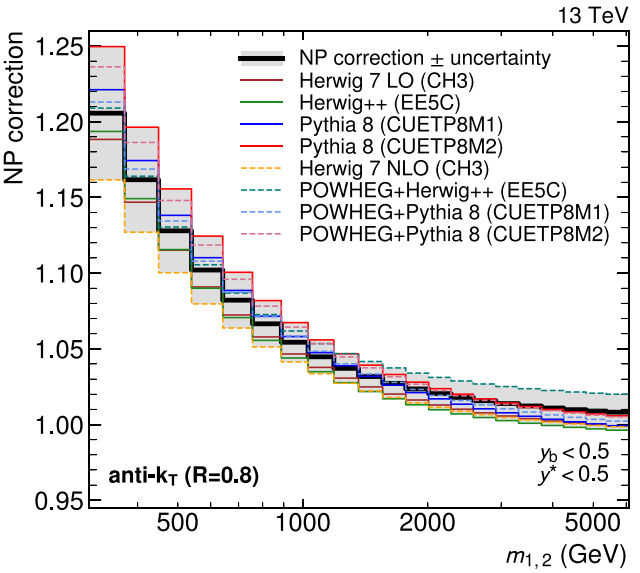

Fig. 6 Nonperturbative correction factors obtained for jets with $R = 0.4$ (left) and 0.8 (right) as a function of $m_{1,2}$, illustrated here in the rapidity region ($y_b < 0.5$, $y^* < 0.5$). Individual correction factors are first derived from simulation using eight different MC configurations. The largest and smallest value obtained in each observable bin is then used to define the final correction factor and its associated uncertainty. The correction values are larger for jets with $R = 0.8$, increasing to over 20% in the lowest $m_{1,2}$ bin

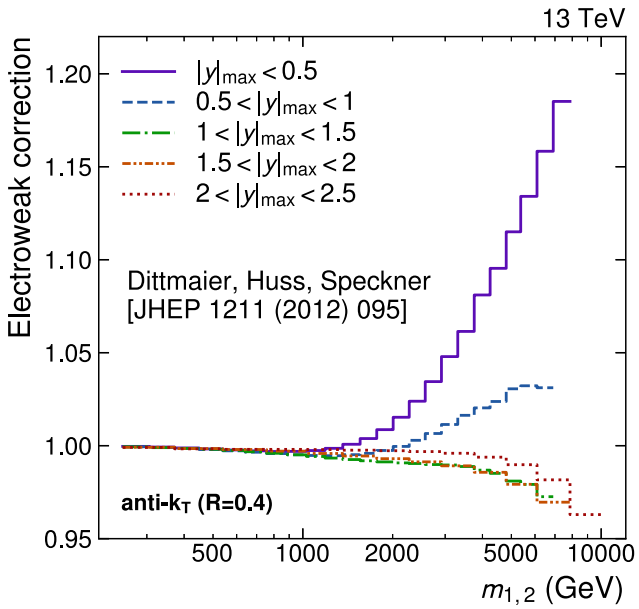

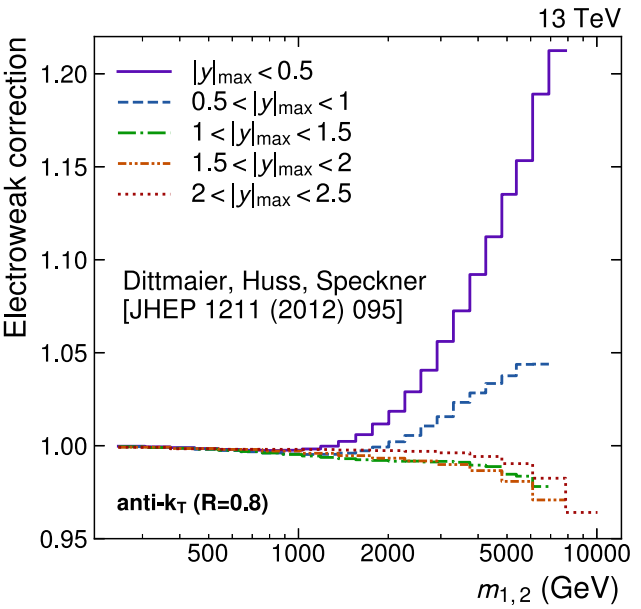

Fig. 7 Electroweak correction factors obtained for jets with $R = 0.4$ (left) and 0.8 (right) as a function of $m_{1,2}$ in the five different $|y|_{max}$ regions. The corrections depend strongly on the kinematic properties of the jets and are observed to be largest at central rapidities for $m_{1,2} > 1$ TeV

9 Comparison to theory

An overview of the unfolded cross sections obtained for the 2D and 3D measurements and the corresponding fixed-order theoretical predictions at NNLO, complemented by NP and electroweak corrections, is presented in Fig. 8. For a more detailed comparison, ratios of the measured cross sections to the theoretical predictions are shown in Figs. 9 and 10.

The theoretical predictions are obtained using recent NNLO PDF sets available via the LHAPDF [53] library (version 6.3.0), namely ABMP16 [54], CT18 [55], MSHT20 [56], and NNPDF3.1 [57]. All PDF sets are derived in global fits to data from multiple experiments while fixing the value of the strong coupling constant $\alpha_S(m_Z)$ to 0.118, except for ABMP16, where $\alpha_S(m_Z) = 0.1147$ is determined in the fit together with all other parameters. The uncertainties in the

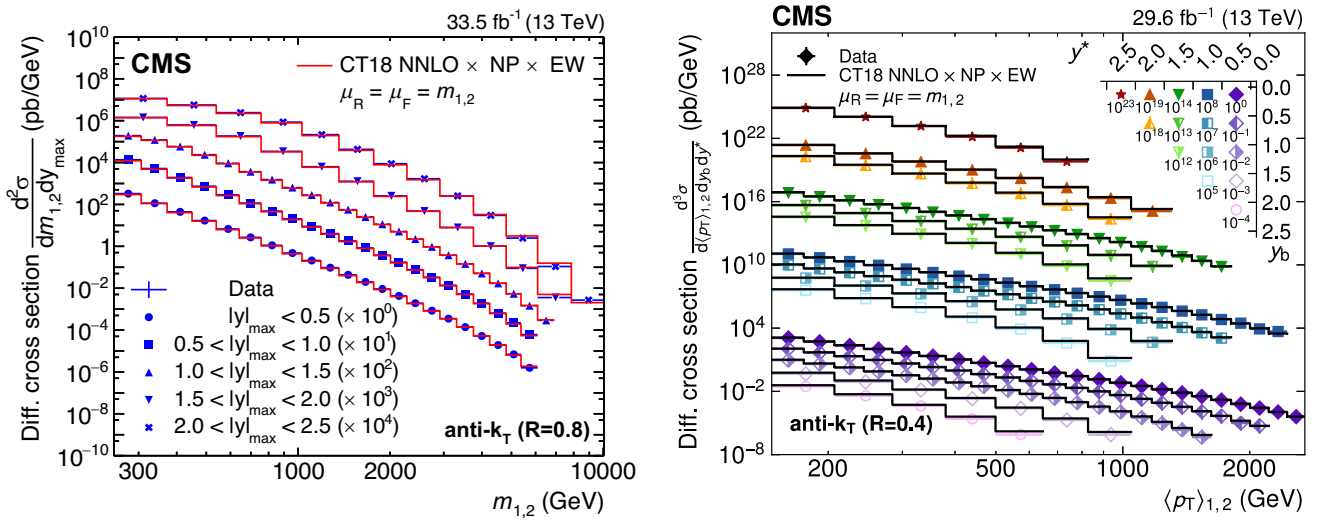

Fig. 8 Differential dijet cross sections, illustrated here for the 2D measurement as a function of $m_{1,2}$ using jets with $R = 0.8$ (left), and the 3D measurement as a function of $\langle p_T\rangle_{1,2}$ using jets with $R = 0.4$ (right). The markers and lines indicate the measured unfolded cross sections and the corresponding NNLO predictions, respectively. For better visibility, the values are scaled by a factor depending on the rapidity region, as indicated in the legend. Analogous plots for all other jet sizes and observables can be found in Appendix B

cross section predictions due to the PDFs are calculated as 68% confidence intervals following the prescriptions given in the respective references. The PDF uncertainty bands shown in Fig. 10 are obtained using the CT18 PDF set and do not account for the finite precision of $\alpha_S(m_Z)$.

The predictions for different PDFs are generally in agreement with each other within the PDF uncertainties, except for the AMBP16 PDF, for which the predicted cross sections are generally smaller than those for other PDFs. At large $m_{1,2}$ or $\langle p_T\rangle_{1,2}$, the predictions obtained for the different PDF sets show a diverging trend, while still remaining compatible within the PDF uncertainties.

The level of agreement between the theoretical predictions and the data is observed to be good in most phase space regions, with some deviations at the lower ends of the spectra and in the outer rapidity regions. In general, the theoretical predictions for $R = 0.8$ are observed to provide a better description of the data than for $R = 0.4$, which is consistent with past observations [42,58–61].

10 The QCD analysis

To evaluate the impact of the present measurements on determinations of the proton PDFs and the strong coupling constant, a QCD analysis is performed following the approach taken by earlier HERAPDF analyses [1,2,62]. The data used in the QCD analysis comprise DIS measurements [1,2] obtained in $e^{\pm}p$ collisions at the HERA collider experiments H1 and ZEUS as a function of the momentum transfer Q^2, supplemented by the present measurements of the dijet cross section.

The HERA measurements correspond to charged-current (CC) DIS data collected in e^-p and e^+p collisions at a proton beam energy of $E_p = 920$ GeV, and neutral-current (NC) DIS data collected in e^+p collisions at proton beam energies of $E_p = 460$, 575, 820, and 920 GeV. Only data points with Q^2 values above a threshold $Q^2_{min} = 10\,\text{GeV}^2$ are included, to ensure a good description of the measurements by the theoretical predictions.

It is well known that fixed-order predictions work most reliably for inclusive observables, i.e., where the phase space for QCD radiation is not restricted. Such restrictions – as for example the choice of a small distance parameter R for jet clustering – introduce disparities in the cancellation of singularities between real emissions and virtual corrections, leading to large logarithmic terms that have a negative impact on the perturbative convergence and would require resummation [63]. Moreover, as discussed in Sect. 8, there are indications that subleading-color corrections might have a smaller impact for larger values of R, and for $m_{1,2}$ as compared to $\langle p_T\rangle_{1,2}$. Thus, to profit most from the available predictions at NNLO, only the dijet cross sections as a function of $m_{1,2}$ for the larger value of $R = 0.8$ are used in the QCD analysis.

Theoretical predictions for the dijet cross sections are obtained from NNLOJET and FASTNLO as interpolation grids at NNLO accuracy, taking into account the full dependence of the NNLO cross sections on the PDFs, the strong coupling constant, μ_R, and μ_F. Following Ref. [3], the dijet invariant mass $m_{1,2}$ is chosen as the central value for both μ_R and

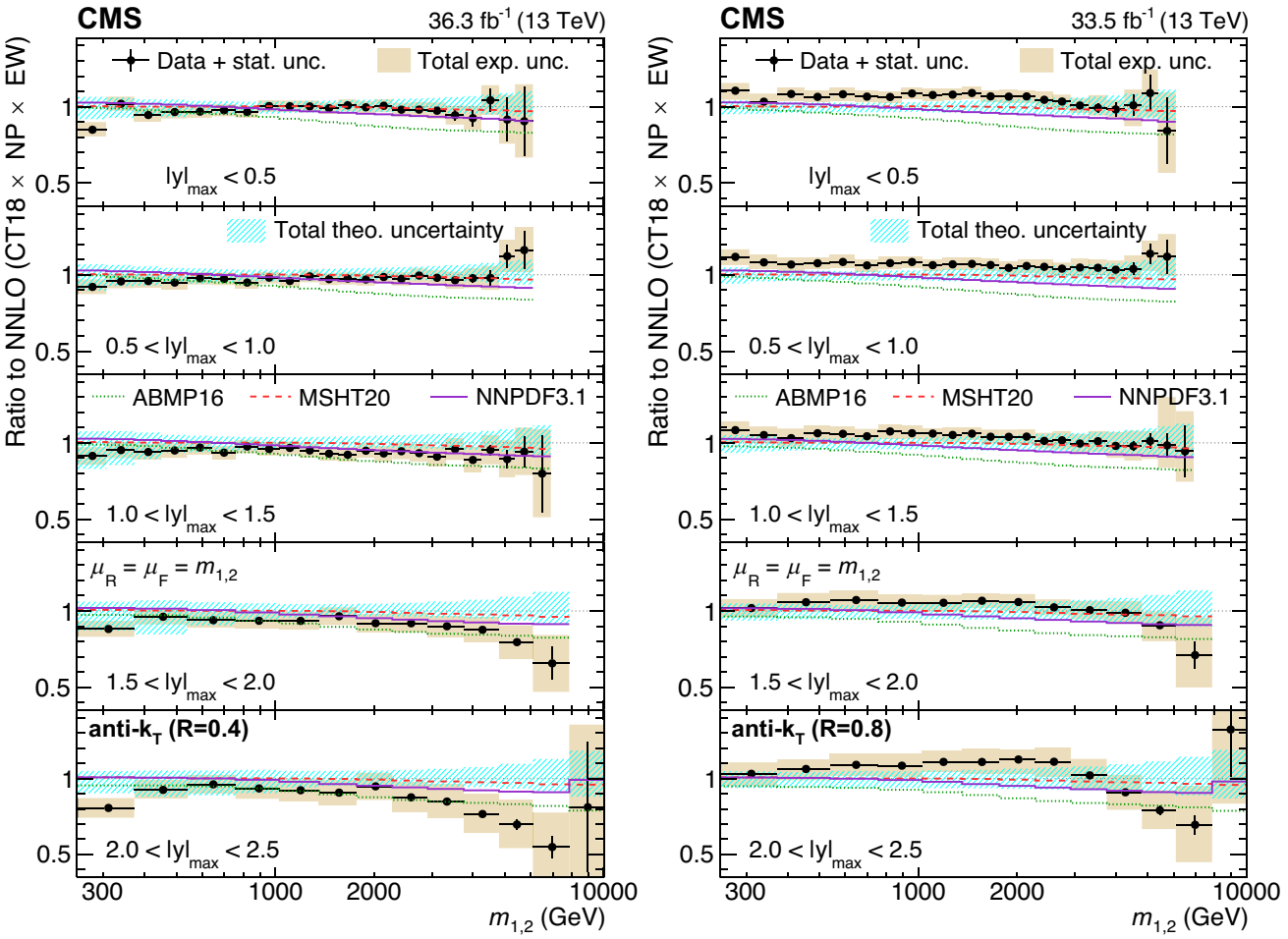

Fig. 9 Comparison of the 2D dijet cross section as a function of $m_{1,2}$ to fixed-order theoretical calculations at NNLO, using jets with $R = 0.4$ (left) and 0.8 (right). Shown are the ratios of the measured cross sections (markers) to the predictions obtained using the CT18 NNLO PDF set. The error bars and shaded yellow regions indicate the statistical and the total experimental uncertainties of the data, respectively, and the hatched teal band indicates the sum in quadrature of the PDF, NP, and scale uncertainties. Alternative theoretical predictions obtained using other global PDF sets are shown as colored lines. Similar plots for the individual rapidity regions can be found in Appendix B

μ_F. The cross sections are corrected additionally for NP and electroweak effects as described in Sect. 8.

Simultaneous determinations of PDFs and the strong coupling constant at the scale of the Z boson mass, $\alpha_S(m_Z)$, are performed with the xFitter program (version 2.0.1) [64,65], using the HERA data together with either the 2D or 3D dijet cross sections as inputs. Access to the theoretical predictions for the dijet cross sections is provided by fastNLO. The evolution of PDFs following the DGLAP equations [66–68] is performed using the QCDNUM package (version 17-01/15) [69]. Contributions from heavy quarks are treated in the Thorne–Roberts optimal variable flavor number scheme (RTOPT) [70–72], with the masses of the charm and bottom quarks set to $m_c = 1.43\,\text{GeV}$ and $m_b = 4.5\,\text{GeV}$, respectively.

In the HERAPDF approach, the proton structure is expressed in terms of the gluon distribution $g(x)$, the up and down valence quark distributions $u_v(x)$ and $d_v(x)$, and the up- and down-type sea antiquark distributions $\overline{U}(x)$ and $\overline{D}(x)$. For each of these distributions f, the dependence on the proton momentum fraction x carried by a parton is parametrized at a starting scale $\mu^2_{F,0} = 1.9\,\text{GeV}^2$ as

$$x f(x, \mu^2_{F,0}) = A_f\, x^{B_f}\, (1-x)^{C_f}\, (1 + D_f\, x + E_f\, x^2). \quad (7)$$

The overall normalization of the PDFs is given by the A parameters, with A_{u_v}, A_{d_v}, and A_g being constrained by the quark number and momentum sum rules. The B and C parameters control the shape of the distribution as x approaches the edges of its domain at 0 and 1, respectively. The D and E parameters represent additional degrees of freedom related to the functional forms.

The sea quark contributions are given by $\overline{U}(x) = \bar{u}(x)$ and $\overline{D}(x) = \bar{d}(x) + \bar{s}(x)$, where $\bar{u}(x)$, $\bar{d}(x)$, and $\bar{s}(x)$ refer to

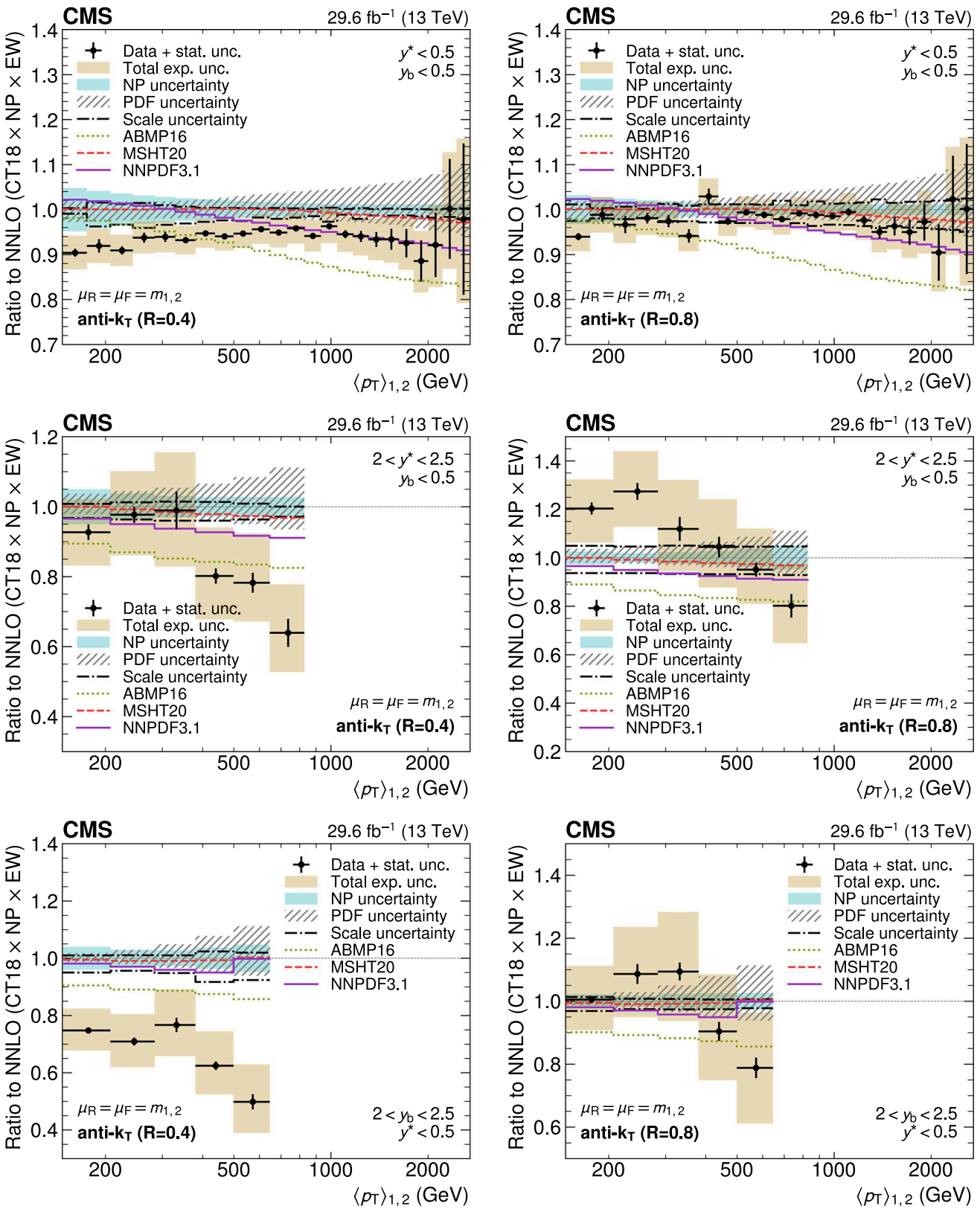

Fig. 10 Comparison of the 3D dijet cross section for jets with $R = 0.4$ (left) and 0.8 (right) as a function of $\langle p_T \rangle_{1,2}$ to fixed-order theoretical calculations at NNLO, shown here for three out of the total of 15 rapidity regions. The data points and predictions for alternative PDFs are analogous to those in Fig. 9. In addition, the separate contributions to the theory uncertainty due to the CT18 PDFs, NP corrections, and six-point scale variations are shown explicitly. Similar plots for all rapidity regions and observables can be found in Appendix B

the distribution of up, down, and strange antiquarks, respectively. A fixed overall normalization ratio is imposed by the requirement $A_{\overline{\mathrm{U}}} = A_{\overline{\mathrm{D}}}(1 - f_{\mathrm{s}})$, where the strangeness fraction is given by $f_{\mathrm{s}} = \bar{\mathrm{s}}/(\bar{\mathrm{s}} + \bar{\mathrm{d}})$ and set to 0.4 following Ref. [2]. To enforce a similar behavior of the quark sea as $x \to 0$, the requirement $B_{\overline{\mathrm{U}}} = B_{\overline{\mathrm{D}}}$ is imposed. The total sea quark distribution is defined as $\Sigma(x) = 2\left(\overline{\mathrm{U}}(x) + \overline{\mathrm{D}}(x)\right)$.

The above constraints result in a total of ten A, B, and C parameters whose values are determined during the fit procedure. Additional D and E parameters are included where it is found that these lead to an improved fit quality in terms of the total χ^2 value, following the procedure outlined in Ref. [2]. Starting from the initial parametrization with no additional parameters, the change in χ^2 resulting from the inclusion of any of the remaining D and E parameters in the fit is evaluated. The parameter resulting in the largest decrease in χ^2 is added to the parametrization, and the procedure is repeated until no further significant improvement is observed. The final parametrization obtained in this way for the fits including the CMS dijet measurements is given by:

$$
\begin{aligned}
x\,\mathrm{g}(x, \mu_{\mathrm{F},0}^2) &= A_{\mathrm{g}}\, x^{B_{\mathrm{g}}}(1-x)^{C_{\mathrm{g}}},\\
x\,\mathrm{u_v}(x, \mu_{\mathrm{F},0}^2) &= A_{\mathrm{u_v}}\, x^{B_{\mathrm{u_v}}}(1-x)^{C_{\mathrm{u_v}}}(1 + D_{\mathrm{u_v}} x + E_{\mathrm{u_v}} x^2),\\
x\,\mathrm{d_v}(x, \mu_{\mathrm{F},0}^2) &= A_{\mathrm{d_v}}\, x^{B_{\mathrm{d_v}}}(1-x)^{C_{\mathrm{d_v}}},\\
x\,\overline{\mathrm{U}}(x, \mu_{\mathrm{F},0}^2) &= A_{\overline{\mathrm{U}}}\, x^{B_{\overline{\mathrm{U}}}}(1-x)^{C_{\overline{\mathrm{U}}}}(1 + D_{\overline{\mathrm{U}}} x),\\
x\,\overline{\mathrm{D}}(x, \mu_{\mathrm{F},0}^2) &= A_{\overline{\mathrm{D}}}\, x^{B_{\overline{\mathrm{D}}}}(1-x)^{C_{\overline{\mathrm{D}}}}.
\end{aligned}
\tag{8}
$$

Uncertainties in the fitted PDFs are determined using a similar procedure as the one described in Ref. [62]. Separate contributions for *fit*, *model*, *scale*, and *parametrization* uncertainties are obtained as described in the following.

The fit uncertainty represents the propagation to the PDFs of the uncertainties in the input measurements, theoretical predictions, and theory correction factors. It is estimated following the MC method outlined in Refs. [73,74], whereby a large number of alternative fits (MC replicas) are performed with random variations of the input data according to their statistical and systematic uncertainties, taking the standard deviation of the resulting PDFs as an estimate of the fit uncertainty.

An alternative estimate for the fit uncertainty is obtained via the Hessian method [75] and found to be comparable to the MC fit uncertainty in most cases, apart from the $\mathrm{u_v}$ distribution, where it is found that the fit uncertainty is significantly underestimated by the Hessian method at $x < 0.1$. This is understood to be a consequence of the more flexible parametrization of $\mathrm{u_v}$ resulting from the parametrization scan, which is driven by the high-x region where the input data are constraining.

Table 2 Nominal values and variations of parameters used to determine the PDF model uncertainty. Variations marked with an asterisk are in conflict with the requirement $\mu_{\mathrm{F},0} < m_{\mathrm{c}}$ and thus cannot be used directly for the uncertainty estimation. Following Ref. [62], the results obtained for the opposite variation are symmetrized in these cases

Parameter	Nominal value	Variations	
		down	*up*
Q^2_{min} (GeV^2)	10	7.5	12.5
f_{s}	0.4	0.3	0.5
m_{c} (GeV)	1.43	*1.37**	1.49
m_{b} (GeV)	4.5	4.25	4.75
$\mu^2_{\mathrm{F},0}$ (GeV^2)	1.9	1.6	*2.2**

The model uncertainty arises from the choices made for the values of certain non-PDF parameters: the minimum Q^2 value used for restricting the HERA data, the strangeness fraction f_{s}, the charm and bottom quark masses m_{c} and m_{b}, and the value of the starting scale $\mu_{\mathrm{F},0}$. It is estimated by varying the values of these parameters up and down from their nominal values as indicated in Table 2, and adding the differences to the nominal fit result in quadrature separately for each variation direction.

A further uncertainty arises because of the choice of PDF parametrization. It is estimated by performing alternative fits that include one additional D or E parameter compared to the nominal parametrization. The maximum deviation between the nominal PDF and those obtained from the alternative parametrizations is taken as an additional parametrization uncertainty.

Finally, a scale uncertainty is estimated to account for missing higher orders in perturbation theory by varying μ_{R} and μ_{F} as described in Sect. 8. The envelope of the PDFs obtained with these alternative scale choices is defined as the scale uncertainty.

As discussed in Sect. 9, the level of agreement between the data and the theoretical predictions obtained with various global PDF sets varies according to the phase space region and is generally worse at outer rapidities. For the PDF determinations performed using the present data, a poor fit quality is observed in a small number of rapidity regions at high $|y|_{\mathrm{max}}$, y^* or y_{b}, with the partial χ^2 divided by the number of data points reaching values of $\approx$3.

The effect of including these regions in the PDF determinations is investigated by comparing to fits performed with only a subset of rapidity regions, in which the data are well described by the theoretical predictions. While this results in an increased fit uncertainty, a sizable reduction in the parametrization uncertainty – and to a lesser extent the scale

Table 3 Goodness-of-fit values for the fits to the HERA DIS data alone, and together with the CMS dijet measurements, using the PDF parametrization given in Eq. 8. The table shows the partial χ^2 values divided by the number of data points for the HERA DIS datasets and each of the dijet rapidity regions. The total χ^2 value, divided by the number of degrees of freedom, is given at the bottom of the table

		Partial χ^2 / n_{data}		
		HERA DIS	HERA DIS + CMS 13 TeV dijets	
Data set			2D	3D
CMS dijet 2D				
$\lvert y\rvert_{\max} < 0.5$			18 / 22	
$0.5 < \lvert y\rvert_{\max} < 1$			15 / 22	
$1 < \lvert y\rvert_{\max} < 1.5$			16 / 23	
$1.5 < \lvert y\rvert_{\max} < 2$			15 / 12	
CMS dijet 3D				
$y_b < 0.5$,	$y^* < 0.5$			22 / 21
$y_b < 0.5$,	$0.5 < y^* < 1$			24 / 19
$0.5 < y_b < 1$,	$y^* < 0.5$			49 / 19
$0.5 < y_b < 1$,	$0.5 < y^* < 1$			13 / 17
$0.5 < y_b < 1$,	$1 < y^* < 1.5$			8 / 7
$1 < y_b < 1.5$,	$0.5 < y^* < 1$			10 / 7
$0.5 < y_b < 1$,	$1.5 < y^* < 2$			9 / 6
$1 < y_b < 1.5$,	$1 < y^* < 1.5$			4 / 6
$1.5 < y_b < 2$,	$0.5 < y^* < 1$			8 / 5
HERA1+2				
CC e^-p, $E_p = 920$ GeV		51 / 42	51 / 42	50 / 42
CC e^+p, $E_p = 920$ GeV		37 / 39	37 / 39	38 / 39
NC e^-p, $E_p = 920$ GeV		221 / 159	222 / 159	221 / 159
NC e^+p, $E_p = 460$ GeV		198 / 177	197 / 177	198 / 177
NC e^+p, $E_p = 575$ GeV		186 / 221	186 / 221	186 / 221
NC e^+p, $E_p = 820$ GeV		55 / 61	55 / 61	55 / 61
NC e^+p, $E_p = 920$ GeV		359 / 317	364 / 317	362 / 317
Total χ^2/n_{dof}		1161 / 1003	1232 / 1081	1339 / 1109

uncertainty – is achieved for the restricted fits. Consequently, the fit results are derived with the chosen subset of rapidity regions, which are indicated in Table 3 along with the total and partial χ^2 values, which are close to unity in most rapidity regions, except for the bin $0.5 < y_b < 1$, $y^* < 0.5$. The results of fits including all rapidity regions are provided for reference in Appendix A.

The PDFs resulting from the fits including the CMS dijet measurements are shown in Fig. 11, along with the different uncertainty contributions. The PDFs obtained with the inclusion of the 2D data are compatible with those obtained from the 3D data within the total uncertainty, which is obtained by adding together the parametrization uncertainty and the sum in quadrature of the fit, model, and scale uncertainty contributions. For most of the distributions, a smaller fit uncertainty is obtained in the 3D fit compared to the 2D one, while the model uncertainty is of a similar size, and the scale and parametrization uncertainties are slightly larger for the 3D fit in certain x regions.

To evaluate the impact of the present measurements on the PDF determination, fits are performed using the HERA DIS data alone, using the same PDF parametrization as for the fits including the dijet measurements. Figure 12 shows a comparison between the PDFs obtained using only the HERA DIS data, and those obtained when fitting the CMS dijet data in addition, along with the respective fit uncertainties. The distributions obtained with and without the inclusion of the dijet measurements are observed to be compatible with each other, and a general reduction in the fit uncertainty is observed when the CMS data is included in the fit. In particular, the precision of the gluon PDF is improved for parton momentum fractions $x > 0.1$, where the uncertainty is reduced by up to a factor of ≈ 2 by the inclusion of the dijet measurements. The

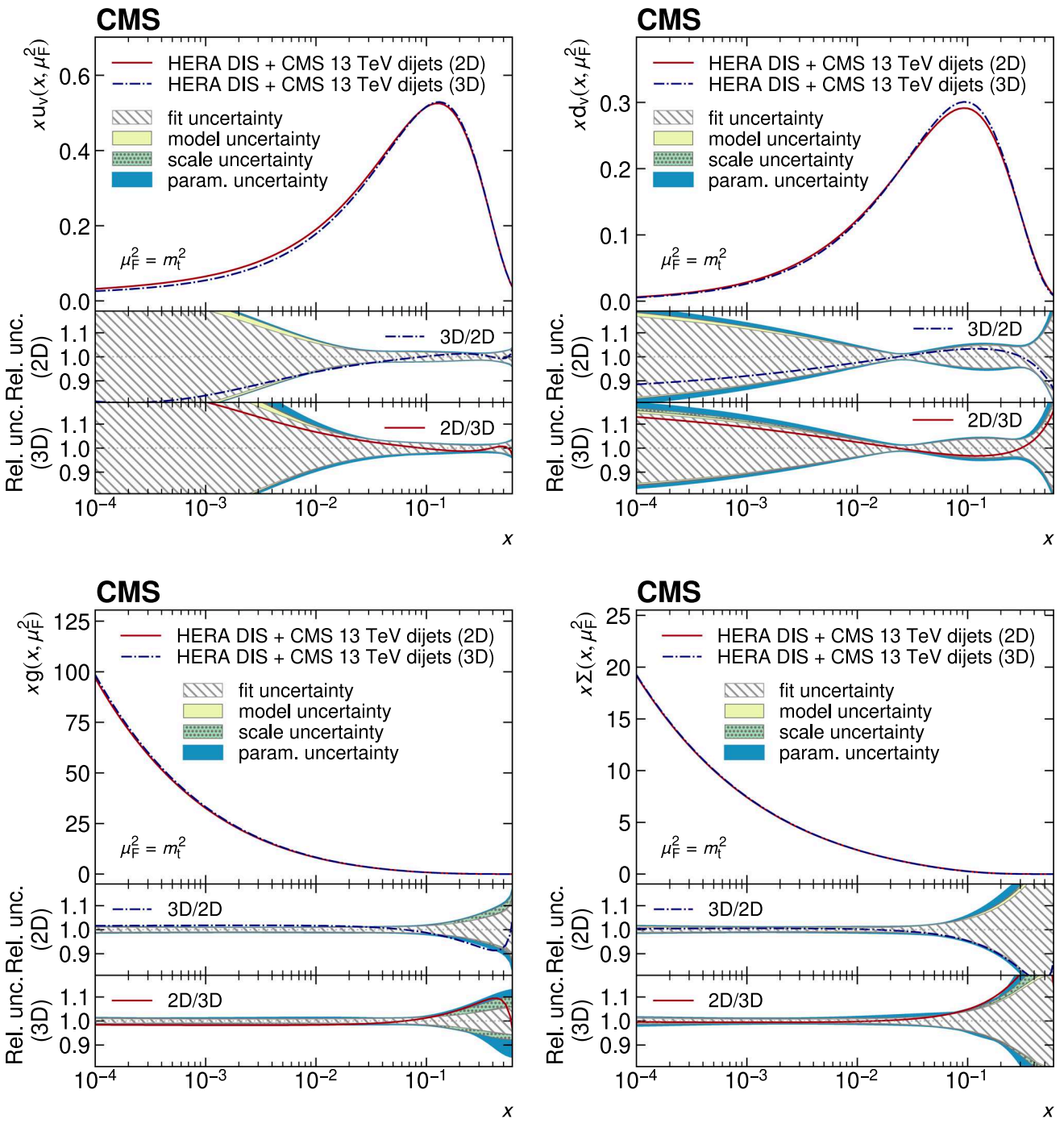

Fig. 11 Parton distributions obtained in a fit to HERA DIS data together with the CMS 2D or 3D dijet measurements. The top panels show the PDFs of the up and down valence quarks (upper row), of the gluon (lower left), and of the total sea quarks (lower right) as a function of the fractional parton momentum x at a factorization scale equal to the top quark mass. The middle (lower) panels show the relative uncertainty contributions obtained for the 2D (3D) fit, as well as the ratios of the fitted central values

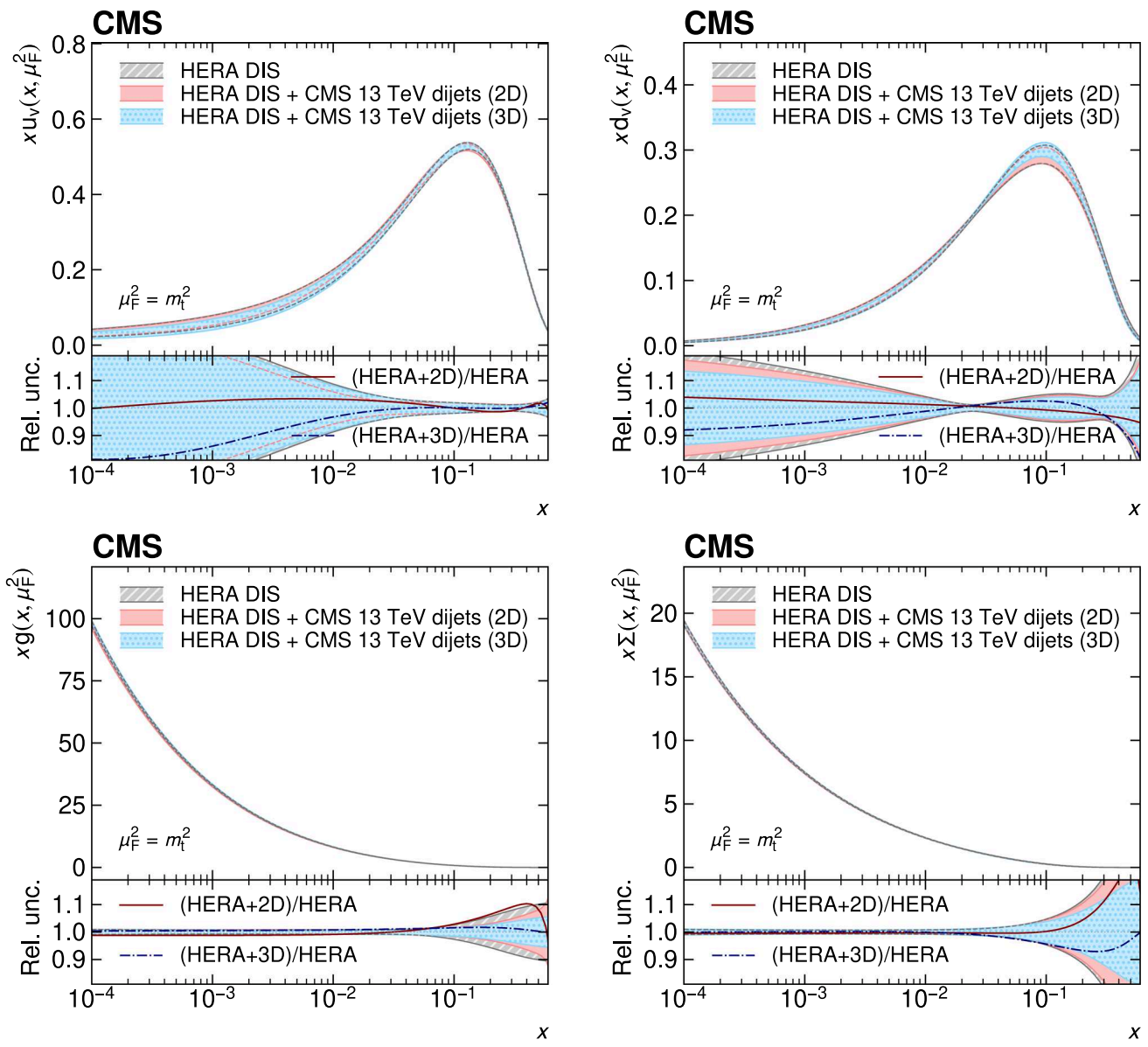

Fig. 12 Parton distributions obtained in a fit to HERA DIS data together with the CMS dijet data, compared to a fit to HERA DIS data alone. Shown are the PDFs of the up and down valence quarks (upper row), of the gluon (lower left), and of the total sea quarks (lower right) as a function of the fractional parton momentum x at a factorization scale equal to the top quark mass. The bands indicate the fit uncertainty and are shown in the lower panels as a relative uncertainty with respect to the corresponding central values. The lines in the lower panels show the ratios between the fitted central values

3D data are observed to constrain the gluon PDF to higher values of x compared to the 2D data.

For the PDF determinations presented above, the value of $\alpha_S(m_Z)$ is extracted from the data by including it in the fits as a free parameter, thus ensuring a consistent treatment of correlations between $\alpha_S(m_Z)$ and the PDF parameters, in particular those of the gluon distribution. The value of $\alpha_S(m_Z)$ obtained in the fit to the 2D dijet cross sections is

$$\begin{aligned} \alpha_S(m_Z) = 0.1179 \quad & \pm 0.0015\,(\text{fit}) \\ & \pm 0.0008\,(\text{scale}) \\ & \pm 0.0008\,(\text{model}) \\ & \pm 0.0001\,(\text{param.}) \\ = 0.1179 \quad & \pm 0.0019\,(\text{total}), \end{aligned} \tag{9}$$

where the central value (fit uncertainty) is obtained as the average (standard deviation) over the ensemble of MC replicas. The remaining uncertainties are determined analogously to the PDFs, and in particular the parametrization uncertainty contributes linearly to the total uncertainty while the remaining contributions are added in quadrature. For the 3D dijet measurement, the result obtained is

$$\begin{aligned} \alpha_S(m_Z) = 0.1181 \quad & \pm 0.0013\,(\text{fit}) \\ & \pm 0.0009\,(\text{scale}) \\ & \pm 0.0006\,(\text{model}) \\ & \pm 0.0002\,(\text{param.}) \\ = 0.1181 \quad & \pm 0.0022\,(\text{total}), \end{aligned} \tag{10}$$

which is in good agreement with the 2D result.

The values of $\alpha_S(m_Z)$ determined from the dijet measurements are in agreement with the value of 0.1166 ± 0.0017 obtained in Ref. [61], and with the world average value of 0.1179 ± 0.0009 [76].

Parton distributions obtained in previous analyses at $\sqrt{s}$ = 8 or 13 TeV of the inclusive jet [60,61,77] or the 3D dijet cross section [5] are not easily comparable directly because of significant differences in the fit setup, the PDF parametrizations, the model parameters, and particularly in the theoretical calculations at 8 TeV, which were only available at NLO. Taking the fit uncertainty in $\alpha_S(m_Z)$ obtained in a simultaneous fit with the PDFs as a figure of merit, the 13 TeV results are more precise, which is consistent with the increase in integrated luminosity.

11 Summary

The dijet production cross section is measured based on pp collision data recorded by the CMS detector in 2016 at $\sqrt{s} =$ 13 TeV, corresponding to an integrated luminosity of up to 36.3 fb^{-1}.

The measurements are performed double-differentially (2D) as a function of the dijet invariant mass $m_{1,2}$ in five regions of the maximal absolute rapidity $|y|_{\max}$ of the two jets with the largest transverse momenta, and triple-differentially (3D) as a function of either $m_{1,2}$ or the average transverse momentum $\langle p_T \rangle_{1,2}$ in 15 bins of the rapidity variables y^* and y_b. The latter two variables correspond to the rapidity separation of the two jets, and the total boost of the dijet system, respectively. All measurements are performed for jets clustered using the anti-k_T jet algorithm with distance parameters $R = 0.4$ and 0.8, and the cross sections are unfolded in all measurement dimensions simultaneously to correct for detector effects.

This is the first time that such a large set of multidifferential dijet measurements for two observables, $\langle p_T \rangle_{1,2}$ and $m_{1,2}$, and two jet distance parameters, $R = 0.4$ and 0.8, is made available for comparison to theory and use in fits of the parton distribution functions (PDFs) of the proton. Predictions at next-to-next-to-leading order (NNLO) in perturbative quantum chromodynamics, supplemented with electroweak and nonperturbative corrections are observed to describe the data better for $R = 0.8$.

Using the measurement of $m_{1,2}$ for $R = 0.8$, the PDFs of the proton are determined simultaneously in fits to the dijet measurements together with deep-inelastic scattering data from the HERA experiments following the approach described in earlier HERAPDF analyses [1,2,62]. The results obtained from the double- and triple-differential measurements are compatible within the estimated uncertainties. The inclusion of either of the dijet measurements leads to an improved determination of the PDFs compared to fits to HERA data alone. In particular, the uncertainty in the gluon distribution at fractional proton momenta $x > 0.1$ is reduced, with the 3D dijet data providing tighter constraints at higher values of x compared to the 2D data. The strong coupling constant at the Z boson mass is determined simultaneously with the PDFs, yielding consistent results between the 2D and 3D dijet measurements, with the former resulting in the slightly more precise value of $\alpha_S(m_Z) = 0.1179 \pm 0.0019$ at NNLO.

The impact of subleading-color contributions to the leading-color NNLO calculation used here is not yet known [41]. Apart from being useful as inputs to PDF fits or studies of jet size dependence, the present 2D and 3D measurements for two jet size parameters, $R = 0.4$ and 0.8, and for the two dijet observables $m_{1,2}$ and $\langle p_T \rangle_{1,2}$, provide an ideal testing ground for further investigations.

Acknowledgements We congratulate our colleagues in the CERN accelerator departments for the excellent performance of the LHC and thank the technical and administrative staffs at CERN and at other CMS institutes for their contributions to the success of the CMS effort. In addition, we gratefully acknowledge the computing centers and personnel of the Worldwide LHC Computing Grid and other centers for delivering so effectively the computing infrastructure essential to our analyses. Finally, we acknowledge the enduring support for the construction and operation of the LHC, the CMS detector, and the supporting computing infrastructure provided by the following funding agencies: SC (Armenia), BMBWF and FWF (Austria); FNRS and FWO (Belgium); CNPq, CAPES, FAPERJ, FAPERGS, and FAPESP (Brazil); MES and BNSF (Bulgaria); CERN; CAS, MoST, and NSFC (China); MINCIENCIAS (Colombia); MSES and CSF (Croatia); RIF (Cyprus); SENESCYT (Ecuador); MoER, ERC PUT and ERDF (Estonia); Academy of Finland, MEC, and HIP (Finland); CEA and CNRS/IN2P3 (France); SRNSF (Georgia); BMBF, DFG, and HGF (Germany); GSRI (Greece); NKFIH (Hungary); DAE and DST (India); IPM (Iran); SFI (Ireland); INFN (Italy); MSIP and NRF (Republic of Korea); MES (Latvia); LAS (Lithuania); MOE and UM (Malaysia); BUAP, CINVESTAV, CONACYT, LNS, SEP, and UASLP-FAI (Mexico); MOS (Montenegro); MBIE (New Zealand); PAEC (Pakistan); MES and NSC (Poland); FCT (Portugal); MESTD (Serbia); MCIN/AEI and PCTI (Spain); MOSTR (Sri Lanka); Swiss Funding Agencies (Switzerland); MST (Taipei);

MHESI and NSTDA (Thailand); TUBITAK and TENMAK (Turkey); NASU (Ukraine); STFC (United Kingdom); DOE and NSF (USA).
Individuals have received support from the Marie-Curie program and the European Research Council and Horizon 2020 Grant, contract Nos. 675440, 724704, 752730, 758316, 765710, 824093, and COST Action CA16108 (European Union); the Leventis Foundation; the Alfred P. Sloan Foundation; the Alexander von Humboldt Foundation; the Science Committee, project no. 22rl-037 (Armenia); the Belgian Federal Science Policy Office; the Fonds pour la Formation à la Recherche dans l'Industrie et dans l'Agriculture (FRIA-Belgium); the Agentschap voor Innovatie door Wetenschap en Technologie (IWT-Belgium); the F.R.S.-FNRS and FWO (Belgium) under the "Excellence of Science – EOS" – be.h project n. 30820817; the Beijing Municipal Science & Technology Commission, No. Z191100007219010 and Fundamental Research Funds for the Central Universities (China); the Ministry of Education, Youth and Sports (MEYS) of the Czech Republic; the Shota Rustaveli National Science Foundation, grant FR-22-985 (Georgia); the Deutsche Forschungsgemeinschaft (DFG), under Germany's Excellence Strategy – EXC 2121 "Quantum Universe" – 390833306, and under project number 400140256 - GRK2497; the Hellenic Foundation for Research and Innovation (HFRI), Project Number 2288 (Greece); the Hungarian Academy of Sciences, the New National Excellence Program - ÚNKP, the NKFIH research grants K 124845, K 124850, K 128713, K 128786, K 129058, K 131991, K 133046, K 138136, K 143460, K 143477, 2020-2.2.1-ED-2021-00181, and TKP2021-NKTA-64 (Hungary); the Council of Science and Industrial Research, India; ICSC – National Research Center for High Performance Computing, Big Data and Quantum Computing, funded by the EU NexGeneration program (Italy); the Latvian Council of Science; the Ministry of Education and Science, project no. 2022/WK/14, and the National Science Center, contracts Opus 2021/41/B/ST2/01369 and 2021/43/B/ST2/01552 (Poland); the Fundação para a Ciência e a Tecnologia, grant CEECIND/01334/2018 (Portugal); the National Priorities Research Program by Qatar National Research Fund; MCIN/AEI/10.13039/501100011033, ERDF "a way of making Europe", and the Programa Estatal de Fomento de la Investigación Científica y Técnica de Excelencia María de Maeztu, grant MDM-2017-0765 and Programa Severo Ochoa del Principado de Asturias (Spain); the Chulalongkorn Academic into Its 2nd Century Project Advancement Project, and the National Science, Research and Innovation Fund via the Program Management Unit for Human Resources & Institutional Development, Research and Innovation, grant B37G660013 (Thailand); the Kavli Foundation; the Nvidia Corporation; the SuperMicro Corporation; the Welch Foundation, contract C-1845; and the Weston Havens Foundation (USA).

Data Availability Statement Release and preservation of data used by the CMS Collaboration as the basis for publications is guided by the CMS data preservation, re-use and open access policy.

Code Availability Statement The CMS core software is publicly available on GitHub (https://github.com/cms-sw/cmssw).

Declarations

Conflict of interest The authors declare that they have no Conflict of interest.

Open Access This article is licensed under a Creative Commons Attribution 4.0 International License, which permits use, sharing, adaptation, distribution and reproduction in any medium or format, as long as you give appropriate credit to the original author(s) and the source, provide a link to the Creative Commons licence, and indicate if changes were made. The images or other third party material in this article are included in the article's Creative Commons licence, unless indicated otherwise in a credit line to the material. If material is not included in the article's Creative Commons licence and your intended use is not permitted by statutory regulation or exceeds the permitted use, you will need to obtain permission directly from the copyright holder. To view a copy of this licence, visit http://creativecommons.org/licenses/by/4.0/.

Funded by SCOAP[3].

Appendix A: Full-rapidity fit results

This section documents the results obtained for the fits described in Sect. 10 when all dijet rapidity regions are included. The partial χ^2 values indicating the goodness-of-fit in each rapidity region are given in Table 4, and Eqs. (11) and (12) show the values of $\alpha_S(m_Z)$ obtained in fits including the 2D and 3D dijet cross sections, respectively:

$$\begin{aligned} \alpha_S(m_Z)_{2D} = 0.1201 \quad & \pm 0.0012\,(\text{fit}) \\ & \pm 0.0008\,(\text{scale}) \\ & \pm 0.0008\,(\text{model}) \\ & \pm 0.0005\,(\text{param.}), \end{aligned} \tag{11}$$

$$\begin{aligned} \alpha_S(m_Z)_{3D} = 0.1201 \quad & \pm 0.0010\,(\text{fit}) \\ & \pm 0.0005\,(\text{scale}) \\ & \pm 0.0008\,(\text{model}) \\ & \pm 0.0006\,(\text{param.}). \end{aligned} \tag{12}$$

Table 4 Goodness-of-fit values for the fits to the HERA DIS data alone, and together with the CMS dijet measurements, including all rapidity regions. The table shows the partial χ^2 values divided by the number of data points for the HERA DIS datasets and each of the dijet rapidity regions. The total χ^2 value, divided by the number of degrees of freedom, is given at the bottom of the table

		Partial χ^2 / n_{data} HERA DIS + CMS 13 TeV dijets	
Data set		2D	3D
CMS dijet 2D			
$\lvert y\rvert_{\max} < 0.5$		24 / 22	
$0.5 < \lvert y\rvert_{\max} < 1$		14 / 22	
$1 < \lvert y\rvert_{\max} < 1.5$		22 / 23	
$1.5 < \lvert y\rvert_{\max} < 2$		15 / 12	
$2 < \lvert y\rvert_{\max} < 2.5$		30 / 12	
CMS dijet 3D			
$y_b < 0.5$,	$y^* < 0.5$		32 / 21
$y_b < 0.5$,	$0.5 < y^* < 1$		23 / 19
$0.5 < y_b < 1$,	$y^* < 0.5$		40 / 19
$y_b < 0.5$,	$1 < y^* < 1.5$		45 / 17
$0.5 < y_b < 1$,	$0.5 < y^* < 1$		18 / 17
$1 < y_b < 1.5$,	$y^* < 0.5$		44 / 17
$y_b < 0.5$,	$1.5 < y^* < 2$		15 / 7
$0.5 < y_b < 1$,	$1 < y^* < 1.5$		7 / 7
$1 < y_b < 1.5$,	$0.5 < y^* < 1$		9 / 7
$1.5 < y_b < 2$,	$y^* < 0.5$		20 / 6
$y_b < 0.5$,	$2 < y^* < 2.5$		19 / 6
$0.5 < y_b < 1$,	$1.5 < y^* < 2$		16 / 6
$1 < y_b < 1.5$,	$1 < y^* < 1.5$		6 / 6
$1.5 < y_b < 2$,	$0.5 < y^* < 1$		1 / 5
$2 < y_b < 2.5$,	$y^* < 0.5$		15 / 4
HERA1+2			
CC e^-p, $E_p = 920$ GeV		50 / 42	48 / 42
CC e^+p, $E_p = 920$ GeV		37 / 39	41 / 39
NC e^-p, $E_p = 920$ GeV		222 / 159	227 / 159
NC e^+p, $E_p = 460$ GeV		197 / 177	201 / 177
NC e^+p, $E_p = 575$ GeV		186 / 221	187 / 221
NC e^+p, $E_p = 820$ GeV		55 / 61	55 / 61
NC e^+p, $E_p = 920$ GeV		368 / 317	365 / 317
Total χ^2/n_{dof}		1283 / 1094	1557 / 1167

Appendix B: Additional figures

See Figs. 13, 14, 15, 16, 17, 18, 19, 20, 21, 22, 23, 24, 25, 26, 27 and 28.

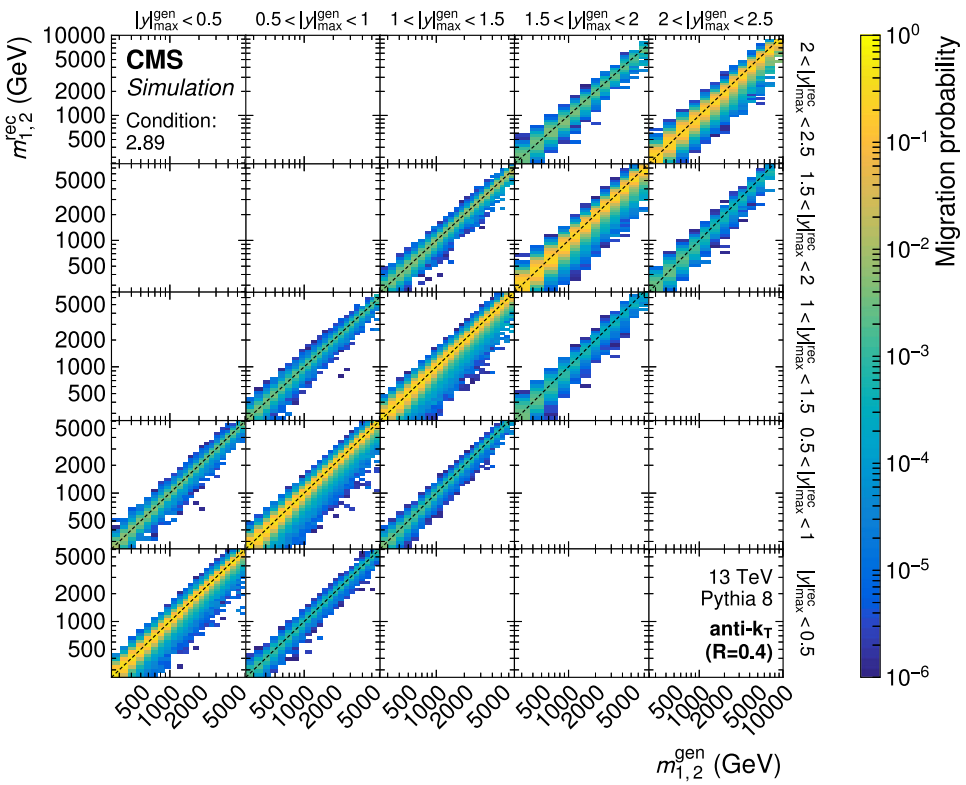

Fig. 13 Response matrix for the 2D measurements as a function of $m_1, 2$ for jets with $R = 0.4$. The details correspond to those of Fig. 2

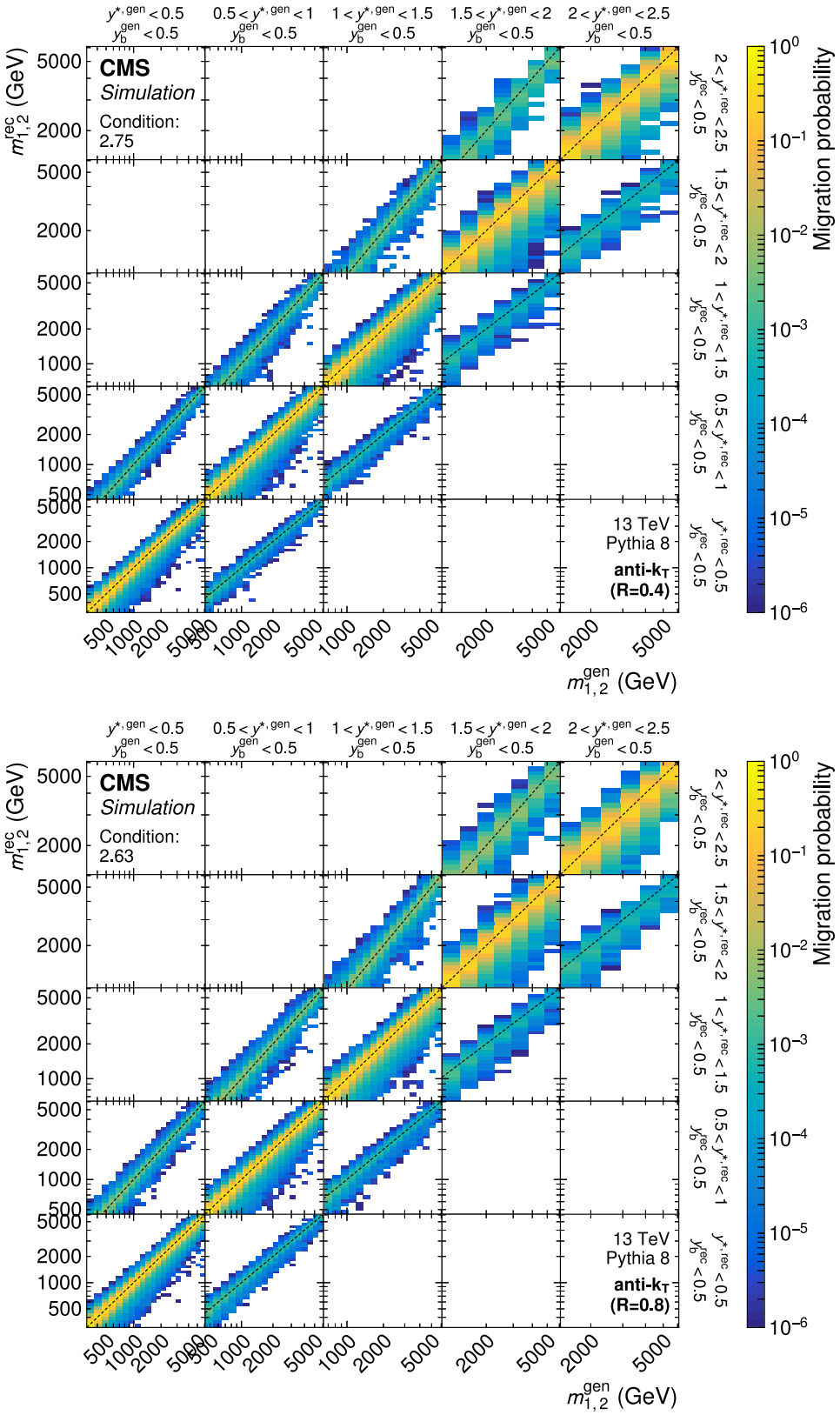

Fig. 14 Partial response matrices for the 3D measurements as a function of $m_{1,2}$ using jets with $R = 0.4$ (upper) and 0.8 (lower), shown here for the five rapidity regions with $y_b < 0.5$. The details correspond to those of Fig. 2

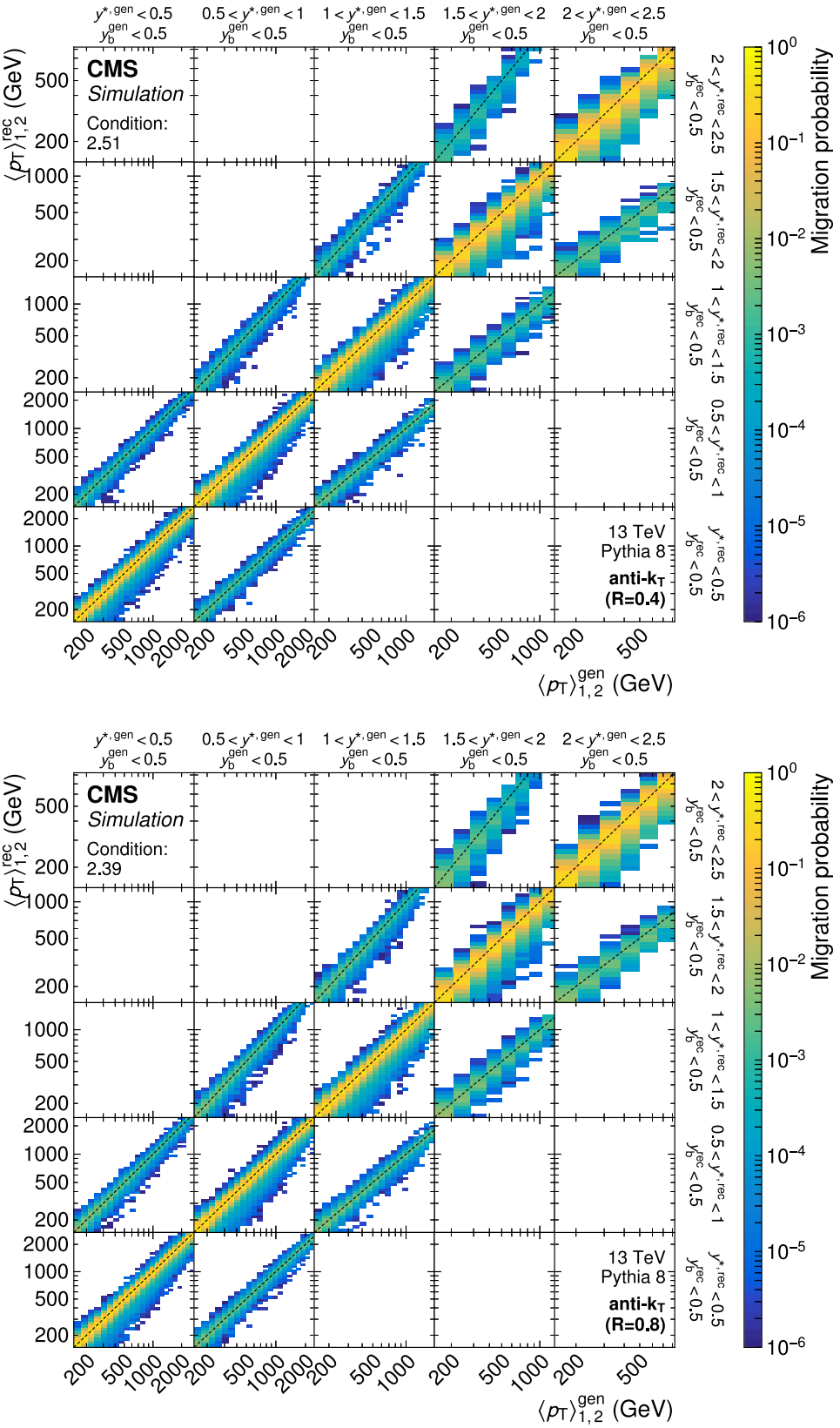

Fig. 15 Partial response matrices for the 3D measurements as a function of $\langle p_T \rangle_{1,2}$ using jets with $R = 0.4$ (upper) and 0.8 (lower), shown here for the five rapidity regions with $y_b < 0.5$. The details correspond to those of Fig. 2

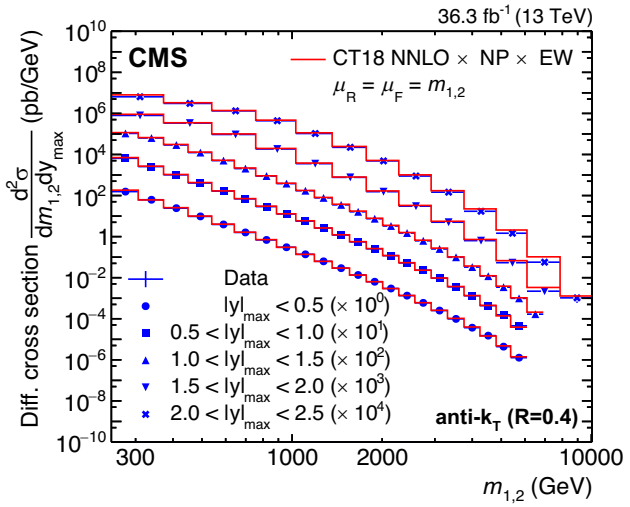

Fig. 16 Overview of the 2D dijet cross section as a function of $m_{1,2}$ in all 5 $|y|_{max}$ regions, using jets with $R = 0.4$. The details correspond to those of Fig. 8

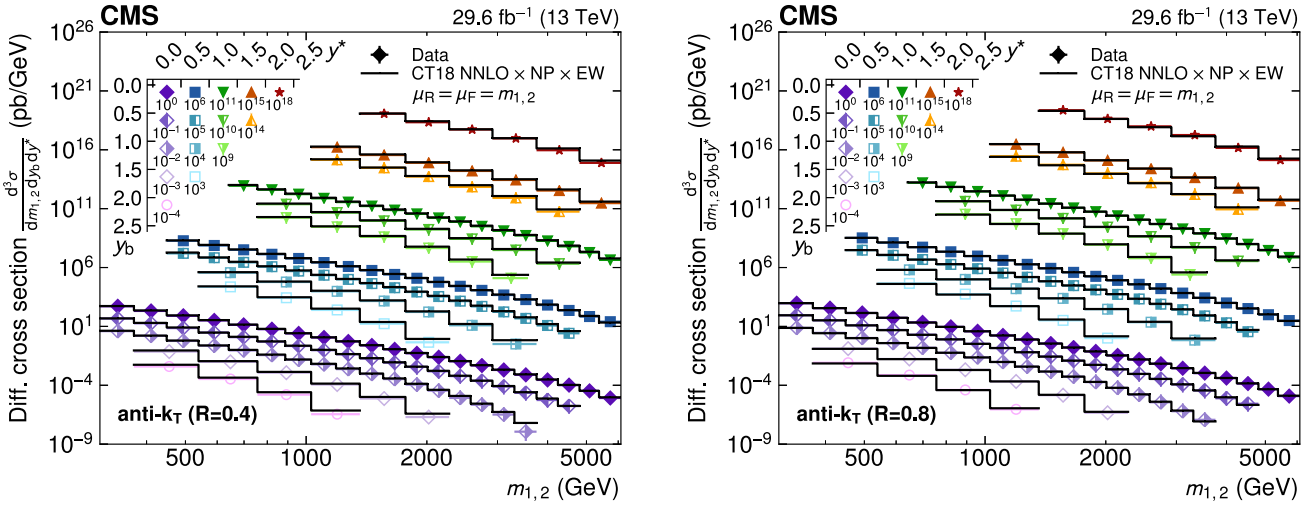

Fig. 17 Overview of the 3D dijet cross section as a function of $m_{1,2}$ in all 15 (y^*, y_b) regions, using jets with $R = 0.4$ (left) and 0.8 (right). The details correspond to those of Fig. 8

Fig. 18 Overview of the 3D dijet cross section as a function of $\langle p_T \rangle_{1,2}$ in all 15 (y^*, y_b) regions, using jets with $R = 0.8$. The details correspond to those of Fig. 8

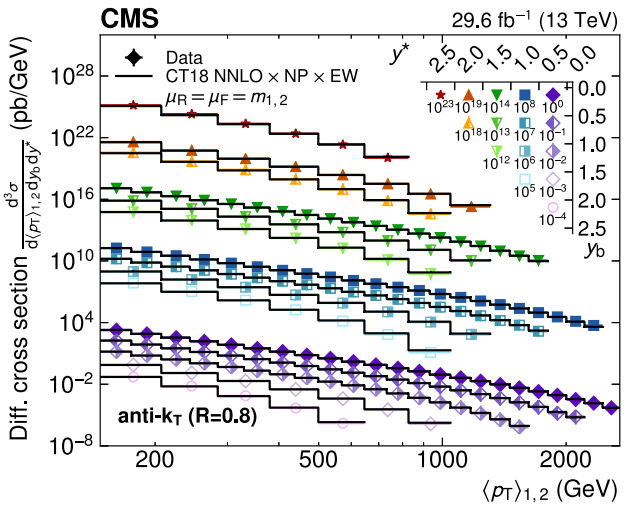

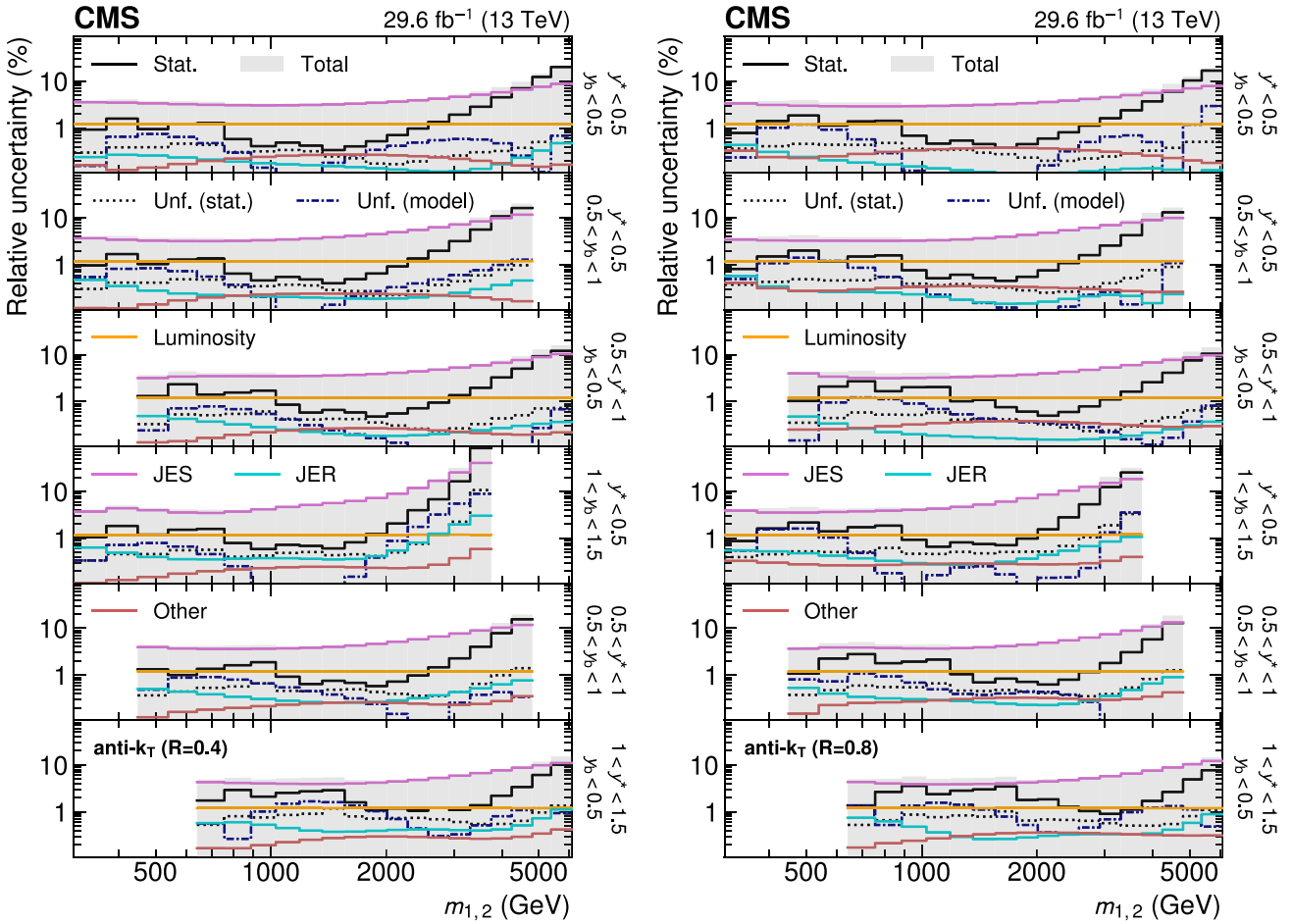

Fig. 19 Breakdown of the experimental uncertainty for the 3D measurements as a function of $m_{1,2}$ using jets with $R = 0.4$ (left) and 0.8 (right), in six out of 15 (y^*, y_b) bins. The details correspond to those of Fig. 4

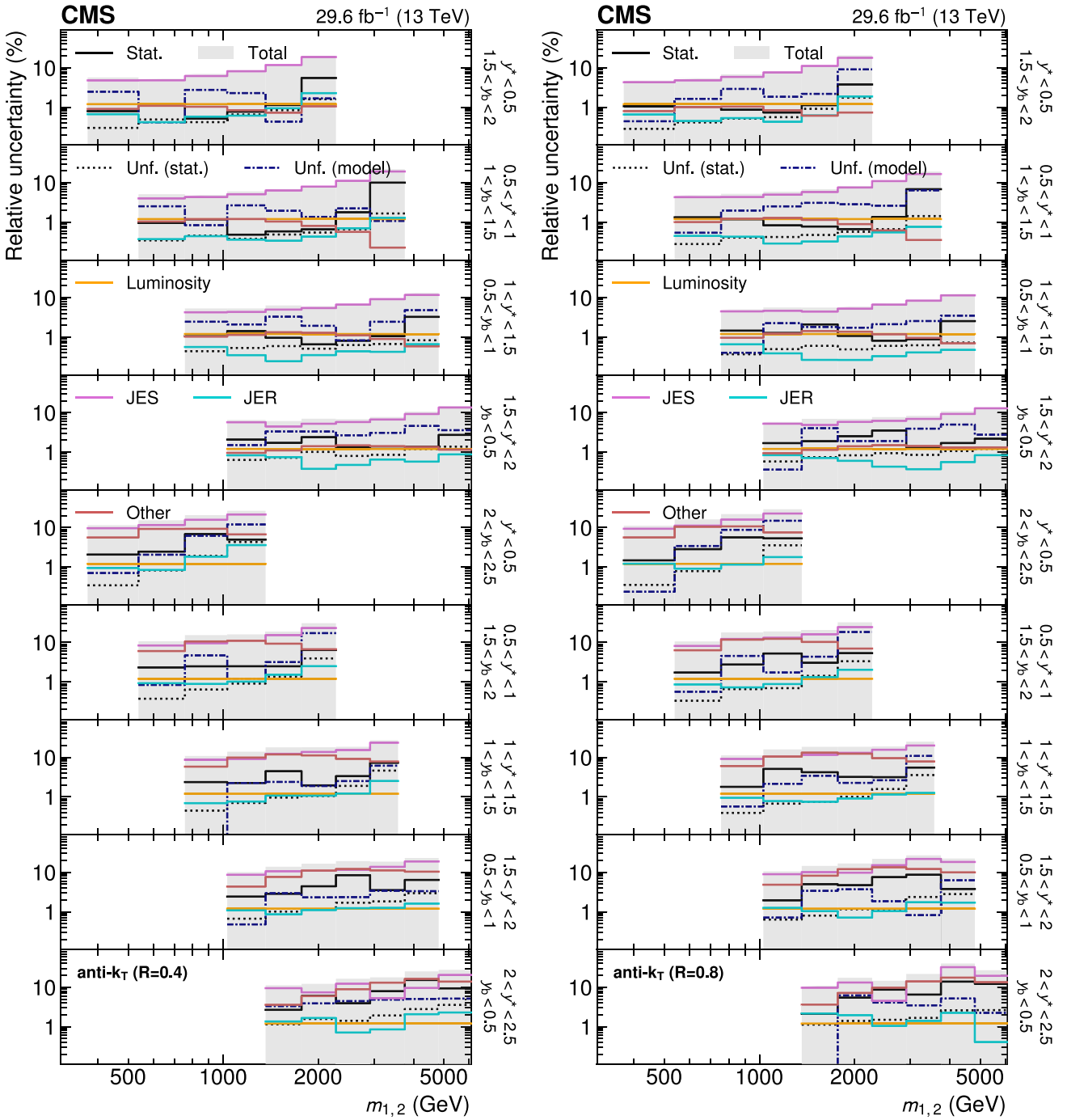

Fig. 20 (*continuation of Fig.* 19) Breakdown of the experimental uncertainty for the 3D measurements as a function of $m_{1,2}$ using jets with $R = 0.4$ (left) and 0.8 (right), in the remaining nine out of 15 (y^*, y_b) bins. The details correspond to those of Fig. 4

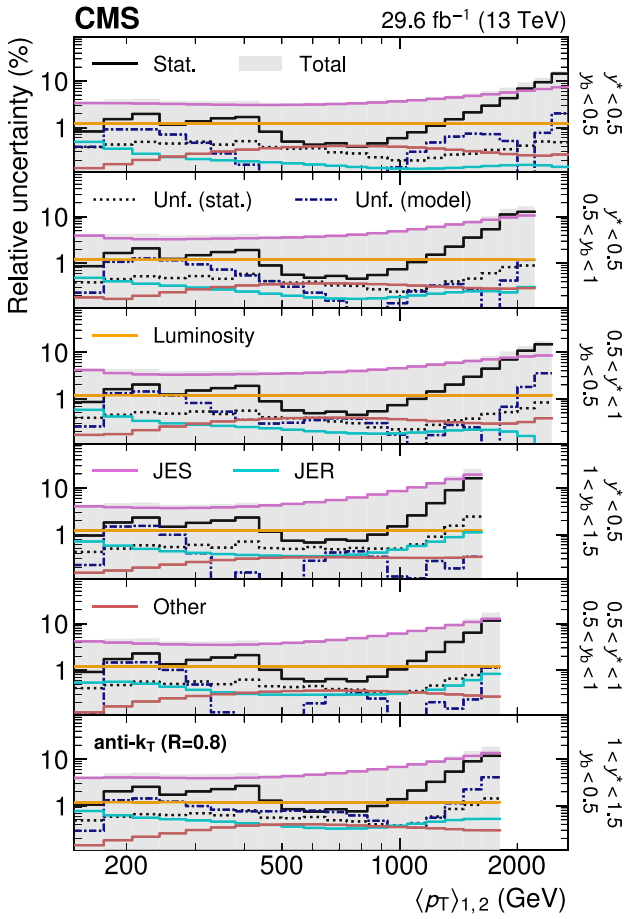

Fig. 21 Breakdown of the experimental uncertainty for the 3D measurements as a function of $\langle p_T \rangle_{1,2}$ using jets with $R = 0.8$, in six out of 15 (y^*, y_b) bins. The details correspond to those of Fig. 4

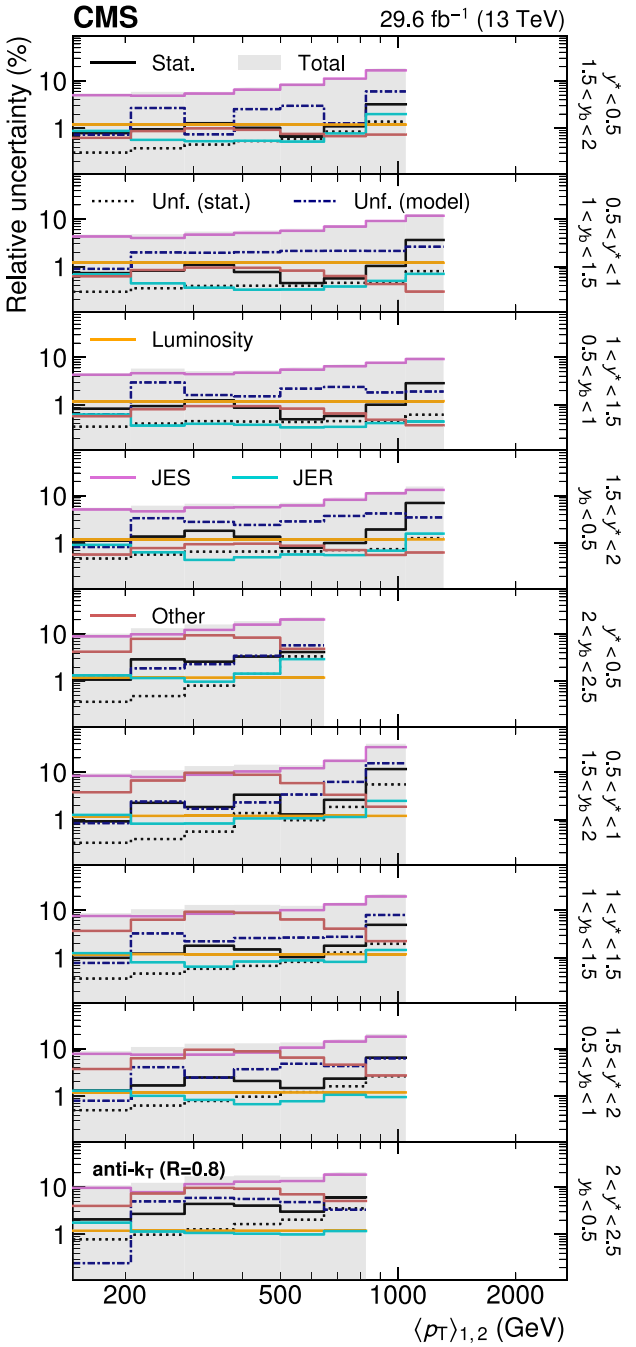

Fig. 22 (*continuation of Fig.* 21) Breakdown of the experimental uncertainty for the 3D measurements as a function of $\langle p_T \rangle_{1,2}$ using jets with $R = 0.8$, in the remaining nine out of 15 (y^*, y_b) bins. The details correspond to those of Fig. 4

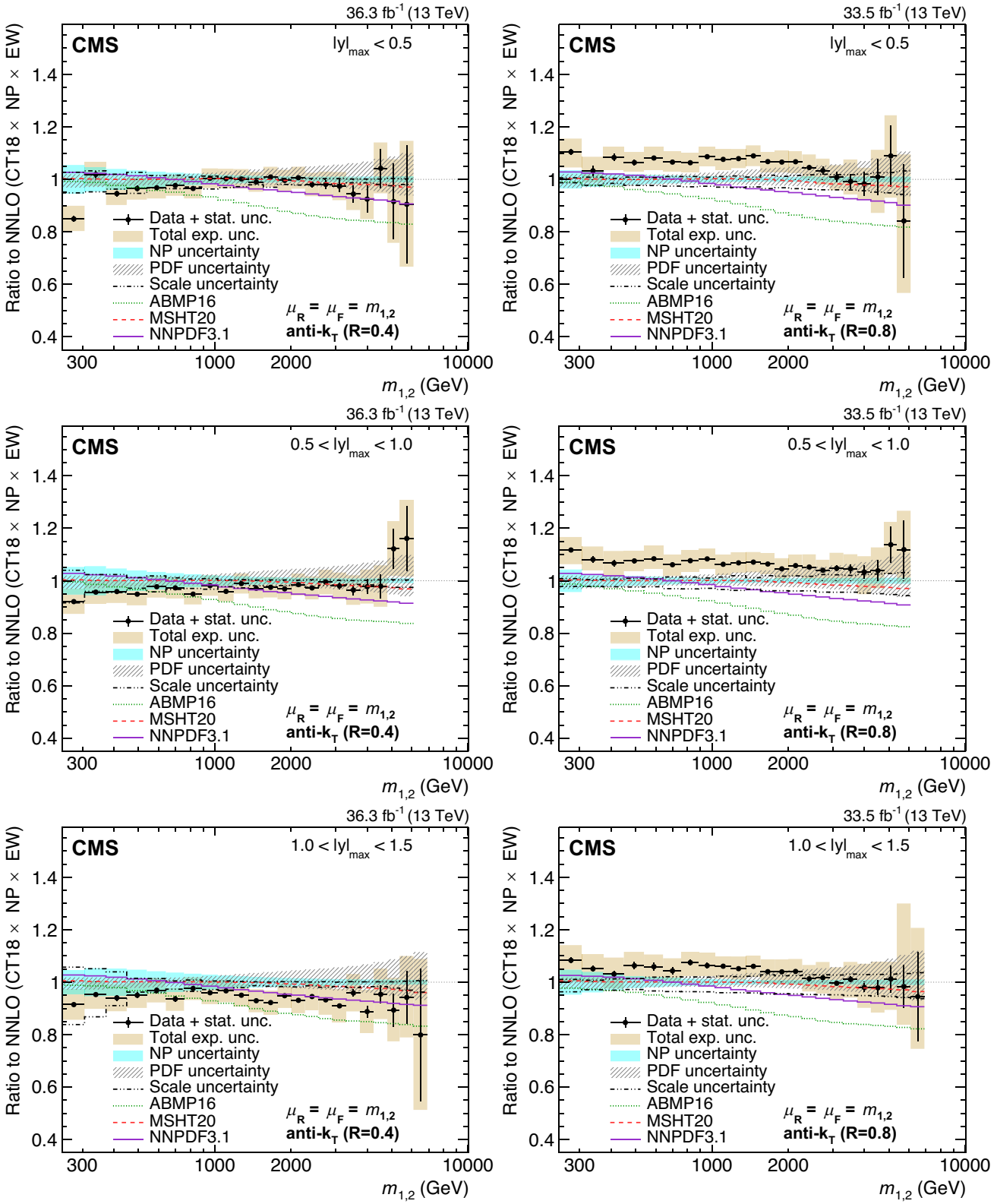

Fig. 23 Comparison of the 2D dijet cross section for jets with $R = 0.4$ (left) and 0.8 (right) as a function of $m_{1,2}$ to fixed-order theoretical calculations at NNLO, shown here for three inner $|y|_{\max}$ regions. The details correspond to those of Fig. 9

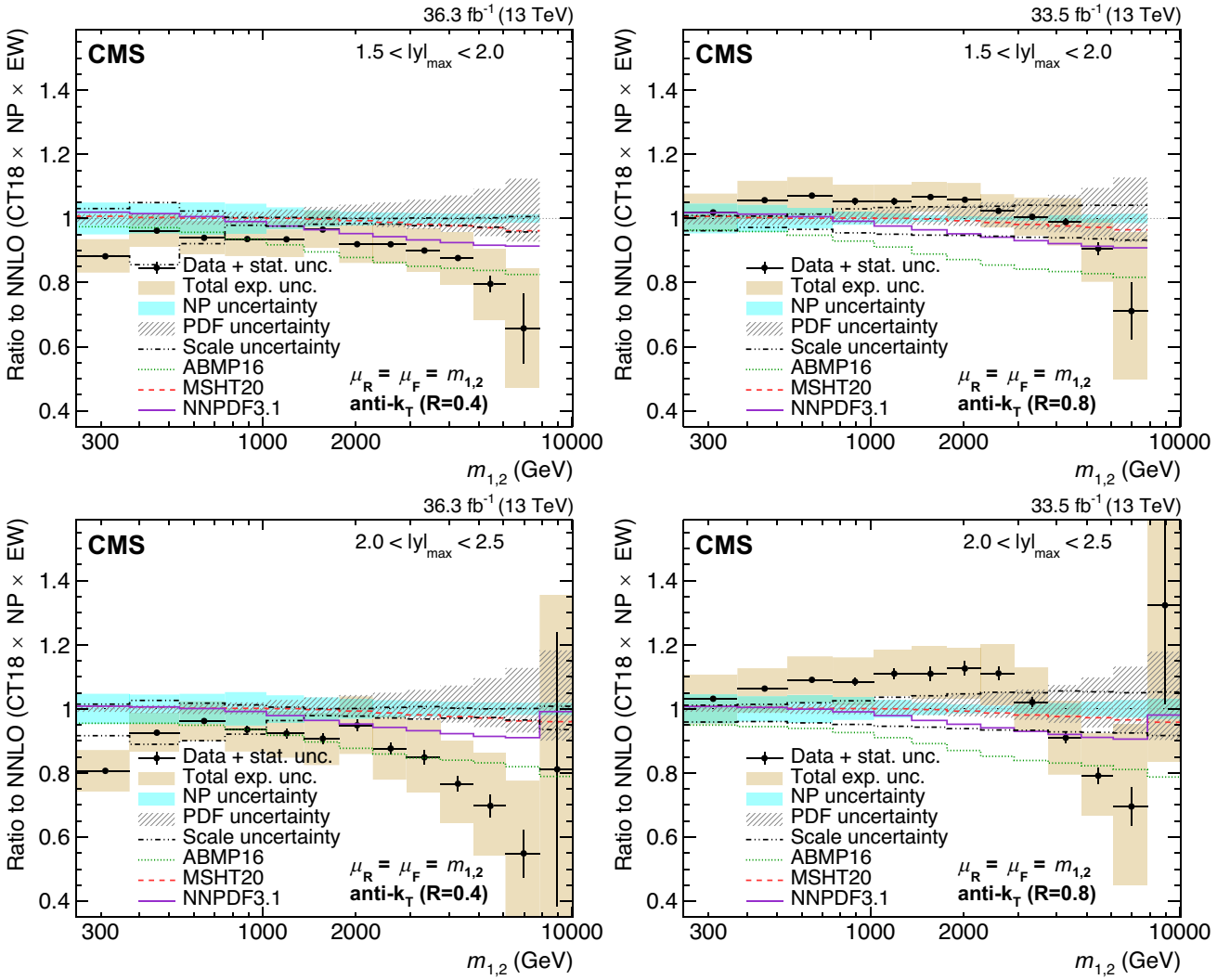

Fig. 24 (*continuation of Fig.* 23) Comparison of the 2D dijet cross section for jets with $R = 0.4$ (left) and 0.8 (right) as a function of $m_{1,2}$ to fixed-order theoretical calculations at NNLO, shown here for two outermost $|y|_{\max}$ regions. The details correspond to those of Fig. 9

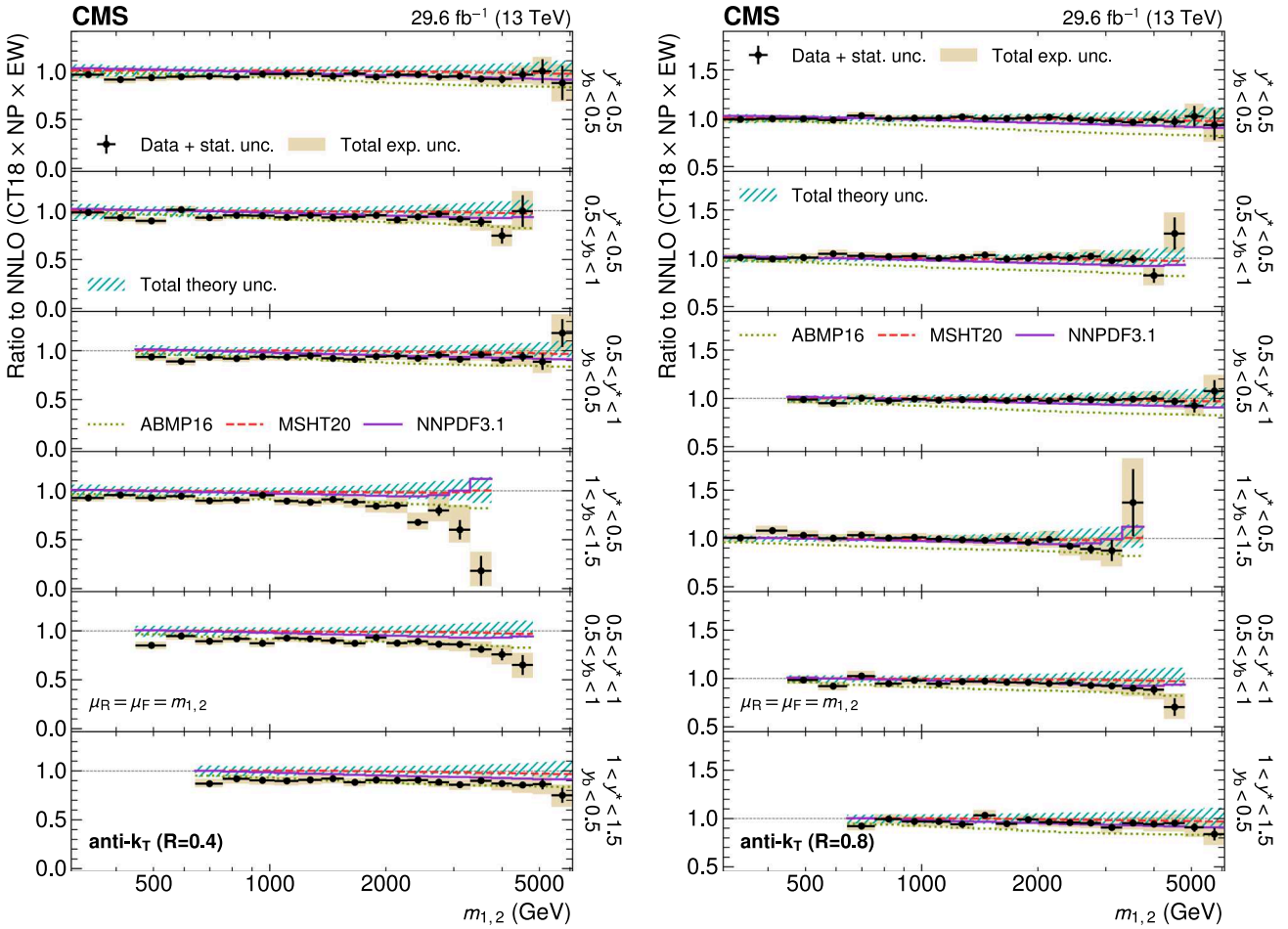

Fig. 25 Comparison of the 3D dijet cross section as a function of $m_{1,2}$ to fixed-order theoretical calculations at NNLO, using jets with $R = 0.4$ (left) and 0.8 (right), in six out of the total 15 (y^*, y_b) bins. The details correspond to those of Fig. 10

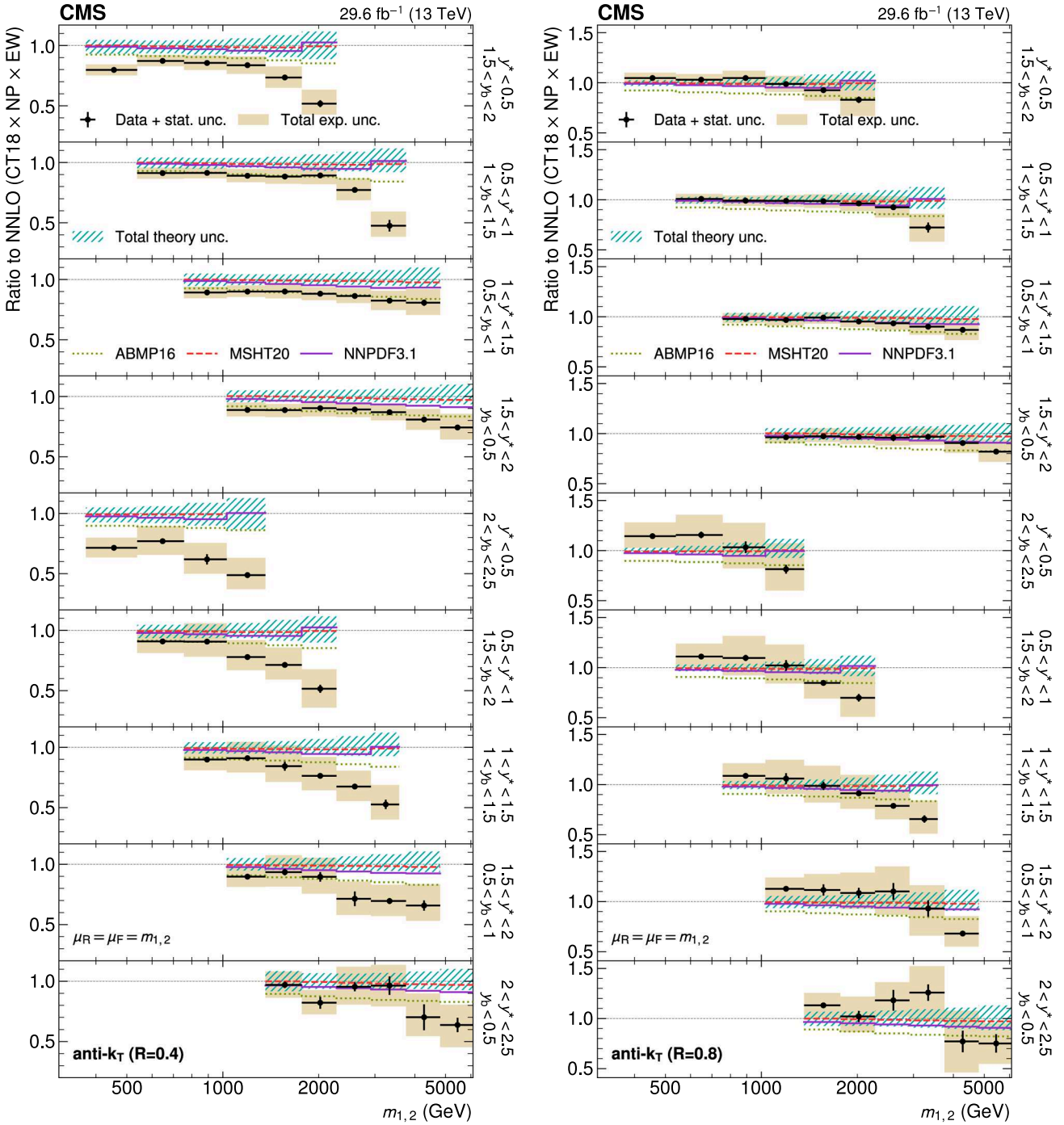

Fig. 26 (*continuation of Fig.* 25) Comparison of the 3D dijet cross section as a function of $m_{1,2}$ to fixed-order theoretical calculations at NNLO, using jets with $R = 0.4$ (left) and 0.8 (right), in the remaining nine out of 15 (y^*, y_b) bins. The details correspond to those of Fig. 10

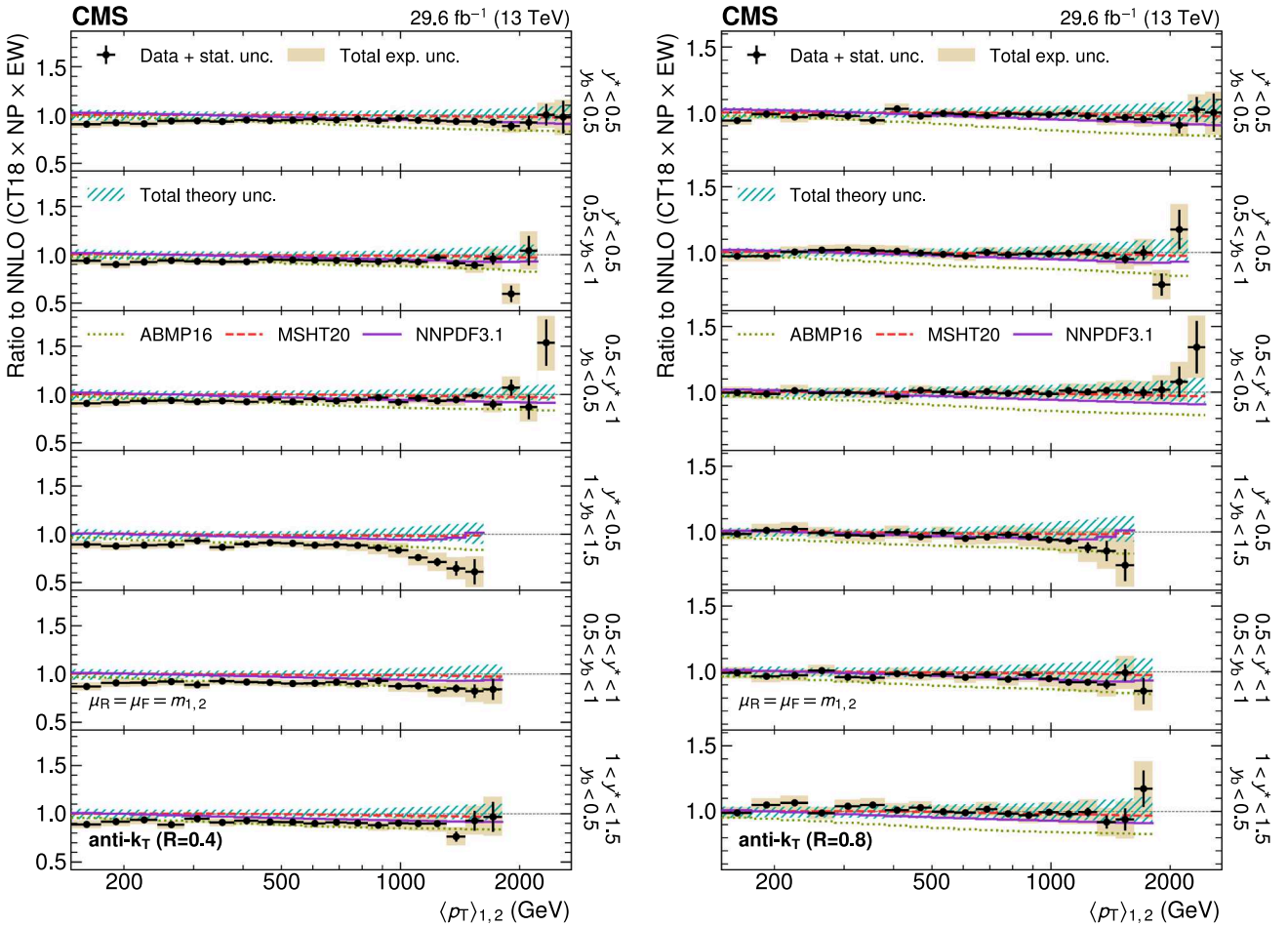

Fig. 27 Comparison of the 3D dijet cross section as a function of $\langle p_T \rangle_{1,2}$ to fixed-order theoretical calculations at NNLO, using jets with $R = 0.4$ (left) and 0.8 (right), in six out of the total 15 (y^*, y_b) bins. The details correspond to those of Fig. 10

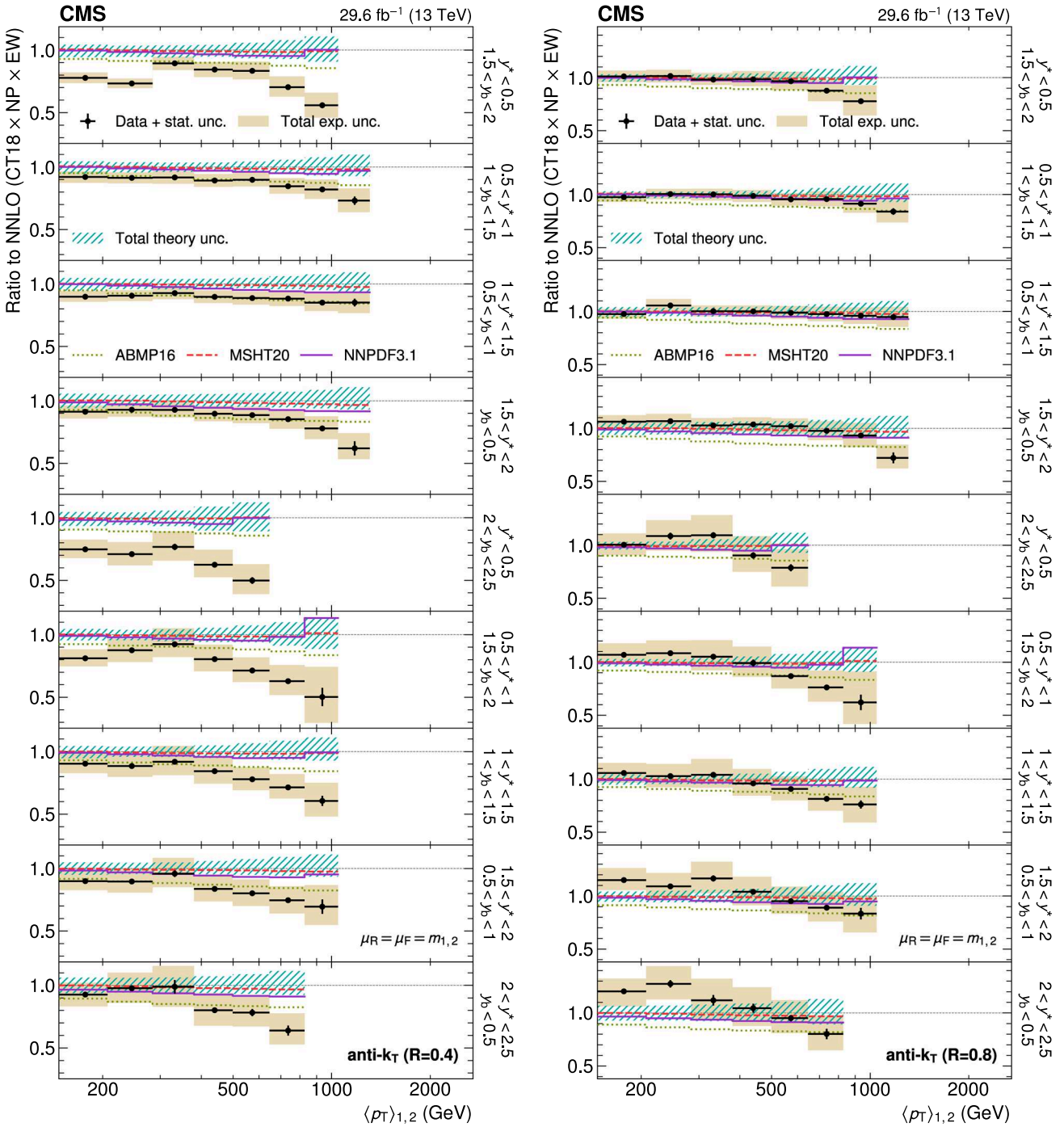

Fig. 28 (*continuation of Fig.* 27) Comparison of the 3D dijet cross section as a function of $\langle p_T \rangle_{1,2}$ to fixed-order theoretical calculations at NNLO, using jets with $R = 0.4$ (left) and 0.8 (right), in the remaining nine out of 15 (y^*, y_b) bins. The details correspond to those of Fig. 10

References

1. H1 and ZEUS Collaborations, Combined measurement and QCD analysis of the inclusive $e^{\pm}p$ scattering cross sections at HERA. JHEP **01**, 109 (2010). https://doi.org/10.1007/JHEP01(2010)109. arXiv:0911.0884
2. H1 and ZEUS Collaborations, Combination of measurements of inclusive deep inelastic $e^{\pm}p$ scattering cross sections and QCD analysis of HERA data. Eur. Phys. J. C **75**, 580 (2015). https://doi.org/10.1140/epjc/s10052-015-3710-4. arXiv:1506.06042
3. J. Currie et al., Precise predictions for dijet production at the LHC. Phys. Rev. Lett. **119**, 152001 (2017). https://doi.org/10.1103/PhysRevLett.119.152001. arXiv:1705.10271
4. A. Gehrmann-De Ridder et al., Triple differential dijet cross section at the LHC. Phys. Rev. Lett. **123**, 102001 (2019). https://doi.org/10.1103/PhysRevLett.123.102001. arXiv:1905.09047
5. CMS Collaboration, Measurement of the triple-differential dijet cross section in proton-proton collisions at $\sqrt{s} = 8$ TeV and constraints on parton distribution functions. Eur. Phys. J. C **77**, 746 (2017). https://doi.org/10.1140/epjc/s10052-017-5286-7. arXiv:1705.02628
6. M. Cacciari, G.P. Salam, G. Soyez, The anti-k_T jet clustering algorithm. JHEP **04**, 063 (2008). https://doi.org/10.1088/1126-6708/2008/04/063. arXiv:0802.1189
7. M. Cacciari, G.P. Salam, G. Soyez, FastJet user manual. Eur. Phys. J. C **72**, 1896 (2012). https://doi.org/10.1140/epjc/s10052-012-1896-2. arXiv:1111.6097
8. ATLAS Collaboration, Measurement of inclusive jet and dijet cross sections in proton–proton collisions at 7 TeV centre-of-mass energy with the ATLAS detector. Eur. Phys. J. C **71**, 1512 (2011). https://doi.org/10.1140/epjc/s10052-010-1512-2. arXiv:1009.5908
9. CMS Collaboration, Measurement of the differential dijet production cross section in proton–proton collisions at $\sqrt{s} = 7$ TeV. Phys. Lett. B **700**, 187 (2011). https://doi.org/10.1016/j.physletb.2011.05.027. arXiv:1104.1693
10. CMS Collaboration, Measurements of differential jet cross sections in proton-proton collisions at $\sqrt{s} = 7$ TeV with the CMS detector. Phys. Rev. D **87**, 112002 (2013). https://doi.org/10.1103/PhysRevD.87.119902. arXiv:1212.6660. (Erratum: https://doi.org/10.1103/PhysRevD.87.112002)
11. ATLAS Collaboration, Measurement of dijet cross sections in pp collisions at 7 TeV centre-of-mass energy using the ATLAS detector. JHEP **05**, 059 (2014). https://doi.org/10.1007/JHEP05(2014)059. arXiv:1312.3524
12. ATLAS Collaboration, Measurement of inclusive jet and dijet cross-sections in proton-proton collisions at $\sqrt{s} = 13$ TeV with the ATLAS detector. JHEP **05**, 195 (2018). https://doi.org/10.1007/JHEP05(2018)195. arXiv:1711.02692
13. HEPData record for this analysis (2023). https://doi.org/10.17182/hepdata.146075
14. CMS Collaboration, The CMS trigger system. JINST **12**, P01020 (2017). https://doi.org/10.1088/1748-0221/12/01/P01020. arXiv:1609.02366
15. CMS Collaboration, Performance of the CMS Level-1 trigger in proton-proton collisions at $\sqrt{s} = 13$ TeV. JINST **15**, P10017 (2020). https://doi.org/10.1088/1748-0221/15/10/P10017. arXiv:2006.10165
16. CMS Collaboration, The CMS experiment at the CERN LHC. JINST **3**, S08004 (2008). https://doi.org/10.1088/1748-0221/3/08/S08004
17. T. Sjöstrand et al., An introduction to PYTHIA 8.2. Comput. Phys. Commun. **191**, 159 (2015). https://doi.org/10.1016/j.cpc.2015.01.024. arXiv:1410.3012
18. CMS Collaboration, Event generator tunes obtained from underlying event and multiparton scattering measurements. Eur. Phys. J. C **76**, 155 (2016). https://doi.org/10.1140/epjc/s10052-016-3988-x. arXiv:1512.00815
19. J. Alwall et al., The automated computation of tree-level and next-to-leading order differential cross sections, and their matching to parton shower simulations. JHEP **07**, 079 (2014). https://doi.org/10.1007/JHEP07(2014)079. arXiv:1405.0301
20. GEANT4 Collaboration, Geant4—a simulation toolkit. Nucl. Instrum. Methods A **506**, 250 (2003). https://doi.org/10.1016/S0168-9002(03)01368-8
21. CMS Collaboration, Measurement of the inelastic proton-proton cross section at $\sqrt{s} = 13$ TeV. JHEP **07**, 161 (2018). https://doi.org/10.1007/JHEP07(2018)161. arXiv:1802.02613
22. CMS Collaboration, Pileup mitigation at CMS in 13 TeV data. JINST **15**, P09018 (2020). https://doi.org/10.1088/1748-0221/15/09/P09018. arXiv:2003.00503
23. CMS Collaboration, Particle-flow reconstruction and global event description with the CMS detector. JINST **12**, P10003 (2017). https://doi.org/10.1088/1748-0221/12/10/P10003. arXiv:1706.04965
24. CMS Collaboration, "Technical proposal for the Phase-II upgrade of the Compact Muon Solenoid", CMS Technical Proposal CERN-LHCC-2015-010, CMS-TDR-15-02 (2015). http://cds.cern.ch/record/2020886
25. CMS Collaboration, "Study of pileup removal algorithms for jets", CMS Physics Analysis Summary CMS-PAS-JME-14-001 (2014). http://cds.cern.ch/record/1751454
26. CMS Collaboration, Jet energy scale and resolution in the CMS experiment in pp collisions at 8 TeV. JINST **12**, P02014 (2017). https://doi.org/10.1088/1748-0221/12/02/P02014. arXiv:1607.03663
27. CMS Collaboration, "Jet algorithms performance in 13 TeV data", CMS Physics Analysis Summary CMS-PAS-JME-16-003 (2017). http://cds.cern.ch/record/2256875
28. CMS Collaboration, Performance of missing transverse momentum reconstruction in proton-proton collisions at $\sqrt{s} = 13$ TeV using the CMS detector. JINST **14**, P07004 (2019). https://doi.org/10.1088/1748-0221/14/07/P07004. arXiv:1903.06078
29. S. Schmitt, TUnfold: an algorithm for correcting migration effects in high energy physics. JINST **7**, T10003 (2012). https://doi.org/10.1088/1748-0221/7/10/T10003. arXiv:1205.6201
30. CMS Collaboration, "Jet energy scale and resolution performance with 13 TeV data collected by CMS in 2016–2018", CMS Detector Performance Note CMS-DP-2020-019 (2020). https://cds.cern.ch/record/2715872
31. CMS Collaboration, Precision luminosity measurement in proton-proton collisions at $\sqrt{s} = 13$ TeV in 2015 and 2016 at CMS. Eur. Phys. J. C **81**, 800 (2021). https://doi.org/10.1140/epjc/s10052-021-09538-2. arXiv:2104.01927
32. T. Gehrmann et al., "Jet cross sections and transverse momentume distributions with NNLOJET", in *Proceedings of 13th International Symposium on Radiative Corrections (Applications of Quantum Field Theory to Phenomenology)—PoS(RADCOR2017)*, vol. 290 (2018), p. 074. arXiv:1801.06415. https://doi.org/10.22323/1.290.0074
33. T. Kluge, K. Rabbertz, M. Wobisch, "fastNLO: Fast pQCD calculations for PDF fits", in *Proc. 14th Intern. Workshop on Deep-Inelastic Scattering (DIS 2006)* (Tsukuba, Japan, 2006), p. 483. https://doi.org/10.1142/9789812706706_0110. arXiv:hep-ph/0609285
34. D. Britzger, K. Rabbertz, F. Stober, M. Wobisch, "New features in version 2 of the fastNLO project", in *Proc. 20th Intern. Workshop on Deep-Inelastic Scattering and Related Subjects*, p. 217. (2012). arXiv:1208.3641. https://doi.org/10.3204/DESY-PROC-2012-02/165
35. D. Britzger et al., Calculations for deep inelastic scattering using fast interpolation grid techniques at NNLO in QCD and the extrac-

tion of α_s from HERA data. Eur. Phys. J. C **79**, 845 (2019). https://doi.org/10.1140/epjc/s10052-019-7351-x. arXiv:1906.05303
36. D. Britzger et al., NNLO interpolation grids for jet production at the LHC. Eur. Phys. J. C **82**, 930 (2022). https://doi.org/10.1140/epjc/s10052-022-10880-2. arXiv:2207.13735
37. M. Cacciari et al., The $t\bar{t}$ cross-section at 1.8 TeV and 1.96 TeV: a study of the systematics due to parton densities and scale dependence. JHEP **04**, 068 (2004). https://doi.org/10.1088/1126-6708/2004/04/068. arXiv:hep-ph/0303085
38. S. Catani, D. de Florian, M. Grazzini, P. Nason, Soft-gluon resummation for Higgs boson production at hadron colliders. JHEP **07**, 028 (2003). https://doi.org/10.1088/1126-6708/2003/07/028. arXiv:hep-ph/0306211
39. A. Banfi, G.P. Salam, G. Zanderighi, Phenomenology of event shapes at hadron colliders. JHEP **06**, 038 (2010). https://doi.org/10.1007/JHEP06(2010)038. arXiv:1001.4082
40. J. Currie, E.W.N. Glover, J. Pires, Next-to-next-to leading order QCD predictions for single jet inclusive production at the LHC. Phys. Rev. Lett. **118**, 072002 (2017). https://doi.org/10.1103/PhysRevLett.118.072002. arXiv:1611.01460
41. X. Chen et al., NNLO QCD corrections in full colour for jet production observables at the LHC. JHEP **09**, 025 (2022). https://doi.org/10.1007/JHEP09(2022)025. arXiv:2204.10173
42. CMS Collaboration, Measurement of the double-differential inclusive jet cross section in proton-proton collisions at $\sqrt{s} = 13$ TeV. Eur. Phys. J. C **76**, 451 (2016). https://doi.org/10.1140/epjc/s10052-016-4286-3. arXiv:1605.04436
43. CMS Collaboration, Investigations of the impact of the parton shower tuning in PYTHIA 8 in the modelling of $t\bar{t}$ at $\sqrt{s} = 8$ and 13 TeV. CMS Physics Analysis Summary CMS-PAS-TOP-16-021, (2016). http://cds.cern.ch/record/2235192
44. M. Bähr et al., herwig++ physics and manual. Eur. Phys. J. C **58**, 639 (2008). https://doi.org/10.1140/epjc/s10052-008-0798-9. arXiv:0803.0883
45. M.H. Seymour, A. Siódmok, Constraining MPI models using σ_{eff} and recent Tevatron and LHC underlying event data. JHEP **10**, 113 (2013). https://doi.org/10.1007/JHEP10(2013)113. arXiv:1307.5015
46. P. Nason, A new method for combining NLO QCD with shower Monte Carlo algorithms. JHEP **11**, 040 (2004). https://doi.org/10.1088/1126-6708/2004/11/040. arXiv:hep-ph/0409146
47. S. Frixione, P. Nason, C. Oleari, Matching NLO QCD computations with parton shower simulations: the POWHEG method. JHEP **11**, 070 (2007). https://doi.org/10.1088/1126-6708/2007/11/070. arXiv:0709.2092
48. S. Alioli, P. Nason, C. Oleari, E. Re, A general framework for implementing NLO calculations in shower Monte Carlo programs: the POWHEG BOX. JHEP **06**, 043 (2010). https://doi.org/10.1007/JHEP06(2010)043. arXiv:1002.2581
49. S. Alioli et al., Jet pair production in POWHEG. JHEP **04**, 081 (2011). https://doi.org/10.1007/JHEP04(2011)081. arXiv:1012.3380
50. J. Bellm et al., herwig 7.0/ herwig++ 3.0 release note. Eur. Phys. J. C **76**, 196 (2016). https://doi.org/10.1140/epjc/s10052-016-4018-8. arXiv:1512.01178
51. CMS Collaboration, Development and validation of herwig 7 tunes from CMS underlying-event measurements. Eur. Phys. J. C **81**, 312 (2021). https://doi.org/10.1140/epjc/s10052-021-08949-5. arXiv:2011.03422
52. S. Dittmaier, A. Huss, C. Speckner, Weak radiative corrections to dijet production at hadron colliders. JHEP **11**, 095 (2012). https://doi.org/10.1007/JHEP11(2012)095. arXiv:1210.0438
53. A. Buckley et al., LHAPDF6: parton density access in the LHC precision era. Eur. Phys. J. C **75**, 132 (2015). https://doi.org/10.1140/epjc/s10052-015-3318-8. arXiv:1412.7420
54. S. Alekhin, J. Blümlein, S. Moch, R. Plačakytė, Parton distribution functions, α_s, and heavy-quark masses for LHC Run II. Phys. Rev. D **96**, 014011 (2017). https://doi.org/10.1103/PhysRevD.96.014011. arXiv:1701.05838
55. T.-J. Hou et al., New CTEQ global analysis of quantum chromodynamics with high-precision data from the LHC. Phys. Rev. D **103**, 014013 (2021). https://doi.org/10.1103/PhysRevD.103.014013. arXiv:1912.10053
56. S. Bailey et al., Parton distributions from LHC, HERA, Tevatron and fixed target data: MSHT20 PDFs. Eur. Phys. J. C **81**, 341 (2021). https://doi.org/10.1140/epjc/s10052-021-09057-0. arXiv:2012.04684
57. NNPDF Collaboration, Parton distributions from high-precision collider data. Eur. Phys. J. C **77**, 663 (2017). https://doi.org/10.1140/epjc/s10052-017-5199-5. arXiv:1706.00428
58. CMS Collaboration, Measurement of the ratio of inclusive jet cross sections using the anti-k_T algorithm with radius parameters $R = 0.5$ and 0.7 in pp collisions at $\sqrt{s} = 7$ TeV. Phys. Rev. D **90**, 072006 (2014). https://doi.org/10.1103/PhysRevD.90.072006. arXiv:1406.0324
59. ATLAS Collaboration, Measurement of the inclusive jet cross-sections in proton–proton collisions at $\sqrt{s} = 8$ TeV with the ATLAS detector. JHEP **09**, 020 (2017). https://doi.org/10.1007/JHEP09(2017)020. arXiv:1706.03192
60. CMS Collaboration, Measurement and QCD analysis of double-differential inclusive jet cross sections in proton–proton collisions at $\sqrt{s} = 13$ TeV. JHEP **02**, 142 (2022). https://doi.org/10.1007/JHEP02(2022)142. arXiv:2111.10431
61. CMS Collaboration, Addendum to: Measurement and QCD analysis of double-differential inclusive jet cross sections in proton–proton collisions at $\sqrt{s} = 13$ TeV. JHEP **12**, 035 (2022). https://doi.org/10.1007/JHEP12(2022)035. arXiv:2111.10431
62. H1 and ZEUS Collaborations, Impact of jet-production data on the next-to-next-to-leading-order determination of HERAPDF2.0 parton distributions. Eur. Phys. J. C **82**, 243 (2022). https://doi.org/10.1140/epjc/s10052-022-10083-9. arXiv:2112.01120
63. J. Bellm et al., Jet cross sections at the LHC and the quest for higher precision. Eur. Phys. J. C **80**, 93 (2020). https://doi.org/10.1140/epjc/s10052-019-7574-x. arXiv:1903.12563
64. S. Alekhin et al., HERAFitter: open source QCD fit project. Eur. Phys. J. C **75**, 304 (2015). https://doi.org/10.1140/epjc/s10052-015-3480-z. arXiv:1410.4412
65. V. Bertone et al., xFitter 2.0.0: An open source QCD fit framework, in *Proceedings of XXV International Workshop on Deep-Inelastic Scattering and Related Subjects—PoS(DIS2017)*, vol. 297. (2017), p. 203. https://doi.org/10.22323/1.297.0203. arXiv:1709.01151
66. Y.L. Dokshitzer, Calculation of the structure functions for deep inelastic scattering and e^+e^- annihilation by perturbation theory in quantum chromodynamics. Sov. Phys. JETP **46**, 641 (1977)
67. V.N. Gribov, L.N. Lipatov, Deep inelastic ep scattering in perturbation theory. Sov. J. Nucl. Phys. **15**, 438 (1972)
68. G. Altarelli, G. Parisi, Asymptotic freedom in parton language. Nucl. Phys. B **126**, 298 (1977). https://doi.org/10.1016/0550-3213(77)90384-4
69. M. Botje, QCDNUM: fast QCD evolution and convolution. Comput. Phys. Commun. **182**, 490 (2011). https://doi.org/10.1016/j.cpc.2010.10.020. arXiv:1005.1481
70. R.S. Thorne, R.G. Roberts, Ordered analysis of heavy flavor production in deep inelastic scattering. Phys. Rev. D **57**, 6871 (1998). https://doi.org/10.1103/PhysRevD.57.6871. arXiv:hep-ph/9709442
71. R.S. Thorne, Variable-flavor number scheme for next-to-next-to-leading order. Phys. Rev. D **73**, 054019 (2006). https://doi.org/10.1103/PhysRevD.73.054019. arXiv:hep-ph/0601245

72. R.S. Thorne, Effect of changes of variable flavor number scheme on parton distribution functions and predicted cross sections. Phys. Rev. D **86**, 074017 (2012). https://doi.org/10.1103/PhysRevD.86.074017. arXiv:1201.6180
73. W.T. Giele, S. Keller, Implications of hadron collider observables on parton distribution function uncertainties. Phys. Rev. D **58**, 094023 (1998). https://doi.org/10.1103/PhysRevD.58.094023. arXiv:hep-ph/9803393
74. W.T. Giele, S.A. Keller, D.A. Kosower, Parton distribution function uncertainties (2001). arXiv:hep-ph/0104052
75. J. Pumplin et al., Uncertainties of predictions from parton distribution functions. II. The Hessian method. Phys. Rev. D **65**, 014013 (2001). https://doi.org/10.1103/PhysRevD.65.014013. arXiv:hep-ph/0101032
76. Particle Data Group, R.L. Workman et al., Review of particle physics. Prog. Theor. Exp. Phys. **2022**, 083C01 (2022). https://doi.org/10.1093/ptep/ptac097
77. CMS Collaboration, Measurement and QCD analysis of double-differential inclusive jet cross sections in pp collisions at $\sqrt{s} = 8$ TeV and cross section ratios to 2.76 and 7 TeV. JHEP **03**, 156 (2017). https://doi.org/10.1007/JHEP03(2017)156. arXiv:1609.05331

CMS Collaboration

Yerevan Physics Institute, Yerevan, Armenia
A. Hayrapetyan, A. Tumasyan [1]

Institut für Hochenergiephysik, Vienna, Austria
W. Adam, J. W. Andrejkovic, T. Bergauer, S. Chatterjee, K. Damanakis, M. Dragicevic, A. Escalante Del Valle, P. S. Hussain, M. Jeitler [2], N. Krammer, L. Lechner, D. Liko, I. Mikulec, J. Schieck [2], R. Schöfbeck, D. Schwarz, M. Sonawane, S. Templ, W. Waltenberger, C.-E. Wulz [2]

Universiteit Antwerpen, Antwerpen, Belgium
M. R. Darwish [3], T. Janssen, T. Kello [4], P. Van Mechelen

Vrije Universiteit Brussel, Brussel, Belgium
E. S. Bols, J. D'Hondt, A. De Moor, M. Delcourt, H. El Faham, S. Lowette, I. Makarenko, A. Morton, D. Müller, A. R. Sahasransu, S. Tavernier, S. Van Putte, D. Vannerom

Université Libre de Bruxelles, Bruxelles, Belgium
B. Clerbaux, S. Dansana, G. De Lentdecker, L. Favart, D. Hohov, J. Jaramillo, K. Lee, M. Mahdavikhorrami, A. Malara, S. Paredes, L. Pétré, N. Postiau, L. Thomas, M. Vanden Bemden, C. Vander Velde, P. Vanlaer

Ghent University, Ghent, Belgium
M. De Coen, D. Dobur, J. Knolle, L. Lambrecht, G. Mestdach, C. Rendón, A. Samalan, K. Skovpen, M. Tytgat, N. Van Den Bossche, B. Vermassen, L. Wezenbeek

Université Catholique de Louvain, Louvain-la-Neuve, Belgium
A. Benecke, G. Bruno, F. Bury, C. Caputo, C. Delaere, I. S. Donertas, A. Giammanco, K. Jaffel, Sa. Jain, V. Lemaitre, J. Lidrych, P. Mastrapasqua, K. Mondal, T. T. Tran, S. Wertz

Centro Brasileiro de Pesquisas Fisicas, Rio de Janeiro, Brazil
G. A. Alves, E. Coelho, C. Hensel, A. Moraes, P. Rebello Teles

Universidade do Estado do Rio de Janeiro, Rio de Janeiro, Brazil
W. L. Aldá Júnior, M. Alves Gallo Pereira, M. Barroso Ferreira Filho, H. Brandao Malbouisson, W. Carvalho, J. Chinellato [5], E. M. Da Costa, G. G. Da Silveira [6], D. De Jesus Damiao, V. Dos Santos Sousa, S. Fonseca De Souza, J. Martins [7], C. Mora Herrera, K. Mota Amarilo, L. Mundim, H. Nogima, A. Santoro, S. M. Silva Do Amaral, A. Sznajder, M. Thiel, A. Vilela Pereira

Universidade Estadual Paulista, Universidade Federal do ABC, São Paulo, Brazil
C. A. Bernardes [6], L. Calligaris, T. R. Fernandez Perez Tomei, E. M. Gregores, P. G. Mercadante, S. F. Novaes, B. Orzari, Sandra S. Padula

Institute for Nuclear Research and Nuclear Energy, Bulgarian Academy of Sciences, Sofia, Bulgaria
A. Aleksandrov, G. Antchev, R. Hadjiiska, P. Iaydjiev, M. Misheva, M. Shopova, G. Sultanov

University of Sofia, Sofia, Bulgaria
A. Dimitrov, T. Ivanov, L. Litov, B. Pavlov, P. Petkov, A. Petrov, E. Shumka

Instituto De Alta Investigación, Universidad de Tarapacá, Casilla 7 D, Arica, Chile
S. Keshri, S. Thakur

Beihang University, Beijing, China
T. Cheng, Q. Guo, T. Javaid[8], M. Mittal, L. Yuan

Department of Physics, Tsinghua University, Beijing, China
G. Bauer[9], Z. Hu, K. Yi[9,10]

Institute of High Energy Physics, Beijing, China
G. M. Chen[8], H. S. Chen[8], M. Chen[8], F. Iemmi, C. H. Jiang, A. Kapoor, H. Liao, Z.-A. Liu[11], F. Monti, R. Sharma, J. N. Song, J. Tao, C. Wang, J. Wang, H. Zhang

State Key Laboratory of Nuclear Physics and Technology, Peking University, Beijing, China
A. Agapitos, Y. Ban, A. Levin, C. Li, Q. Li, X. Lyu, Y. Mao, S. J. Qian, X. Sun, D. Wang, H. Yang

Sun Yat-Sen University, Guangzhou, China
M. Lu, Z. You

University of Science and Technology of China, Hefei, China
N. Lu

Institute of Modern Physics and Key Laboratory of Nuclear Physics and Ion-beam Application (MOE)-Fudan University, Shanghai, China
X. Gao[4], D. Leggat, H. Okawa, Y. Zhang

Zhejiang University, Hangzhou, Zhejiang, China
Z. Lin, C. Lu, M. Xiao

Universidad de Los Andes, Bogota, Colombia
C. Avila, D. A. Barbosa Trujillo, A. Cabrera, C. Florez, J. Fraga, J. A. Reyes Vega

Universidad de Antioquia, Medellin, Colombia
J. Mejia Guisao, F. Ramirez, M. Rodriguez, J. D. Ruiz Alvarez

Faculty of Electrical Engineering, Mechanical Engineering and Naval Architecture, University of Split, Split, Croatia
D. Giljanovic, N. Godinovic, D. Lelas, A. Sculac

Faculty of Science, University of Split, Split, Croatia
M. Kovac, T. Sculac

Institute Rudjer Boskovic, Zagreb, Croatia
P. Bargassa, V. Brigljevic, B. K. Chitroda, D. Ferencek, S. Mishra, A. Starodumov[11], T. Susa

University of Cyprus, Nicosia, Cyprus
A. Attikis, K. Christoforou, S. Konstantinou, J. Mousa, C. Nicolaou, F. Ptochos, P. A. Razis, H. Rykaczewski, H. Saka, A. Stepennov

Charles University, Prague, Czech Republic
M. Finger, M. Finger Jr., A. Kveton

Escuela Politecnica Nacional, Quito, Ecuador
E. Ayala

Universidad San Francisco de Quito, Quito, Ecuador

E. Carrera Jarrin

Academy of Scientific Research and Technology of the Arab Republic of Egypt, Egyptian Network of High Energy Physics, Cairo, Egypt
A. A. Abdelalim[12,13], E. Salama[14,15]

Center for High Energy Physics (CHEP-FU), Fayoum University, El-Fayoum, Egypt
M. A. Mahmoud, Y. Mohammed

National Institute of Chemical Physics and Biophysics, Tallinn, Estonia
K. Ehataht, M. Kadastik, T. Lange, S. Nandan, C. Nielsen, J. Pata, M. Raidal, L. Tani, C. Veelken

Department of Physics, University of Helsinki, Helsinki, Finland
H. Kirschenmann, K. Osterberg, M. Voutilainen

Helsinki Institute of Physics, Helsinki, Finland
S. Bharthuar, E. Brücken, F. Garcia, J. Havukainen, K. T. S. Kallonen, M. S. Kim, R. Kinnunen, T. Lampén, K. Lassila-Perini, S. Lehti, T. Lindén, M. Lotti, L. Martikainen, M. Myllymäki, M.m. Rantanen, H. Siikonen, E. Tuominen, J. Tuominiemi

Lappeenranta-Lahti University of Technology, Lappeenranta, Finland
P. Luukka, H. Petrow, T. Tuuva†

IRFU, CEA, Université Paris-Saclay, Gif-sur-Yvette, France
C. Amendola, M. Besancon, F. Couderc, M. Dejardin, D. Denegri, J. L. Faure, F. Ferri, S. Ganjour, P. Gras, G. Hamel de Monchenault, V. Lohezic, J. Malcles, J. Rander, A. Rosowsky, M.Ö. Sahin, A. Savoy-Navarro[16], P. Simkina, M. Titov

Laboratoire Leprince-Ringuet, CNRS/IN2P3, Ecole Polytechnique, Institut Polytechnique de Paris, Palaiseau, France
C. Baldenegro Barrera, F. Beaudette, A. Buchot Perraguin, P. Busson, A. Cappati, C. Charlot, F. Damas, O. Davignon, B. Diab, G. Falmagne, B. A. Fontana Santos Alves, S. Ghosh, R. Granier de Cassagnac, A. Hakimi, B. Harikrishnan, G. Liu, J. Motta, M. Nguyen, C. Ochando, L. Portales, R. Salerno, U. Sarkar, J. B. Sauvan, Y. Sirois, A. Tarabini, E. Vernazza, A. Zabi, A. Zghiche

Université de Strasbourg, CNRS, IPHC UMR 7178, Strasbourg, France
J.-L. Agram[17], J. Andrea, D. Apparu, D. Bloch, J.-M. Brom, E. C. Chabert, C. Collard, U. Goerlach, C. Grimault, A.-C. Le Bihan, P. Van Hove

Institut de Physique des 2 Infinis de Lyon (IP2I), Villeurbanne, France
S. Beauceron, B. Blancon, G. Boudoul, N. Chanon, J. Choi, D. Contardo, P. Depasse, C. Dozen[18], H. El Mamouni, J. Fay, S. Gascon, M. Gouzevitch, C. Greenberg, G. Grenier, B. Ille, I. B. Laktineh, M. Lethuillier, L. Mirabito, S. Perries, M. Vander Donckt, P. Verdier, J. Xiao

Georgian Technical University, Tbilisi, Georgia
G. Adamov, I. Lomidze, Z. Tsamalaidze[11]

I. Physikalisches Institut, RWTH Aachen University, Aachen, Germany
V. Botta, L. Feld, K. Klein, M. Lipinski, D. Meuser, A. Pauls, N. Röwert, M. Teroerde

III. Physikalisches Institut A, RWTH Aachen University, Aachen, Germany
S. Diekmann, A. Dodonova, N. Eich, D. Eliseev, M. Erdmann, P. Fackeldey, B. Fischer, T. Hebbeker, K. Hoepfner, F. Ivone, M. Y. Lee, L. Mastrolorenzo, M. Merschmeyer, A. Meyer, S. Mondal, S. Mukherjee, D. Noll, A. Novak, F. Nowotny, A. Pozdnyakov, Y. Rath, W. Redjeb, F. Rehm, H. Reithler, A. Schmidt, S. C. Schuler, A. Sharma, A. Stein, F. Torres Da Silva De Araujo[19], L. Vigilante, S. Wiedenbeck, S. Zaleski

III. Physikalisches Institut B, RWTH Aachen University, Aachen, Germany
C. Dziwok, G. Flügge, W. Haj Ahmad[20], T. Kress, A. Nowack, O. Pooth, A. Stahl, T. Ziemons, A. Zotz

Deutsches Elektronen-Synchrotron, Hamburg, Germany
H. Aarup Petersen, M. Aldaya Martin, J. Alimena, S. Amoroso, Y. An, S. Baxter, M. Bayatmakou, H. Becerril Gonzalez, O. Behnke, S. Bhattacharya, F. Blekman[21], K. Borras[22], D. Brunner, A. Campbell, A. Cardini, C. Cheng, F. Colombina, S. Consuegra Rodríguez, G. Correia Silva, M. De Silva, G. Eckerlin, D. Eckstein, L. I. Estevez Banos, O. Filatov, E. Gallo[21], A. Geiser, A. Giraldi, G. Greau, V. Guglielmi, M. Guthoff, A. Jafari[23], N. Z. Jomhari, B. Kaech, M. Kasemann, H. Kaveh, C. Kleinwort, R. Kogler, M. Komm, D. Krücker, W. Lange, D. Leyva Pernia, K. Lipka[24], W. Lohmann[25], R. Mankel, I.-A. Melzer-Pellmann, M. Mendizabal Morentin, J. Metwally, A. B. Meyer, G. Milella, M. Mormile, A. Mussgiller, A. Nürnberg, Y. Otarid, D. Pérez Adán, E. Ranken, A. Raspereza, B. Ribeiro Lopes, J. Rübenach, A. Saggio, M. Scham[22,26], V. Scheurer, S. Schnake[22], P. Schütze, C. Schwanenberger[21], M. Shchedrolosiev, R. E. Sosa Ricardo, L. P. Sreelatha Pramod, D. Stafford, F. Vazzoler, A. Ventura Barroso, R. Walsh, Q. Wang, Y. Wen, K. Wichmann, L. Wiens[22], C. Wissing, S. Wuchterl, Y. Yang, A. Zimermmane Castro Santos

University of Hamburg, Hamburg, Germany
A. Albrecht, S. Albrecht, M. Antonello, S. Bein, L. Benato, M. Bonanomi, P. Connor, K. De Leo, M. Eich, K. El Morabit, Y. Fischer, A. Fröhlich, C. Garbers, E. Garutti, A. Grohsjean, M. Hajheidari, J. Haller, A. Hinzmann, H. R. Jabusch, G. Kasieczka, P. Keicher, R. Klanner, W. Korcari, T. Kramer, V. Kutzner, F. Labe, J. Lange, A. Lobanov, C. Matthies, A. Mehta, L. Moureaux, M. Mrowietz, A. Nigamova, Y. Nissan, A. Paasch, K. J. Pena Rodriguez, T. Quadfasel, M. Rieger, D. Savoiu, J. Schindler, P. Schleper, M. Schröder, J. Schwandt, M. Sommerhalder, H. Stadie, G. Steinbrück, A. Tews, M. Wolf

Karlsruher Institut fuer Technologie, Karlsruhe, Germany
S. Brommer, M. Burkart, E. Butz, T. Chwalek, A. Dierlamm, A. Droll, N. Faltermann, M. Giffels, A. Gottmann, F. Hartmann[27], M. Horzela, U. Husemann, M. Klute, R. Koppenhöfer, M. Link, A. Lintuluoto, S. Maier, S. Mitra, Th. Müller, M. Neukum, M. Oh, G. Quast, K. Rabbertz, I. Shvetsov, H. J. Simonis, N. Trevisani, R. Ulrich, J. van der Linden, R. F. Von Cube, M. Wassmer, S. Wieland, R. Wolf, S. Wunsch, X. Zuo

Institute of Nuclear and Particle Physics (INPP), NCSR Demokritos, Aghia Paraskevi, Greece
G. Anagnostou, P. Assiouras, G. Daskalakis, A. Kyriakis, A. Stakia

National and Kapodistrian University of Athens, Athens, Greece
D. Karasavvas, P. Kontaxakis, G. Melachroinos, A. Panagiotou, I. Papavergou, I. Paraskevas, N. Saoulidou, K. Theofilatos, E. Tziaferi, K. Vellidis, I. Zisopoulos

National Technical University of Athens, Athens, Greece
G. Bakas, T. Chatzistavrou, G. Karapostoli, K. Kousouris, I. Papakrivopoulos, E. Siamarkou, G. Tsipolitis, A. Zacharopoulou

University of Ioánnina, Ioánnina, Greece
K. Adamidis, I. Bestintzanos, I. Evangelou, C. Foudas, P. Gianneios, C. Kamtsikis, P. Katsoulis, P. Kokkas, P. G. Kosmoglou Kioseoglou, N. Manthos, I. Papadopoulos, J. Strologas

HUN-REN Wigner Research Centre for Physics, Budapest, Hungary
M. Bartók[28], C. Hajdu, D. Horvath[29,30], F. Sikler, V. Veszpremi

MTA-ELTE Lendület CMS Particle and Nuclear Physics Group, Eötvös Loránd University, Budapest, Hungary
M. Csanád, K. Farkas, M. M. A. Gadallah[31], P. Major, K. Mandal, G. Pásztor, A. J. Rádl[32], O. Surányi, G. I. Veres

Institute of Nuclear Research ATOMKI, Debrecen, Hungary
G. Bencze, S. Czellar, J. Karancsi[28], J. Molnar, Z. Szillasi

Institute of Physics, University of Debrecen, Debrecen, Hungary
P. Raics, B. Ujvari[33], G. Zilizi

Karoly Robert Campus, MATE Institute of Technology, Gyongyos, Hungary
T. Csorgo[32], F. Nemes[32], T. Novak

Panjab University, Chandigarh, India
J. Babbar, S. Bansal, S. B. Beri, V. Bhatnagar, G. Chaudhary, S. Chauhan, N. Dhingra[34], R. Gupta, A. Kaur, A. Kaur, H. Kaur, M. Kaur, S. Kumar, P. Kumari, M. Meena, K. Sandeep, T. Sheokand, J. B. Singh[35], A. Singla

University of Delhi, Delhi, India
A. Ahmed, A. Bhardwaj, A. Chhetri, B. C. Choudhary, A. Kumar, M. Naimuddin, K. Ranjan, S. Saumya

Saha Institute of Nuclear Physics, HBNI, Kolkata, India
S. Baradia, S. Barman[36], S. Bhattacharya, D. Bhowmik, S. Dutta, S. Dutta, B. Gomber[37], P. Palit, G. Saha, B. Sahu[37], S. Sarkar

Indian Institute of Technology Madras, Madras, India
P. K. Behera, S. C. Behera, S. Chatterjee, P. Jana, P. Kalbhor, J. R. Komaragiri[38], D. Kumar[38], M. Mohammad Mobassir Ameen, A. Muhammad, L. Panwar[38], R. Pradhan, P. R. Pujahari, N. R. Saha, A. Sharma, A. K. Sikdar, S. Verma

Tata Institute of Fundamental Research-A, Mumbai, India
T. Aziz, I. Das, S. Dugad, M. Kumar, G. B. Mohanty, P. Suryadevara

Tata Institute of Fundamental Research-B, Mumbai, India
A. Bala, S. Banerjee, M. Guchait, S. Karmakar, S. Kumar, G. Majumder, K. Mazumdar, S. Mukherjee, A. Thachayath

National Institute of Science Education and Research, An OCC of Homi Bhabha National Institute, Bhubaneswar, Odisha, India
S. Bahinipati[39], A. K. Das, C. Kar, D. Maity, P. Mal, T. Mishra, V. K. Muraleedharan Nair Bindhu[40], K. Naskar[40], A. Nayak[40], P. Saha, S. K. Swain, S. Varghese[40], D. Vats[40]

Indian Institute of Science Education and Research (IISER), Pune, India
A. Alpana, S. Dube, B. Kansal, A. Laha, S. Pandey, A. Rastogi, S. Sharma

Isfahan University of Technology, Isfahan, Iran
H. Bakhshiansohi[41,42], E. Khazaie[42], M. Zeinali[43]

Institute for Research in Fundamental Sciences (IPM), Tehran, Iran
S. Chenarani[44], S. M. Etesami, M. Khakzad, M. Mohammadi Najafabadi

University College Dublin, Dublin, Ireland
M. Grunewald

INFN Sezione di Bari[a], Università di Bari[b], Politecnico di Bari[c], Bari, Italy
M. Abbrescia[a,b], R. Aly[a,b,12], C. Aruta[a,b], A. Colaleo[a], D. Creanza[a,c], B. D'Anzi[a,b], N. De Filippis[a,c], M. De Palma[a,b], A. Di Florio[a,b], W. Elmetenawee[a,b], F. Errico[a,b], L. Fiore[a], G. Iaselli[a,c], G. Maggi[a,c], M. Maggi[a], V. Mastrapasqua[a,b], S. My[a,b], S. Nuzzo[a,b], A. Pellecchia[a,b], A. Pompili[a,b], G. Pugliese[a,c], R. Radogna[a], D. Ramos[a], A. Ranieri[a], L. Silvestris[a], Ü. Sözbilir[a], A. Stamerra[a], R. Venditti[a], P. Verwilligen[a], A. Zaza[a,b]

INFN Sezione di Bologna[a], Università di Bologna[b], Bologna, Italy

G. Abbiendi[a], C. Battilana[a,b], D. Bonacorsi[a,b], L. Borgonovi[a], P. Capiluppi[a,b], A. Castro[a,b], F. R. Cavallo[a], M. Cuffiani[a,b], G. M. Dallavalle[a], T. Diotalevi[a,b], F. Fabbri[a], A. Fanfani[a,b], D. Fasanella[a,b], P. Giacomelli[a], L. Giommi[a,b], C. Grandi[a], L. Guiducci[a,b], S. Lo Meo[a,45], L. Lunerti[a,b], S. Marcellini[a], G. Masetti[a], F. L. Navarria[a,b], A. Perrotta[a], F. Primavera[a,b], A. M. Rossi[a,b], T. Rovelli[a,b], G. P. Siroli[a,b]

INFN Sezione di Catania[a], Università di Catania[b], Catania, Italy
S. Costa[a,b,46], A. Di Mattia[a], R. Potenza[a,b], A. Tricomi[a,b,46], C. Tuve[a,b]

INFN Sezione di Firenze[a], Università di Firenze[b], Firenze, Italy
G. Barbagli[a], G. Bardelli[a,b], B. Camaiani[a,b], A. Cassese[a], R. Ceccarelli[a,b], V. Ciulli[a,b], C. Civinini[a], R. D'Alessandro[a,b], E. Focardi[a,b], G. Latino[a,b], P. Lenzi[a,b], M. Lizzo[a,b], M. Meschini[a], S. Paoletti[a], G. Sguazzoni[a], L. Viliani[a]

INFN Laboratori Nazionali di Frascati, Frascati, Italy
L. Benussi, S. Bianco, S. Meola[47], D. Piccolo

INFN Sezione di Genova[a], Università di Genova[b], Genoa, Italy
P. Chatagnon[a], F. Ferro[a], E. Robutti[a], S. Tosi[a,b]

INFN Sezione di Milano-Bicocca[a], Università di Milano-Bicocca[b], Milan, Italy
A. Benaglia[a], G. Boldrini[a], F. Brivio[a,b], F. Cetorelli[a,b], F. De Guio[a,b], M. E. Dinardo[a,b], P. Dini[a], S. Gennai[a], A. Ghezzi[a,b], P. Govoni[a,b], L. Guzzi[a,b], M. T. Lucchini[a,b], M. Malberti[a], S. Malvezzi[a], A. Massironi[a], D. Menasce[a], L. Moroni[a], M. Paganoni[a,b], D. Pedrini[a], B. S. Pinolini[a], S. Ragazzi[a,b], N. Redaelli[a], T. Tabarelli de Fatis[a,b], D. Zuolo[a,b]

INFN Sezione di Napoli[a], Università di Napoli 'Federico II'[b], Napoli, Italy; Università della Basilicata[c], Potenza, Italy; Scuola Superiore Meridionale (SSM)[d], Naples, Italy
S. Buontempo[a], A. Cagnotta[a,b], F. Carnevali[a,b], N. Cavallo[a,c], A. De Iorio[a,b], F. Fabozzi[a,c], A. O. M. Iorio[a,b], L. Lista[a,b,48], P. Paolucci[a,27], B. Rossi[a], C. Sciacca[a,b]

INFN Sezione di Padova[a], Università di Padova[b], Padova, Italy; Università di Trento[c], Trento, Italy
R. Ardino[a], P. Azzi[a], N. Bacchetta[a,49], D. Bisello[a,b], P. Bortignon[a], A. Bragagnolo[a,b], R. Carlin[a,b], P. Checchia[a], T. Dorigo[a], F. Gasparini[a,b], U. Gasparini[a,b], G. Grosso[a], M. Gulmini[a,50], L. Layer[a,51], E. Lusiani[a], M. Margoni[a,b], A. T. Meneguzzo[a,b], M. Migliorini[a,b], J. Pazzini[a,b], P. Ronchese[a,b], R. Rossin[a,b], F. Simonetto[a,b], G. Strong[a], M. Tosi[a,b], A. Triossi[a,b], H. Yarar[a,b], M. Zanetti[a,b], P. Zotto[a,b], A. Zucchetta[a,b], G. Zumerle[a,b]

INFN Sezione di Pavia[a], Università di Pavia[b], Pavia, Italy
S. Abu Zeid[a,15], C. Aimè[a,b], A. Braghieri[a], S. Calzaferri[a,b], D. Fiorina[a,b], P. Montagna[a,b], V. Re[a], C. Riccardi[a,b], P. Salvini[a], I. Vai[a,b], P. Vitulo[a,b]

INFN Sezione di Perugia[a], Università di Perugia[b], Perugia, Italy
P. Asenov[a,52], G. M. Bilei[a], D. Ciangottini[a,b], L. Fanò[a,b], M. Magherini[a,b], G. Mantovani[a,b], V. Mariani[a,b], M. Menichelli[a], F. Moscatelli[a,52], A. Piccinelli[a,b], M. Presilla[a,b], A. Rossi[a,b], A. Santocchia[a,b], D. Spiga[a], T. Tedeschi[a,b]

INFN Sezione di Pisa[a], Università di Pisa[b], Scuola Normale Superiore di Pisa[c], Pisa, Italy; Università di Siena[d], Siena, Italy
P. Azzurri[a], G. Bagliesi[a], R. Bhattacharya[a], L. Bianchini[a,b], T. Boccali[a], E. Bossini[a,b], D. Bruschini[a,c], R. Castaldi[a], M. A. Ciocci[a,b], V. D'Amante[a,d], R. Dell'Orso[a], S. Donato[a], A. Giassi[a], F. Ligabue[a,c], D. Matos Figueiredo[a], A. Messineo[a,b], M. Musich[a,b], F. Palla[a], S. Parolia[a], G. Ramirez-Sanchez[a,c], A. Rizzi[a,b], G. Rolandi[a,c], S. Roy Chowdhury[a], T. Sarkar[a], A. Scribano[a], P. Spagnolo[a], R. Tenchini[a], G. Tonelli[a,b], N. Turini[a,d], A. Venturi[a], P. G. Verdini[a]

INFN Sezione di Roma[a], Sapienza Università di Roma[b], Rome, Italy

P. Barria[a], M. Campana[a,b], F. Cavallari[a], L. Cunqueiro Mendez[a,b], D. Del Re[a,b], E. Di Marco[a], M. Diemoz[a], E. Longo[a,b], P. Meridiani[a], J. Mijuskovic[a,b,53], G. Organtini[a,b], F. Pandolfi[a], R. Paramatti[a,b], C. Quaranta[a,b], S. Rahatlou[a,b], C. Rovelli[a], F. Santanastasio[a,b], L. Soffi[a], R. Tramontano[a,b]

INFN Sezione di Torino[a], Università di Torino[b], Torino, Italy; Università del Piemonte Orientale[c], Novara, Italy
N. Amapane[a,b], R. Arcidiacono[a,c], S. Argiro[a,b], M. Arneodo[a,c], N. Bartosik[a], R. Bellan[a,b], A. Bellora[a,b], C. Biino[a], N. Cartiglia[a], M. Costa[a,b], R. Covarelli[a,b], N. Demaria[a], L. Finco[a], M. Grippo[a,b], B. Kiani[a,b], F. Legger[a], F. Luongo[a,b], C. Mariotti[a], S. Maselli[a], A. Mecca[a,b], E. Migliore[a,b], M. Monteno[a], R. Mulargia[a], M. M. Obertino[a,b], G. Ortona[a], L. Pacher[a,b], N. Pastrone[a], M. Pelliccioni[a], M. Ruspa[a,c], K. Shchelina[a], F. Siviero[a,b], V. Sola[a,b], A. Solano[a,b], D. Soldi[a,b], A. Staiano[a], C. Tarricone[a,b], M. Tornago[a,b], D. Trocino[a], G. Umoret[a,b], A. Vagnerini[a,b], E. Vlasov[a,b]

INFN Sezione di Trieste[a], Università di Trieste[b], Trieste, Italy
S. Belforte[a], V. Candelise[a,b], M. Casarsa[a], F. Cossutti[a], G. Della Ricca[a,b], G. Sorrentino[a,b]

Kyungpook National University, Daegu, Korea
S. Dogra, C. Huh, B. Kim, D. H. Kim, J. Kim, J. Lee, S. W. Lee, C. S. Moon, Y. D. Oh, S. I. Pak, M. S. Ryu, S. Sekmen, Y. C. Yang

Chonnam National University, Institute for Universe and Elementary Particles, Kwangju, Korea
G. Bak, P. Gwak, H. Kim, D. H. Moon

Hanyang University, Seoul, Korea
E. Asilar, T. J. Kim, J. Park

Korea University, Seoul, Korea
S. Choi, S. Han, B. Hong, K. Lee, K. S. Lee, J. Lim, J. Park, S. K. Park, J. Yoo

Kyung Hee University, Department of Physics, Seoul, Korea
J. Goh

Sejong University, Seoul, Korea
H. S. Kim, Y. Kim, S. Lee

Seoul National University, Seoul, Korea
J. Almond, J. H. Bhyun, J. Choi, S. Jeon, J. Kim, J. S. Kim, S. Ko, H. Kwon, H. Lee, S. Lee, B. H. Oh, S. B. Oh, H. Seo, U. K. Yang, I. Yoon

University of Seoul, Seoul, Korea
W. Jang, D. Y. Kang, Y. Kang, D. Kim, S. Kim, B. Ko, J. S. H. Lee, Y. Lee, J. A. Merlin, I. C. Park, Y. Roh, I. J. Watson, S. Yang

Department of Physics, Yonsei University, Seoul, Korea
S. Ha, H. D. Yoo

Sungkyunkwan University, Suwon, Korea
M. Choi, M. R. Kim, H. Lee, Y. Lee, I. Yu

College of Engineering and Technology, American University of the Middle East (AUM), Dasman, Kuwait
T. Beyrouthy, Y. Maghrbi

Riga Technical University, Riga, Latvia
K. Dreimanis, A. Gaile, G. Pikurs, A. Potrebko, M. Seidel, V. Veckalns[54]

University of Latvia (LU), Riga, Latvia
N. R. Strautnieks

Vilnius University, Vilnius, Lithuania
M. Ambrozas, A. Juodagalvis, A. Rinkevicius, G. Tamulaitis

National Centre for Particle Physics, Universiti Malaya, Kuala Lumpur, Malaysia
N. Bin Norjoharuddeen, I. Yusuff[55], Z. Zolkapli

Universidad de Sonora (UNISON), Hermosillo, Mexico
J. F. Benitez, A. Castaneda Hernandez, H. A. Encinas Acosta, L. G. Gallegos Maríñez, M. León Coello, J. A. Murillo Quijada, A. Sehrawat, L. Valencia Palomo

Centro de Investigacion y de Estudios Avanzados del IPN, Mexico City, Mexico
G. Ayala, H. Castilla-Valdez, E. De La Cruz-Burelo, I. Heredia-De La Cruz[56], R. Lopez-Fernandez, C. A. Mondragon Herrera, D. A. Perez Navarro, A. Sánchez Hernández

Universidad Iberoamericana, Mexico City, Mexico
C. Oropeza Barrera, M. Ramírez García

Benemerita Universidad Autonoma de Puebla, Puebla, Mexico
I. Pedraza, H. A. Salazar Ibarguen, C. Uribe Estrada

University of Montenegro, Podgorica, Montenegro
I. Bubanja, N. Raicevic

University of Canterbury, Christchurch, New Zealand
P. H. Butler

National Centre for Physics, Quaid-I-Azam University, Islamabad, Pakistan
A. Ahmad, M. I. Asghar, A. Awais, M. I. M. Awan, H. R. Hoorani, W. A. Khan

AGH University of Krakow, Faculty of Computer Science, Electronics and Telecommunications, Kraków, Poland
V. Avati, L. Grzanka, M. Malawski

National Centre for Nuclear Research, Swierk, Poland
H. Bialkowska, M. Bluj, B. Boimska, M. Górski, M. Kazana, M. Szleper, P. Zalewski

Institute of Experimental Physics, Faculty of Physics, University of Warsaw, Warsaw, Poland
K. Bunkowski, K. Doroba, A. Kalinowski, M. Konecki, J. Krolikowski

Warsaw University of Technology, Warsaw, Poland
K. Pozniak, W. Zabolotny

Laboratório de Instrumentação e Física Experimental de Partículas, Lisbon, Portugal
M. Araujo, D. Bastos, C. Beirão Da Cruz E Silva, A. Boletti, M. Bozzo, P. Faccioli, M. Gallinaro, J. Hollar, N. Leonardo, T. Niknejad, M. Pisano, J. Seixas, J. Varela

Faculty of Physics, University of Belgrade, Belgrade, Serbia
P. Adzic, P. Milenovic

VINCA Institute of Nuclear Sciences, University of Belgrade, Belgrade, Serbia
M. Dordevic, J. Milosevic, V. Rekovic

Centro de Investigaciones Energéticas Medioambientales y Tecnológicas (CIEMAT), Madrid, Spain
M. Aguilar-Benitez, J. Alcaraz Maestre, M. Barrio Luna, Cristina F. Bedoya, M. Cepeda, M. Cerrada, N. Colino, B. De La Cruz, A. Delgado Peris, D. Fernández Del Val, J. P. Fernández Ramos, J. Flix, M. C. Fouz, O. Gonzalez Lopez, S. Goy Lopez, J. M. Hernandez, M. I. Josa, J. León Holgado, D. Moran, Á. Navarro Tobar, C. Perez Dengra, A. Pérez-Calero Yzquierdo, J. Puerta Pelayo, I. Redondo, D. D. Redondo Ferrero, L. Romero, S. Sánchez Navas, L. Urda Gómez, J. Vazquez Escobar, C. Willmott

Universidad Autónoma de Madrid, Madrid, Spain
J. F. de Trocóniz

Universidad de Oviedo, Instituto Universitario de Ciencias y Tecnologías Espaciales de Asturias (ICTEA), Oviedo, Spain
B. Alvarez Gonzalez, J. Cuevas, J. Fernandez Menendez, S. Folgueras, I. Gonzalez Caballero,

J. R. González Fernández, E. Palencia Cortezon, C. Ramón Álvarez, V. Rodríguez Bouza, A. Soto Rodríguez, A. Trapote, C. Vico Villalba, P. Vischia

Instituto de Física de Cantabria (IFCA), CSIC-Universidad de Cantabria, Santander, Spain
S. Bhowmik, S. Blanco Fernández, J. A. Brochero Cifuentes, I. J. Cabrillo, A. Calderon, J. Duarte Campderros, M. Fernandez, C. Fernandez Madrazo, G. Gomez, C. Lasaosa García, C. Martinez Rivero, P. Martinez Ruiz del Arbol, F. Matorras, P. Matorras Cuevas, E. Navarrete Ramos, J. Piedra Gomez, C. Prieels, L. Scodellaro, I. Vila, J. M. Vizan Garcia

University of Colombo, Colombo, Sri Lanka
M. K. Jayananda, B. Kailasapathy[57], D. U. J. Sonnadara, D. D. C. Wickramarathna

Department of Physics, University of Ruhuna, Matara, Sri Lanka
W. G. D. Dharmaratna, K. Liyanage, N. Perera, N. Wickramage

CERN, European Organization for Nuclear Research, Geneva, Switzerland
D. Abbaneo, E. Auffray, G. Auzinger, J. Baechler, D. Barney, A. Bermúdez Martínez, M. Bianco, B. Bilin, A. A. Bin Anuar, A. Bocci, E. Brondolin, C. Caillol, T. Camporesi, G. Cerminara, N. Chernyavskaya, M. Cipriani, D. d'Enterria, A. Dabrowski, A. David, A. De Roeck, M. M. Defranchis, M. Deile, M. Dobson, F. Fallavollita[58], L. Forthomme, G. Franzoni, W. Funk, S. Giani, D. Gigi, K. Gill, F. Glege, L. Gouskos, M. Haranko, J. Hegeman, T. James, J. Kieseler, N. Kratochwil, S. Laurila, P. Lecoq, E. Leutgeb, C. Lourenço, B. Maier, L. Malgeri, M. Mannelli, A. C. Marini, F. Meijers, S. Mersi, E. Meschi, F. Moortgat, M. Mulders, S. Orfanelli, F. Pantaleo, M. Peruzzi, A. Petrilli, G. Petrucciani, A. Pfeiffer, M. Pierini, D. Piparo, H. Qu, D. Rabady, G. Reales Gutiérrez, M. Rovere, H. Sakulin, S. Scarfi, M. Selvaggi, A. Sharma, P. Silva, P. Sphicas[59], A. G. Stahl Leiton, A. Steen, S. Summers, D. Treille, P. Tropea, A. Tsirou, D. Walter, J. Wanczyk[60], K. A. Wozniak, P. Zejdl, W. D. Zeuner

Paul Scherrer Institut, Villigen, Switzerland
T. Bevilacqua[61], L. Caminada[61], A. Ebrahimi, W. Erdmann, R. Horisberger, Q. Ingram, H. C. Kaestli, D. Kotlinski, C. Lange, M. Missiroli[61], L. Noehte[61], T. Rohe

ETH Zurich-Institute for Particle Physics and Astrophysics (IPA), Zurich, Switzerland
T. K. Aarrestad, K. Androsov[60], M. Backhaus, A. Calandri, K. Datta, A. De Cosa, G. Dissertori, M. Dittmar, M. Donegà, F. Eble, M. Galli, K. Gedia, F. Glessgen, C. Grab, D. Hits, W. Lustermann, A.-M. Lyon, R. A. Manzoni, L. Marchese, C. Martin Perez, A. Mascellani[60], F. Nessi-Tedaldi, F. Pauss, V. Perovic, S. Pigazzini, M. G. Ratti, M. Reichmann, C. Reissel, T. Reitenspiess, B. Ristic, F. Riti, D. Ruini, D. A. Sanz Becerra, R. Seidita, J. Steggemann[60], D. Valsecchi, R. Wallny

Universität Zürich, Zurich, Switzerland
C. Amsler[62], P. Bärtschi, C. Botta, D. Brzhechko, M. F. Canelli, K. Cormier, A. De Wit, R. Del Burgo, J. K. Heikkilä, M. Huwiler, W. Jin, A. Jofrehei, B. Kilminster, S. Leontsinis, S. P. Liechti, A. Macchiolo, P. Meiring, V. M. Mikuni, U. Molinatti, I. Neutelings, A. Reimers, P. Robmann, S. Sanchez Cruz, K. Schweiger, M. Senger, Y. Takahashi

National Central University, Chung-Li, Taiwan
C. Adloff[63], C. M. Kuo, W. Lin, P. K. Rout, P. C. Tiwari[38], S. S. Yu

National Taiwan University (NTU), Taipei, Taiwan
L. Ceard, Y. Chao, K. F. Chen, P.s. Chen, W.-S. Hou, Y.w. Kao, R. Khurana, G. Kole, Y. Y. Li, R.-S. Lu, E. Paganis, A. Psallidas, J. Thomas-Wilsker, H.y. Wu, E. Yazgan

High Energy Physics Research Unit, Department of Physics, Faculty of Science, Chulalongkorn University, Bangkok, Thailand
C. Asawatangtrakuldee, N. Srimanobhas, V. Wachirapusitanand

Physics Department, Science and Art Faculty, Çukurova University, Adana, Turkey

D. Agyel, F. Boran, Z. S. Demiroglu, F. Dolek, I. Dumanoglu[64], E. Eskut, Y. Guler[65], E. Gurpinar Guler[65], C. Isik, O. Kara, A. Kayis Topaksu, U. Kiminsu, G. Onengut, K. Ozdemir[66], A. Polatoz, B. Tali[67], U. G. Tok, S. Turkcapar, E. Uslan, I. S. Zorbakir

Physics Department, Middle East Technical University, Ankara, Turkey
K. Ocalan[68], M. Yalvac[69]

Bogazici University, Istanbul, Turkey
B. Akgun, I. O. Atakisi, E. Gülmez, M. Kaya[70], O. Kaya[71], S. Tekten[72]

Istanbul Technical University, Istanbul, Turkey
A. Cakir, K. Cankocak[64], Y. Komurcu, S. Sen[73]

Istanbul University, Istanbul, Turkey
O. Aydilek, S. Cerci[67], V. Epshteyn, B. Hacisahinoglu, I. Hos[74], B. Isildak[75], B. Kaynak, S. Ozkorucuklu, H. Sert, C. Simsek, D. Sunar Cerci[67], C. Zorbilmez

Institute for Scintillation Materials of National Academy of Science of Ukraine, Kharkiv, Ukraine
A. Boyaryntsev, B. Grynyov

National Science Centre, Kharkiv Institute of Physics and Technology, Kharkiv, Ukraine
L. Levchuk

University of Bristol, Bristol, UK
D. Anthony, J. J. Brooke, A. Bundock, E. Clement, D. Cussans, H. Flacher, M. Glowacki, J. Goldstein, H. F. Heath, L. Kreczko, B. Krikler, S. Paramesvaran, S. Seif El Nasr-Storey, V. J. Smith, N. Stylianou[76], K. Walkingshaw Pass, R. White

Rutherford Appleton Laboratory, Didcot, UK
A. H. Ball, K. W. Bell, A. Belyaev[77], C. Brew, R. M. Brown, D. J. A. Cockerill, C. Cooke, K. V. Ellis, K. Harder, S. Harper, M.-L. Holmberg[78], Sh. Jain, J. Linacre, K. Manolopoulos, D. M. Newbold, E. Olaiya, D. Petyt, T. Reis, G. Salvi, T. Schuh, C. H. Shepherd-Themistocleous, I. R. Tomalin, T. Williams

Imperial College, London, UK
R. Bainbridge, P. Bloch, C. E. Brown, O. Buchmuller, V. Cacchio, C. A. Carrillo Montoya, V. Cepaitis, G. S. Chahal[79], D. Colling, J. S. Dancu, P. Dauncey, G. Davies, J. Davies, M. Della Negra, S. Fayer, G. Fedi, G. Hall, M. H. Hassanshahi, A. Howard, G. Iles, J. Langford, L. Lyons, A.-M. Magnan, S. Malik, A. Martelli, M. Mieskolainen, J. Nash[80], M. Pesaresi, B. C. Radburn-Smith, A. Richards, A. Rose, C. Seez, R. Shukla, A. Tapper, K. Uchida, G. P. Uttley, L. H. Vage, T. Virdee[27], M. Vojinovic, N. Wardle, D. Winterbottom

Brunel University, Uxbridge, UK
K. Coldham, J. E. Cole, A. Khan, P. Kyberd, I. D. Reid

Baylor University, Waco, TX, USA
S. Abdullin, A. Brinkerhoff, B. Caraway, J. Dittmann, K. Hatakeyama, J. Hiltbrand, A. R. Kanuganti, B. McMaster, M. Saunders, S. Sawant, C. Sutantawibul, M. Toms, J. Wilson

Catholic University of America, Washington, DC, USA
R. Bartek, A. Dominguez, C. Huerta Escamilla, A. E. Simsek, R. Uniyal, A. M. Vargas Hernandez

The University of Alabama, Tuscaloosa, AL, USA
R. Chudasama, S. I. Cooper, S. V. Gleyzer, C. U. Perez, P. Rumerio[81], E. Usai, C. West

Boston University, Boston, MA, USA
A. Akpinar, A. Albert, D. Arcaro, C. Cosby, Z. Demiragli, C. Erice, E. Fontanesi, D. Gastler, J. Rohlf, K. Salyer, D. Sperka, D. Spitzbart, I. Suarez, A. Tsatsos, S. Yuan

Brown University, Providence, RI, USA

G. Benelli, X. Coubez[22], D. Cutts, M. Hadley, U. Heintz, J. M. Hogan[82], T. Kwon, G. Landsberg, K. T. Lau, D. Li, J. Luo, M. Narain, N. Pervan, S. Sagir[83], F. Simpson, W. Y. Wong, X. Yan, D. Yu, W. Zhang

University of California, Davis, Davis, CA, USA
S. Abbott, J. Bonilla, C. Brainerd, R. Breedon, M. Calderon De La Barca Sanchez, M. Chertok, J. Conway, P. T. Cox, R. Erbacher, G. Haza, F. Jensen, O. Kukral, G. Mocellin, M. Mulhearn, D. Pellett, B. Regnery, W. Wei, Y. Yao, F. Zhang

University of California, Los Angeles, CA, USA
M. Bachtis, R. Cousins, A. Datta, J. Hauser, M. Ignatenko, M. A. Iqbal, T. Lam, E. Manca, W. A. Nash, D. Saltzberg, B. Stone, V. Valuev

University of California, Riverside, Riverside, CA, USA
R. Clare, M. Gordon, G. Hanson, W. Si, S. Wimpenny[†]

University of California, San Diego, La Jolla, CA, USA
J. G. Branson, S. Cittolin, S. Cooperstein, D. Diaz, J. Duarte, R. Gerosa, L. Giannini, J. Guiang, R. Kansal, V. Krutelyov, R. Lee, J. Letts, M. Masciovecchio, F. Mokhtar, M. Pieri, M. Quinnan, B. V. Sathia Narayanan, V. Sharma, M. Tadel, E. Vourliotis, F. Würthwein, Y. Xiang, A. Yagil

Department of Physics , University of California, Santa Barbara, Santa Barbara, CA, USA
L. Brennan, C. Campagnari, M. Citron, G. Collura, A. Dorsett, J. Incandela, M. Kilpatrick, J. Kim, A. J. Li, P. Masterson, H. Mei, M. Oshiro, J. Richman, U. Sarica, R. Schmitz, F. Setti, J. Sheplock, D. Stuart, S. Wang

California Institute of Technology, Pasadena, CA, USA
A. Bornheim, O. Cerri, A. Latorre, J. M. Lawhorn, J. Mao, H. B. Newman, T. Q. Nguyen, M. Spiropulu, J. R. Vlimant, C. Wang, S. Xie, R. Y. Zhu

Carnegie Mellon University, Pittsburgh, PA, USA
J. Alison, S. An, M. B. Andrews, P. Bryant, V. Dutta, T. Ferguson, A. Harilal, C. Liu, T. Mudholkar, S. Murthy, M. Paulini, A. Roberts, A. Sanchez, W. Terrill

University of Colorado Boulder, Boulder, CO, USA
J. P. Cumalat, W. T. Ford, A. Hassani, G. Karathanasis, E. MacDonald, N. Manganelli, F. Marini, A. Perloff, C. Savard, N. Schonbeck, K. Stenson, K. A. Ulmer, S. R. Wagner, N. Zipper

Cornell University, Ithaca, NY, USA
J. Alexander, S. Bright-Thonney, X. Chen, D. J. Cranshaw, J. Fan, X. Fan, D. Gadkari, S. Hogan, J. Monroy, J. R. Patterson, J. Reichert, M. Reid, A. Ryd, J. Thom, P. Wittich, R. Zou

Fermi National Accelerator Laboratory, Batavia, IL, USA
M. Albrow, M. Alyari, O. Amram, G. Apollinari, A. Apresyan, L. A. T. Bauerdick, D. Berry, J. Berryhill, P. C. Bhat, K. Burkett, J. N. Butler, A. Canepa, G. B. Cerati, H. W. K. Cheung, F. Chlebana, G. Cummings, J. Dickinson, I. Dutta, V. D. Elvira, Y. Feng, J. Freeman, A. Gandrakota, Z. Gecse, L. Gray, D. Green, S. Grünendahl, D. Guerrero, O. Gutsche, R. M. Harris, R. Heller, T. C. Herwig, J. Hirschauer, L. Horyn, B. Jayatilaka, S. Jindariani, M. Johnson, U. Joshi, T. Klijnsma, B. Klima, K. H. M. Kwok, S. Lammel, D. Lincoln, R. Lipton, T. Liu, C. Madrid, K. Maeshima, C. Mantilla, D. Mason, P. McBride, P. Merkel, S. Mrenna, S. Nahn, J. Ngadiuba, D. Noonan, V. Papadimitriou, N. Pastika, K. Pedro, C. Pena[84], F. Ravera, A. Reinsvold Hall[85], L. Ristori, E. Sexton-Kennedy, N. Smith, A. Soha, L. Spiegel, J. Strait, L. Taylor, S. Tkaczyk, N. V. Tran, L. Uplegger, E. W. Vaandering, I. Zoi

University of Florida, Gainesville, FL, USA

P. Avery, D. Bourilkov, L. Cadamuro, P. Chang, V. Cherepanov, R. D. Field, E. Koenig, M. Kolosova, J. Konigsberg, A. Korytov, K. H. Lo, K. Matchev, N. Menendez, G. Mitselmakher, A. Muthirakalayil Madhu, N. Rawal, D. Rosenzweig, S. Rosenzweig, K. Shi, J. Wang

Florida State University, Tallahassee, FL, USA
T. Adams, A. Al Kadhim, A. Askew, N. Bower, R. Habibullah, V. Hagopian, R. Hashmi, R. S. Kim, S. Kim, T. Kolberg, G. Martinez, H. Prosper, P. R. Prova, O. Viazlo, M. Wulansatiti, R. Yohay, J. Zhang

Florida Institute of Technology, Melbourne, FL, USA
B. Alsufyani, M. M. Baarmand, S. Butalla, T. Elkafrawy[15], M. Hohlmann, R. Kumar Verma, M. Rahmani, F. Yumiceva

University of Illinois Chicago, Chicago, USA
M. R. Adams, C. Bennett, R. Cavanaugh, S. Dittmer, O. Evdokimov, C. E. Gerber, D. J. Hofman, J. H. Lee, D. S. Lemos, A. H. Merrit, C. Mills, S. Nanda, G. Oh, D. Pilipovic, T. Roy, S. Rudrabhatla, M. B. Tonjes, N. Varelas, X. Wang, Z. Ye, J. Yoo

The University of Iowa, Iowa City, IA, USA
M. Alhusseini, D. Blend, K. Dilsiz[86], L. Emediato, G. Karaman, O. K. Köseyan, J.-P. Merlo, A. Mestvirishvili[87], J. Nachtman, O. Neogi, H. Ogul[88], Y. Onel, A. Penzo, C. Snyder, E. Tiras[89]

Johns Hopkins University, Baltimore, MD, USA
B. Blumenfeld, L. Corcodilos, J. Davis, A. V. Gritsan, L. Kang, S. Kyriacou, P. Maksimovic, M. Roguljic, J. Roskes, S. Sekhar, M. Swartz, T. Á. Vámi

The University of Kansas, Lawrence, KS, USA
A. Abreu, L. F. Alcerro Alcerro, J. Anguiano, P. Baringer, A. Bean, Z. Flowers, J. King, G. Krintiras, M. Lazarovits, C. Le Mahieu, C. Lindsey, J. Marquez, N. Minafra, M. Murray, M. Nickel, M. Pitt, S. Popescu[90], C. Rogan, C. Royon, R. Salvatico, S. Sanders, C. Smith, Q. Wang, G. Wilson

Kansas State University, Manhattan, KS, USA
B. Allmond, S. Duric, A. Ivanov, K. Kaadze, A. Kalogeropoulos, D. Kim, Y. Maravin, T. Mitchell, K. Nam, J. Natoli, D. Roy

Lawrence Livermore National Laboratory, Livermore, CA, USA
F. Rebassoo, D. Wright

University of Maryland, College Park, MD, USA
E. Adams, A. Baden, O. Baron, A. Belloni, A. Bethani, Y. M. Chen, S. C. Eno, N. J. Hadley, S. Jabeen, R. G. Kellogg, T. Koeth, Y. Lai, S. Lascio, A. C. Mignerey, S. Nabili, C. Palmer, C. Papageorgakis, L. Wang, K. Wong

Massachusetts Institute of Technology, Cambridge, MA, USA
J. Bendavid, W. Busza, I. A. Cali, Y. Chen, M. D'Alfonso, J. Eysermans, C. Freer, G. Gomez-Ceballos, M. Goncharov, P. Harris, D. Hoang, D. Kovalskyi, J. Krupa, L. Lavezzo, Y.-J. Lee, K. Long, C. Mironov, C. Paus, D. Rankin, C. Roland, G. Roland, S. Rothman, Z. Shi, G. S. F. Stephans, J. Wang, Z. Wang, B. Wyslouch, T. J. Yang

University of Minnesota, Minneapolis, MN, USA
R. M. Chatterjee, B. Crossman, B. M. Joshi, C. Kapsiak, M. Krohn, D. Mahon, J. Mans, M. Revering, R. Rusack, R. Saradhy, N. Schroeder, N. Strobbe, M. A. Wadud

University of Mississippi, Oxford, MS, USA
L. M. Cremaldi

University of Nebraska-Lincoln, Lincoln, NE, USA

K. Bloom, M. Bryson, D. R. Claes, C. Fangmeier, F. Golf, C. Joo, I. Kravchenko, I. Reed, J. E. Siado, G. R. Snow[†], W. Tabb, A. Wightman, F. Yan, A. G. Zecchinelli

State University of New York at Buffalo, Buffalo, NY, USA
G. Agarwal, H. Bandyopadhyay, L. Hay, I. Iashvili, A. Kharchilava, C. McLean, M. Morris, D. Nguyen, J. Pekkanen, S. Rappoccio, H. Rejeb Sfar, A. Williams

Northeastern University, Boston, MA, USA
G. Alverson, E. Barberis, Y. Haddad, Y. Han, A. Krishna, J. Li, G. Madigan, B. Marzocchi, D. M. Morse, V. Nguyen, T. Orimoto, A. Parker, L. Skinnari, A. Tishelman-Charny, B. Wang, D. Wood

Northwestern University, Evanston, IL, USA
S. Bhattacharya, J. Bueghly, Z. Chen, A. Gilbert, K. A. Hahn, Y. Liu, D. G. Monk, M. H. Schmitt, A. Taliercio, M. Velasco

University of Notre Dame, Notre Dame, IN, USA
R. Band, R. Bucci, M. Cremonesi, A. Das, R. Goldouzian, M. Hildreth, K. Hurtado Anampa, C. Jessop, K. Lannon, J. Lawrence, N. Loukas, L. Lutton, J. Mariano, N. Marinelli, I. Mcalister, T. McCauley, C. Mcgrady, K. Mohrman, C. Moore, Y. Musienko[11], H. Nelson, R. Ruchti, A. Townsend, M. Wayne, H. Yockey, M. Zarucki, L. Zygala

The Ohio State University, Columbus, OH, USA
B. Bylsma, M. Carrigan, L. S. Durkin, C. Hill, M. Joyce, A. Lesauvage, M. Nunez Ornelas, K. Wei, B. L. Winer, B. R. Yates

Princeton University, Princeton, NJ, USA
F. M. Addesa, H. Bouchamaoui, P. Das, G. Dezoort, P. Elmer, A. Frankenthal, B. Greenberg, N. Haubrich, S. Higginbotham, G. Kopp, S. Kwan, D. Lange, A. Loeliger, D. Marlow, I. Ojalvo, J. Olsen, D. Stickland, C. Tully

University of Puerto Rico, Mayaguez, PR, USA
S. Malik

Purdue University, West Lafayette, IN, USA
A. S. Bakshi, V. E. Barnes, S. Chandra, R. Chawla, S. Das, A. Gu, L. Gutay, M. Jones, A. W. Jung, D. Kondratyev, A. M. Koshy, M. Liu, G. Negro, N. Neumeister, G. Paspalaki, S. Piperov, A. Purohit, J. F. Schulte, M. Stojanovic[16], J. Thieman, F. Wang, W. Xie

Purdue University Northwest, Hammond, IN, USA
J. Dolen, N. Parashar, A. Pathak

Rice University, Houston, TX, USA
D. Acosta, A. Baty, T. Carnahan, S. Dildick, K. M. Ecklund, P. J. Fernández Manteca, S. Freed, P. Gardner, F. J. M. Geurts, A. Kumar, W. Li, O. Miguel Colin, B. P. Padley, R. Redjimi, J. Rotter, S. Yang, E. Yigitbasi, Y. Zhang

University of Rochester, Rochester, NY, USA
A. Bodek, P. de Barbaro, R. Demina, J. L. Dulemba, C. Fallon, A. Garcia-Bellido, O. Hindrichs, A. Khukhunaishvili, P. Parygin, E. Popova, R. Taus, G. P. Van Onsem

The Rockefeller University, New York, NY, USA
K. Goulianos

Rutgers, The State University of New Jersey, Piscataway, NJ, USA
B. Chiarito, J. P. Chou, Y. Gershtein, E. Halkiadakis, A. Hart, M. Heindl, D. Jaroslawski, O. Karacheban[25], I. Laflotte, A. Lath, R. Montalvo, K. Nash, M. Osherson, H. Routray, S. Salur, S. Schnetzer, S. Somalwar, R. Stone, S. A. Thayil, S. Thomas, J. Vora, H. Wang

University of Tennessee, Knoxville, TN, USA
H. Acharya, A. G. Delannoy, S. Fiorendi, T. Holmes, N. Karunarathna, L. Lee, E. Nibigira, S. Spanier

Texas A&M University, College Station, TX, USA
M. Ahmad, O. Bouhali[91], M. Dalchenko, A. Delgado, R. Eusebi, J. Gilmore, T. Huang, T. Kamon[92], H. Kim, S. Luo, S. Malhotra, R. Mueller, D. Overton, D. Rathjens, A. Safonov

Texas Tech University, Lubbock, TX, USA
N. Akchurin, J. Damgov, V. Hegde, A. Hussain, Y. Kazhykarim, K. Lamichhane, S. W. Lee, A. Mankel, T. Mengke, S. Muthumuni, T. Peltola, I. Volobouev, A. Whitbeck

Vanderbilt University, Nashville, TN, USA
E. Appelt, S. Greene, A. Gurrola, W. Johns, R. Kunnawalkam Elayavalli, A. Melo, F. Romeo, P. Sheldon, S. Tuo, J. Velkovska, J. Viinikainen

University of Virginia, Charlottesville, VA, USA
B. Cardwell, B. Cox, J. Hakala, R. Hirosky, A. Ledovskoy, A. Li, C. Neu, C. E. Perez Lara

Wayne State University, Detroit, MI, USA
P. E. Karchin

University of Wisconsin-Madison, Madison, WI, USA
A. Aravind, S. Banerjee, K. Black, T. Bose, S. Dasu, I. De Bruyn, P. Everaerts, C. Galloni, H. He, M. Herndon, A. Herve, C. K. Koraka, A. Lanaro, R. Loveless, J. Madhusudanan Sreekala, A. Mallampalli, A. Mohammadi, S. Mondal, G. Parida, D. Pinna, A. Savin, V. Shang, V. Sharma, W. H. Smith, D. Teague, H. F. Tsoi, W. Vetens, A. Warden

Authors affiliated with an institute or an international laboratory covered by a cooperation agreement with CERN, Geneva, Switzerland
S. Afanasiev, V. Andreev, Yu. Andreev, T. Aushev, M. Azarkin, A. Babaev, A. Belyaev, V. Blinov[93], E. Boos, V. Borshch, D. Budkouski, M. Chadeeva[93], V. Chekhovsky, A. Dermenev, T. Dimova[93], D. Druzhkin[94], M. Dubinin[84], L. Dudko, G. Gavrilov, V. Gavrilov, S. Gninenko, V. Golovtcov, N. Golubev, I. Golutvin, I. Gorbunov, A. Gribushin, Y. Ivanov, V. Kachanov, L. Kardapoltsev[93], V. Karjavine, A. Karneyeu, V. Kim[93], M. Kirakosyan, D. Kirpichnikov, M. Kirsanov, V. Klyukhin, O. Kodolova[95], D. Konstantinov, V. Korenkov, A. Kozyrev[93], N. Krasnikov, A. Lanev, P. Levchenko[96], O. Lukina, N. Lychkovskaya, V. Makarenko, A. Malakhov, V. Matveev[93,97], V. Murzin, A. Nikitenko[95,98], S. Obraztsov, V. Oreshkin, A. Oskin, V. Palichik, V. Perelygin, S. Petrushanko, S. Polikarpov[93], V. Popov, O. Radchenko[93], V. Rusinov, M. Savina, V. Savrin, D. Selivanova, V. Shalaev, S. Shmatov, S. Shulha, Y. Skovpen[93], S. Slabospitskii, V. Smirnov, A. Snigirev, D. Sosnov, V. Sulimov, E. Tcherniaev, A. Terkulov, O. Teryaev, I. Tlisova, A. Toropin, L. Uvarov, A. Uzunian, A. Vorobyev[†], N. Voytishin, B. S. Yuldashev[99], A. Zarubin, I. Zhizhin, A. Zhokin

[†] **Deceased**

1: Also at Yerevan State University, Yerevan, Armenia
2: Also at TU Wien, Vienna, Austria
3: Also at Institute of Basic and Applied Sciences, Faculty of Engineering, Arab Academy for Science, Technology and Maritime Transport, Alexandria, Egypt
4: Also at Université Libre de Bruxelles, Bruxelles, Belgium
5: Also at Universidade Estadual de Campinas, Campinas, Brazil
6: Also at Federal University of Rio Grande do Sul, Porto Alegre, Brazil
7: Also at UFMS, Nova Andradina, Brazil
8: Also at University of Chinese Academy of Sciences, Beijing, China
9: Also at Nanjing Normal University, Nanjing, China
10: Now at The University of Iowa, Iowa City, IA, USA
11: Also at an institute or an international laboratory covered by a cooperation agreement with CERN, Geneva, Switzerland
12: Also at Helwan University, Cairo, Egypt
13: Now at Zewail City of Science and Technology, Zewail, Egypt
14: Also at British University in Egypt, Cairo, Egypt
15: Now at Ain Shams University, Cairo, Egypt

16: Also at Purdue University, West Lafayette, Indiana, USA
17: Also at Université de Haute Alsace, Mulhouse, France
18: Also at Department of Physics, Tsinghua University, Beijing, China
19: Also at The University of the State of Amazonas, Manaus, Brazil
20: Also at Erzincan Binali Yildirim University, Erzincan, Turkey
21: Also at University of Hamburg, Hamburg, Germany
22: Also at III. Physikalisches Institut A, RWTH Aachen University, Aachen, Germany
23: Also at Isfahan University of Technology, Isfahan, Iran
24: Also at Bergische University Wuppertal (BUW), Wuppertal, Germany
25: Also at Brandenburg University of Technology, Cottbus, Germany
26: Also at Forschungszentrum Jülich, Juelich, Germany
27: Also at CERN, European Organization for Nuclear Research, Geneva, Switzerland
28: Also at Institute of Physics, University of Debrecen, Debrecen, Hungary
29: Also at Institute of Nuclear Research ATOMKI, Debrecen, Hungary
30: Now at Universitatea Babes-Bolyai-Facultatea de Fizica, Cluj-Napoca, Romania
31: Also at Physics Department, Faculty of Science, Assiut University, Assiut, Egypt
32: Also at HUN-REN Wigner Research Centre for Physics, Budapest, Hungary
33: Also at Faculty of Informatics, University of Debrecen, Debrecen, Hungary
34: Also at Punjab Agricultural University, Ludhiana, India
35: Also at UPES-University of Petroleum and Energy Studies, Dehradun, India
36: Also at University of Visva-Bharati, Santiniketan, India
37: Also at University of Hyderabad, Hyderabad, India
38: Also at Indian Institute of Science (IISc), Bangalore, India
39: Also at IIT Bhubaneswar, Bhubaneswar, India
40: Also at Institute of Physics, Bhubaneswar, India
41: Also at Deutsches Elektronen-Synchrotron, Hamburg, Germany
42: Now at Department of Physics, Isfahan University of Technology, Isfahan, Iran
43: Also at Sharif University of Technology, Tehran, Iran
44: Also at Department of Physics, University of Science and Technology of Mazandaran, Behshahr, Iran
45: Also at Italian National Agency for New Technologies, Energy and Sustainable Economic Development, Bologna, Italy
46: Also at Centro Siciliano di Fisica Nucleare e di Struttura Della Materia, Catania, Italy
47: Also at Università degli Studi Guglielmo Marconi, Rome, Italy
48: Also at Scuola Superiore Meridionale, Università di Napoli 'Federico II', Naples, Italy
49: Also at Fermi National Accelerator Laboratory, Batavia, IL, USA
50: Also at Laboratori Nazionali di Legnaro dell'INFN, Legnaro, Italy
51: Also at Università di Napoli 'Federico II', Naples, Italy
52: Also at Consiglio Nazionale delle Ricerche - Istituto Officina dei Materiali, Perugia, Italy
53: Also at IRFU, CEA, Université Paris-Saclay, Gif-sur-Yvette, France
54: Also at Riga Technical University, Riga, Latvia
55: Also at Department of Applied Physics, Faculty of Science and Technology, Universiti Kebangsaan Malaysia, Bangi, Malaysia
56: Also at Consejo Nacional de Ciencia y Tecnología, Mexico City, Mexico
57: Also at Trincomalee Campus, Eastern University, Nilaveli, Sri Lanka
58: Also at INFN Sezione di Pavia, Università di Pavia, Pavia, Italy
59: Also at National and Kapodistrian University of Athens, Athens, Greece
60: Also at Ecole Polytechnique Fédérale Lausanne, Lausanne, Switzerland
61: Also at Universität Zürich, Zurich, Switzerland
62: Also at Stefan Meyer Institute for Subatomic Physics, Vienna, Austria
63: Also at Laboratoire d'Annecy-le-Vieux de Physique des Particules, IN2P3-CNRS, Annecy-le-Vieux, France
64: Also at Near East University, Research Center of Experimental Health Science, Mersin, Turkey
65: Also at Konya Technical University, Konya, Turkey
66: Also at Izmir Bakircay University, Izmir, Turkey
67: Also at Adiyaman University, Adiyaman, Turkey

68: Also at Necmettin Erbakan University, Konya, Turkey
69: Also at Bozok Universitetesi Rektörlügü, Yozgat, Turkey
70: Also at Marmara University, Istanbul, Turkey
71: Also at Milli Savunma University, Istanbul, Turkey
72: Also at Kafkas University, Kars, Turkey
73: Also at Hacettepe University, Ankara, Turkey
74: Also at Faculty of Engineering, Istanbul University-Cerrahpasa, Istanbul, Turkey
75: Also at Ozyegin University, Istanbul, Turkey
76: Also at Vrije Universiteit Brussel, Brussel, Belgium
77: Also at School of Physics and Astronomy, University of Southampton, Southampton, UK
78: Also at University of Bristol, Bristol, UK
79: Also at IPPP Durham University, Durham, UK
80: Also at Monash University, Faculty of Science, Clayton, Australia
81: Also at Università di Torino, Turin, Italy
82: Also at Bethel University, St. Paul, MN, USA
83: Also at Karamanoğlu Mehmetbey University, Karaman, Turkey
84: Also at California Institute of Technology, Pasadena, CA, USA
85: Also at United States Naval Academy, Annapolis, MD, USA
86: Also at Bingol University, Bingol, Turkey
87: Also at Georgian Technical University, Tbilisi, Georgia
88: Also at Sinop University, Sinop, Turkey
89: Also at Erciyes University, Kayseri, Turkey
90: Also at Horia Hulubei National Institute of Physics and Nuclear Engineering (IFIN-HH), Bucharest, Romania
91: Also at Texas A&M University at Qatar, Doha, Qatar
92: Also at Kyungpook National University, Daegu, Korea
93: Also at another institute or international laboratory covered by a cooperation agreement with CERN, Geneva, Switzerland
94: Also at Universiteit Antwerpen, Antwerpen, Belgium
95: Also at Yerevan Physics Institute, Yerevan, Armenia
96: Also at Northeastern University, Boston, MA, USA
97: Now at another institute or international laboratory covered by a cooperation agreement with CERN, Geneva, Switzerland
98: Also at Imperial College, London, UK
99: Also at Institute of Nuclear Physics of the Uzbekistan Academy of Sciences, Tashkent, Uzbekistan